

A diamond spin qubit scanning probe microscope

Présentée le 11 septembre 2023

Faculté des sciences de base
Laboratoire de science à l'échelle nanométrique
Programme doctoral en physique

pour l'obtention du grade de Docteur ès Sciences

par

Dinesh Kevin Mathais PINTO

Acceptée sur proposition du jury

Prof. A. Pasquarello, président du jury
Prof. K. Kern, directeur de thèse
Prof. F. Jelezko, rapporteur
Dr S. Stepanow, rapporteur
Dr S. Rusponi, rapporteur

If we can't trust people with freedom, how can we trust them with power?

— Anonymous

Acknowledgements

I am immensely grateful to Prof. Klaus Kern for giving me the opportunity to work on this research project. I particularly appreciate the trust he showed in me by allowing me the freedom to pursue my own research ideas over the course of this thesis.

I would also like to thank my jury president, Prof. Alfredo Pasquarello, and the members of my jury committee – Dr. Stefano Rusponi, Prof. Fedor Jelezko, and Dr. Sebastian Stepanow for their interest in this project.

I am extremely grateful to my group leader Dr. Aparajita Singha, for her patient guidance, constant encouragement and helpful advice she has provided me throughout this thesis. In addition, I would also like to thank Dr. Ricardo Román and Dr. Toni Hache for their support in the lab and engagement in scientific discussions.

Without technical support, a thesis like this is not possible. An enormous thanks goes to Wolfgang Stiepany and Marko Memmler, for their work in the design and construction of the new experimental setup. A special thanks goes to Dr. Isabel Pfender for her work in building complex electronics required in the setup.

An important thanks goes to Sabine Birtel and Anh Eymann, who skillfully dealt with the administrative demands of this project. I would also like to thank the EPDY division at EPFL, and the Nanoscale Science division at MPI-FKF for the productive discussions and enlightening insights.

The time spent with the anons of Reddit and CT, debating the future of technology, money, and markets were equal parts exhausting and stimulating. Every week was a big week with them involved.

Finally, I must express my very profound gratitude to my parents for providing me with unfailing support, and encouragement throughout my years of study and through the process of researching and writing this thesis.

Lausanne, June 28, 2023

D.P.

Abstract

The properties of a physical system only exist in relation to its environment. This thesis presents the development of a novel spin qubit scanning probe microscope operating over a wide range of environmental conditions. The qubit, which sits at the heart of the microscope, is realized by a nitrogen vacancy (NV) defect in diamond, which in its negatively charged configuration is extremely sensitive to local magnetic fields. We further leverage this local sensitivity by integrating the NV center into a scanning probe microscope (SPM) tip, allowing us to record spatially resolved images of near-surface magnetic structures.

Before we can run, we must first walk. To test the capabilities of the NV, we demonstrate electron paramagnetic resonance on an encapsulated nitrogen spin ($N@C_{60}$) using a single near-surface NV center in diamond at 4.7 K. Exploiting the strong magnetic dipolar interaction between the NV and endofullerene electronic spins, we demonstrate RF pulse controlled Rabi oscillations and measure spin-echos on an encapsulated spin. This measurement, while novel, also exposed us to the limitations of using a “fixed” NV center.

These limitations motivated us to design and construct an entirely new NV scanning probe microscope (NV-SPM). This NV-SPM is capable of operating from ambient pressure to ultra-high vacuum (10^{-9} mbar), from room to cryogenic temperatures (4.7 K), and from zero-field to high vector magnetic fields (1 T). In addition, the system is capable of generating nanosecond pulsed RF excitation up to 20 GHz, can perform confocal imaging and second-order photon correlation, can record real-time optical spectra, and features both active and passive damping to minimize vibrations. The system functionality is tied together with a custom built software package, which allows for advanced levels of measurement sequencing, control and analysis.

To test the nanoscale imaging capabilities of the NV-SPM, we probed domain wall structures in synthetic antiferromagnetic (SAF) thin films. Unlike ferromagnetic materials, SAF films only exhibit a weak net magnetic moment, which generally demands techniques such as X-ray photoemission electron microscopy or spin-polarized scanning tunneling microscopy. These techniques either require complex synchrotron facilities, or are limited to electronically conducting samples. An NV-SPM, on the other hand, places no such restrictions. We perform nanoscale, all-optical relaxometry measurements on SAF films at ambient conditions, and observe clear domain wall structures in good agreement with our magnetic force microscopy measurements on the same sample.

Abstract

As this thesis demonstrates, near-surface NV centers are incredible quantum sensors. Despite this, they are also subject to a number of other effects, such as charge state transitions, which often lead to a loss of coherence. We perform the first measurements examining the charge state behavior of the NV center in diamond tips as a function of vacuum. Using spectroscopic and second-order correlation measurements, we report a clear vacuum induced charge state transition from NV^- to NV^0 . We also observe anomalous effects related to the confocal “size” of the NV center when it undergoes this transition. Finally, we demonstrate that the vacuum induced transition to NV^0 is completely reversible in nature.

Keywords: quantum sensing, quantum information, spin qubit, nitrogen vacancy (NV), scanning probe microscopy (SPM), confocal microscopy, high-frequency pulsed RF, ultra-high vacuum (UHV), cryogenic temperature, field-programmable gate array (FPGA)

Zusammenfassung

Die Eigenschaften eines physikalischen Systems existieren nur in Verbindung zu seiner Umgebung. Diese Thesis zeigt die Entwicklung eines neuartigen Qubit-basierten Rastersondenmikroskops, das über einen weiten Messbereichs. Die Wahl des Qubits, welche entscheidend für den Erfolg der Aufgabe ist und den Kern des Systems darstellt, ist ein einzelnes Spin-Qubit eingeschlossen im Diamantgitter. Das Spin-Qubit ist durch ein Stickstoff-Fehlstellenzentrum (englisch nitrogen vacancy, NV) im Gitter dargestellt, welches in der negativ geladenen Konfiguration einen einzigartigen Energielevelgrundzustand aufweist, was es extrem empfindlich auf lokale Magnetfelder macht. Die Integration eines NVs in die Spitze eines Rastersondenmikroskop (englisch scanning probe microscope, SPM) erlaubt uns räumlich hochaufgelöste Bilder von oberflächennahen magnetischen Strukturen aufzunehmen.

Bevor wir rennen können, müssen wir zuerst laufen. Um die Möglichkeiten des NVs zu testen, zeigten wir die Messung der Elektronenspinresonanz an einem Stickstoffspin, der in eine C_{60} -Molekül eingeschlossen ist. Dabei wurde ein einzelnes oberflächennahes NV in Diamant bei 4.7 K verwendet. Unter Ausnutzung der starken magnetischen dipolaren Wechselwirkung zwischen NV und Stickstoffspin zeigten wir Rabi-Oszillationen, die durch Radiofrequenzpulse gesteuert werden und maßen das Spinecho am eingeschlossenen Spin. Diese Messung - obwohl neuartig - zeigt die Grenzen von unbeweglichen NVs auf.

Das motivierte uns, während der Bearbeitung dieser Thesis, ein komplett neues NV-basiertes Rastersondenmikroskop (NV-SPM) zu konstruieren und aufzubauen. Dieses NV-SPM besitzt die Möglichkeit zwischen Umgebungsdruck und Ultrahochvakuum (10^{-9} mbar), zwischen Raumtemperatur und kryogenen Temperaturen (4.7 K) und bis zu einem magnetischen Feld von 1 T zu messen. Zusätzlich kann das Messsystem Radiofrequenzpulse im Nanosekundenbereich bis zu einer Frequency von 20 GHz erzeugen, kann hochaufgelöste konfokale Mikroskop Bilder und Photonenkorrelationen zweiter Ordnung aufnehmen und besitzt aktive und passive mechanische Dämpfer, um Vibrationen zu minimieren. Alle Funktionen des Systems wird durch ein Software gesteuert, die während der Thesis entwickelt wurde, was hochmoderne Messsequenzen und deren Auswertung erlaubt.

Um die Möglichkeiten des NV-SPM zu testen, untersuchten wir die Domänenwände in einer synthetisch-antiferromagnetischen (SAF) Dünnschicht. Im Gegensatz zu ferromagnetischen Materialien zeigen SAFs nur ein magnetischen Moment auf der atomaren Skala. Diese schwa-

Zusammenfassung

Die magnetische Natur stellt besondere Anforderungen an räumliche Auflösung und magnetischer Empfindlichkeit des Sensors, was normalerweise Messungen wie Röntgenphotoemissionsmikroskopie und spinpolarisierte Rastertunnelmikroskopie erfordert. Diese Techniken erfordern entweder komplexe Synchrotroninfrastruktur oder sind auf elektrisch leitfähige Proben beschränkt. Wir benutzen ein einzelnes NV, um nanoskalierte, komplett optische Relaxometrie-Messungen an SAFs bei Umgebungsbedingungen durchzuführen. Wir beobachten definierte Domänenwandstrukturen, in guter Übereinstimmung mit unseren eigenen Magnetkraftmikroskopmessungen übereinstimmen.

Wie wir in dieser Thesis demonstrieren, sind oberflächennahe, negative geladene NVs herausragende Quantensensoren. Trotzdem werden sie von einer Reihe anderer Faktoren beeinflusst, wie zum Beispiel dem Verlust der negativen Ladung, was oft zu einem Verlust von Kohärenz führt. Unter Vakuumbedingung kommt dieser schädliche Ladungstransfer sogar noch stärker zum tragen. Wir zeigen die erste Durchführung von Ladungstransfermessungen von NV-Messspitzen in unterschiedlichen Vakuumdruckbereichen. Durch Nutzung von Spektroskopie und Korrelationsmessungen zweiter Ordnung, stellen wir einen deutlichen Ladungstransfer von NV^- zu NV^0 fest. Wir beobachten ebenfalls anomale Effekte, die sich auf die konfokale „Größe“ des NVs beziehen, wenn der Ladungstransfer stattfindet. Zum Schluss zeigen wir, dass der vakuuminduzierte Ladungstransfer komplett reversibel verläuft.

Stichwörter: quantensensorik, quanteninformation, spin-qubit, nitrogen-vacancy, raster-sondenmikroskopie, konfokalmikroskop, hochfrequente pulselektronik, ultrahochvakuum, tiefemperatur, field-programmable gate array

Contents

Acknowledgements	i
Abstract (English/Deutsch)	iii
List of figures	xi
List of acronyms	xiii
Introduction	1
1 The nitrogen vacancy center	5
1.1 Structure and fabrication	5
1.2 Initialization, control and readout	7
1.3 Optically detected magnetic resonance (ODMR)	12
1.4 ODMR pulse sequences	13
1.5 NV scanning probe microscopy (NV-SPM)	15
2 Readout & control of an endofullerene electronic spin	17
2.1 Structure and synthesis	18
2.2 Ground state spin Hamiltonian	18
2.3 Preparing the sensor and system	20
2.4 Double electron-electron resonance (DEER) spectroscopy	20
2.5 N@C ₆₀ spin control and relaxation	24
2.6 Coherence of N@C ₆₀ spins	26
2.7 Conclusion	27
3 Construction of a low-temperature & ultra-high vacuum NV-SPM	29
3.1 Setup goals and constraints	29
3.2 Measurement head	30
3.3 Low temperature	37
3.4 Ultra-high vacuum	41
3.5 Confocal laser scanning microscope	42
3.6 Pulsed microwave	45
3.7 Dry vector magnet	47

Contents

3.8	Measurement control with Qudi-Hira	49
3.9	Ambient stage	52
3.10	Active and Passive damping stages	52
3.11	Final system	53
4	Performance of the NV-SPM	57
4.1	Ultra high vacuum and low temperature	57
4.2	Dry vector magnet	59
4.3	Confocal microscopy	61
4.4	Pulsed microwave control	64
4.5	Optically detected magnetic resonance measurements	65
4.6	Atomic force microscopy	67
5	Imaging domain walls in synthetic antiferromagnetic thin films	71
5.1	Multilayer films of Co, Pt and Ru	72
5.2	Measurement principles	72
5.3	NV-SPM on an (X=7, N=17) multilayer	73
5.4	NV-SPM on an (X=6, N=4) multilayer	76
5.5	Permanent quenching of conventional NV tips	78
6	Vacuum induced charge state transition of NV diamond tips	83
6.1	NV center charge states	83
6.2	Preparation	85
6.3	Vacuum induced NV ⁻ to NV ⁰ transition	86
6.4	Spectroscopic variation with pressure	87
6.5	Autocorrelation variation with pressure	89
6.6	Confocal variation with pressure	91
6.7	Recovery of NV ⁻ post vacuum exposure	93
7	Conclusion & Outlook	95
A	Data Processing with Qudi-Hira-Analysis	99
A.1	Spin state computation	103
A.2	Spectroscopy analysis	103
A.3	Oscillation analysis	104
A.4	Hahn-Echo analysis	104
A.5	Second order correlation analysis	105
A.6	Error estimation	105
B	Perturbation theory & coupling strength	107
B.1	Dependence on zero-field axis	108
B.2	Dependence on anisotropic hyperfine interaction	108
B.3	Enhanced hyperfine & zero-field interactions	109
B.4	Non-thermal spin distributions	109

B.5 Coupling strength & distance	110
C Setup Components	113
C.1 Nano-positioning stage	113
C.2 Tip/sample stage	113
C.3 Atomic force microscope	114
C.4 Ultra high vacuum	114
C.5 Low temperature	114
C.6 Vector magnet	114
C.7 Confocal microscope	115
C.8 Pulsed microwave	116
C.9 Communication protocols	116
Bibliography	123
Curriculum Vitae	125

List of Figures

1	Attocube magnetic imaging conference poll	2
2	Artistic render of an NV-SPM	3
1.1	NV center structure in diamond	5
1.2	Single NV centers in diamond membranes and tips	7
1.3	NV center symmetries and energy levels	8
1.4	NV spin state initialization and readout	11
1.5	Pulsed ODMR	12
1.6	T_1 pulse sequence	14
1.7	Ramsey T_2^* pulse sequence	14
1.8	Hahn-Echo T_2 pulse sequence	14
1.9	DEER pulse sequence	15
1.10	Diamond tip AFM resonance curve	16
2.1	N@C ₆₀ energy levels and EPR spectrum	19
2.2	N@C ₆₀ coated diamond nanopillars	21
2.3	DEER spectroscopy on N@C ₆₀	23
2.4	NV decoherence with N@C ₆₀	25
2.5	Spin-state control of N@C ₆₀	26
2.6	Phase coherence of N@C ₆₀	27
3.1	Piezoelectric stack on the measurement head	31
3.2	Tip/sample stage	33
3.3	Pin mapping of tip/sample holder	34
3.4	Preamplifier circuit diagram and model	36
3.5	Cryostat layout and cross-section	38
3.6	Cryostat cable thermalization	40
3.7	Cryostat top plate connection	41
3.8	Ultra-high vacuum chamber	42
3.9	Confocal laser scanning microscope	43
3.10	Pulsed MW configuration	46
3.11	Microwave on tip design	47
3.12	Dry vector magnet design and thermalization	48

List of Figures

3.13	Pulse generation and synchronization with Qudi-Hira	50
3.14	LabView & Qudi-Hira interface	51
3.15	Ambient stage for rapid testing of diamond tips	53
3.16	High level experimental schematic	54
3.17	Final system	55
4.1	Cryostat cool down, hold time and warmup	58
4.2	Dry vector magnet quenching	60
4.3	Confocal microscopy with a VISIR objective	62
4.4	Confocal microscopy with an MPLFLN objective	63
4.5	CMOS camera for co-locating tip and sample	63
4.6	Microwave pulse optimization	65
4.7	Microwave transmission	66
4.8	Measurement modality	68
4.9	Capacitive compensation and noise spectra	69
4.10	Calibration grating sample	70
5.1	Structure of synthetic anti-ferromagnet (SAF)	73
5.2	NV spin dependent PL and optical saturation	74
5.3	NV-SPM and MFM on SAF with X=7, N=17	75
5.4	NV-SPM variation with height and laser power	76
5.5	MFM on SAF with X=6, N=4	77
5.6	NV-SPM on SAF with X=6, N=4	79
5.7	Conventional NV tip quenching on approach	80
6.1	NV center charge states	84
6.2	Conventional and parabolic tips SEM	85
6.3	NV instability at UHV conditions	86
6.4	Spectroscopic variation with pressure	88
6.5	Autocorrelation variation with pressure	90
6.6	Sharp $g^{(2)}(\tau)$ variation at vacuum with laser power	90
6.7	Confocal variation with pressure	92
6.8	Recovery of NV ⁻ post vacuum exposure	94
A.1	Setting up the DataHandler object.	100
A.2	Code example of DataHandler and MeasurementDataclass	101
A.3	Qudi-Hira-Analysis and MeasurementDataclass schematic	102

List of acronyms

NV	nitrogen vacancy
SHPM	scanning Hall probe microscopy
MOKE	magneto optical Kerr microscopy
MFM	magnetic force microscopy
NV-SPM	nitrogen vacancy scanning probe microscopy
sSQUID	scanning SQUID microscopy
AFM	atomic force microscopy
SEM	scanning electron microscopy
DEER	double electron-electron resonance
EBL	electron beam lithography
FPGA	field programmable gate array
LO	local oscillator
AWG	arbitrary waveform generator
VNA	vector network analyzer
MW	microwave
UHV	ultra-high vacuum
EPR	electron paramagnetic resonance
DEER	double electron-electron resonance
HPLC	high pressure liquid chromatography
ODMR	optically detected magnetic resonance
AF	anti-ferromagnetic
ISC	intersystem crossing
ZPL	zero-phonon line
zfi	zero-field interaction
CVD	chemical vapor deposition
NTP	normal temperature and pressure
PL	photo-luminescence
SNR	signal-to-noise ratio
PEEK	polyetheretherketone
AD	analog-to-digital
PLL	phase locked loop
SRIM	stopping and range of ions in matter

Introduction

Sensors are fundamental to human life. The human body itself contains a wide array of sensors, ranging from temperature sensors in the skin, to chemical sensors in the tongue. These sensors are essential for our survival, as they allow us to detect and respond to changes in our environment. In addition to the sensors in our bodies, we also rely on external sensors to monitor and control our environment. For example, we use temperature sensors to control the temperature of our homes, and smoke sensors to alert ourselves of any impending danger.

At the cutting edge of technology lies quantum sensing. Quantum sensing is a rapidly growing field that aims to use the principles of quantum mechanics to enhance the accuracy and sensitivity of measurement devices. Unlike classical sensing techniques that rely on macroscopic objects, quantum sensing utilizes the unique properties of quantum systems, such as superposition and entanglement, to achieve unprecedented levels of precision and sensitivity.

Over the past few decades, there has been a significant interest in developing quantum sensing technologies for a wide range of applications, from fundamental scientific research to industrial applications. The potential benefits of these technologies are enormous, and they have the potential to revolutionize many fields, including materials science, medical diagnostics, and environmental monitoring.

In a quantum sensor, the physical quantity to be measured is encoded into the state of a quantum system, such as an electron, an atom, or a molecule. The sensing process involves two steps: *preparation* and *measurement*.

In the *preparation* step, the quantum sensor is initialized in a known state, such as a superposition of two energy states or a spin state. The physical quantity to be measured modifies the quantum state of the sensor, resulting in a measurable change in some observable property of the system, such as the energy level or the spin orientation.

In the *measurement* step, the quantum sensor is interrogated to read out the physical quantity of interest. This is done by applying a readout pulse or a series of pulses that interact with the quantum sensor and extract information about its state. The readout pulse causes the quantum state of the sensor to evolve, and the resulting state is then measured, typically by detecting the fluorescence or the electrical current generated by the sensor.

The sensitivity and precision of quantum sensors depend on several factors, including the

Introduction

coherence time of the quantum system, the strength of the interaction between the sensor and the physical quantity being measured, and the efficiency of the readout process. The high sensitivity of quantum sensors makes them suitable for a wide range of applications, including (but not limited to) atomic clocks, magnetic field sensors, and gravitational wave detectors.

Amongst the range of quantum sensors out there, one in particular stands out – the nitrogen vacancy (NV) center in diamond¹. The NV center consists of a nitrogen vacancy defect in a diamond crystal, which possesses an unpaired electron, whose spin can be used as a quantum bit (qubit) to store and manipulate quantum information. The electronic structure created by this defect has some highly unique properties,

- *Long coherence times*, the NV center can preserve its spin coherence up to several seconds, and phase coherence up to several milliseconds.
- *Ambient to cryogenic operation*, unlike many other quantum sensors that can only operate at cryogenic conditions, NV centers can also operate at ambient temperature.
- *Nanoscale spatial resolution*, the NV center can be integrated into a scanning probe microscope, allowing for magnetic imaging at the nanoscale.

The last property is critical, and the technique of performing magnetic imaging by integrating the NV center into a scanning probe microscope is known as nitrogen vacancy scanning probe microscopy (NV-SPM). This technique is particularly important to the magnetic imaging community, as is evidenced by a poll conducted at the Attocube Magnetic Imaging Conference in February 2021².

The conference attendees were posed the question – “What magnetic imaging technique do you consider most useful for your research?”. The results of the poll are shown in Fig. 1, and an astounding 48% of attendees indicating that they found NV-SPM the most useful magnetic imaging technique for their research. Among the competing techniques were scanning Hall probe microscopy (SHPM), magneto optical Kerr microscopy (MOKE), scanning SQUID microscopy (sSQUID), and magnetic force microscopy (MFM).

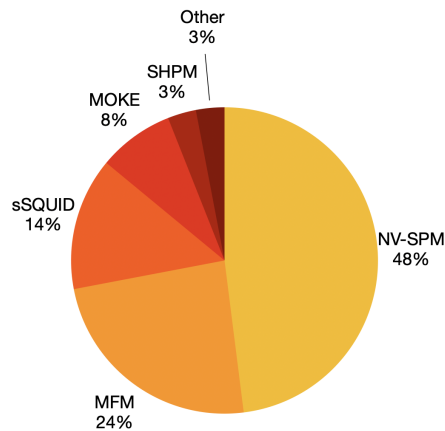


Fig. 1: Results of an online poll conducted at the Attocube Magnetic Imaging Conference².

This thesis aims to design and construct a novel NV-SPM operating over a wide range of environmental conditions. Physical scales such as pressure, temperature and applied magnetic field, are some of the most basic parameters that control the behavior of matter. The ability to fine-tune these parameters in a single experimental system is an incredibly powerful tool for probing the physics underlying exotic quantum materials.

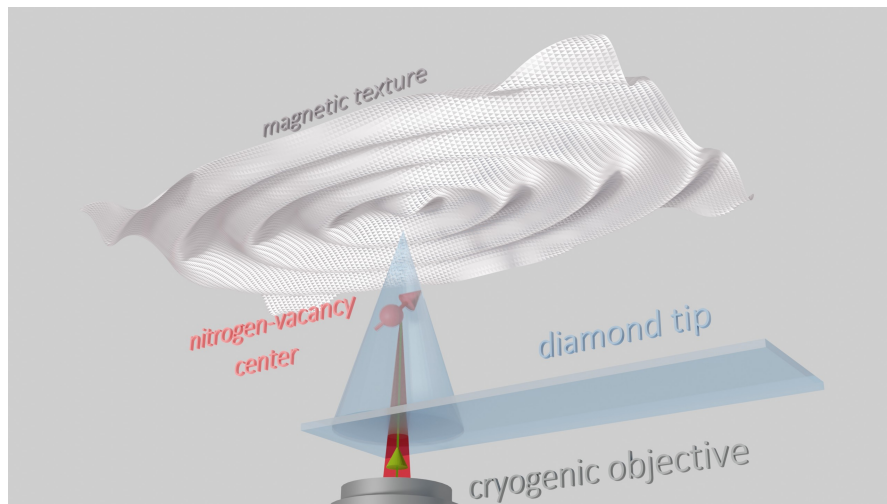


Fig. 2: Artistic render of an NV center inside a scanning probe tip imaging a magnetic texture.

Organization

The thesis is organized into a total of seven chapters and three appendices.

Chapter 1 provides a theoretical introduction to the NV center in diamond as a nanoscale magnetic field sensor.

Chapter 2 showcases the first experimental demonstration of readout and control of single endofullerenes, using an NV center in diamond at 4.7 K.

Chapter 3 describes the process, along with the challenges, of constructing a novel NV-SPM capable of operating at low temperature and UHV.

Chapter 4 details the testing carried out on the NV-SPM to ensure its proper operation, along with profiling its resolution and stability.

Chapter 5 demonstrates the measurement of domain walls in synthetic antiferromagnetic thin films using the NV-SPM.

Chapter 6 reports the first observation of a vacuum induced charge state transition of an NV center in a diamond tip.

Chapter 7 concludes this work with a brief summary, and lists several potential setup upgrades and avenues for future research.

Introduction

Appendix A describes the data processing methods used in this work, along with the open-source software toolkit (`Qudi-Hira-Analysis`) developed during the thesis.

Appendix B details a second-order perturbation theory simulation of a magnetically coupled pair of NV-N@C₆₀ spins.

Appendix C lists out the specific components used to construct different aspects of the experimental setup.

1 The nitrogen vacancy center

Perhaps time's definition of coal is the diamond.

Khalil Gibran

The NV center in diamond is formed by a substitutional nitrogen defect sitting adjacent to a vacancy defect in the diamond lattice. The center acts as an electron trap, which in its negatively charged configuration (NV^-) results in a multi-electron system with strongly coupled optical and microwave (MW) transitions. The optical transitions allow spin-state initialization and readout, and the MW transitions allow coherent electronic spin-state control. This unique combination has led to the realization of spin quantum registers³, nanoscale nuclear magnetic resonance (NMR)⁴, and sub-picotesla magnetic field sensitivity⁵. In this work, the NV center is used as a nanoscale type-II quantum sensor for magnetic field sensing^{6,7}.

1.1 Structure and fabrication

The NV center is a point defect in a two-atom basis diamond lattice (Fig. 1.1). Physically, this involves one atom at each lattice point with a second atom translated by $a/4$ along the

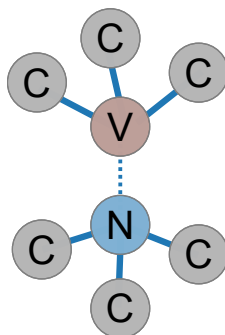


Fig. 1.1: Simplified structure of a single NV center in a diamond lattice. A ^{12}C atom (gray) is replaced by a ^{15}N atom (blue). A neighboring ^{12}C atom is removed, creating a vacancy site (red).

three orthogonal axes ($a = 0.36$ nm for diamond). Historically, NV centers were first fabricated inside bulk diamond samples¹, and then were integrated into scanning probe systems⁸. The earliest scanning probe systems used nanodiamonds as the NV center host, but with advances in material fabrication, modern NV scanning probes use nanopillar waveguide structures. Fig. 1.2 shows scanning electron microscopy (SEM) images of the different diamond structures that can host single NV centers along with the corresponding confocal scans.

The NV centers used in this work fall into two main categories — single NV centers in *diamond membranes*, and single NV centers in *diamond tips*. They both have different fabrication processes, characteristics, and use-cases. Their fabrication procedure is briefly described below.

Single NV centers in diamond membranes

The fabrication process begins with a $2\text{ mm} \times 2\text{ mm} \times 30\text{ }\mu\text{m}$ electronic grade [100] chemical vapor deposition (CVD) grown diamond sourced from Element Six™. The diamond is implanted with ^{15}N at an energy of 5 keV and subsequently annealed at $975\text{ }^\circ\text{C}$ for 2 h. Nanopillar waveguides with a 700 nm base diameter, 400 nm apex diameter and $1\text{ }\mu\text{m}$ height are etched into the diamond to increase optical collection efficiency⁹. Finally, the diamond surface is cleaned and oxygen terminated by boiling in a tri-acid mixture (1 : 1 : 1, HNO_3 : H_2SO_4 : HClO_4) at $200\text{ }^\circ\text{C}$ for ≈ 5 h.

Single NV centers in diamond tips

The fabrication process for diamond tips also uses an electronic grade [100] CVD grown diamond. The diamond is implanted with ^{15}N at an energy of 12 keV. This implantation energy leads to a nominal lower bound on NV depth of (17 ± 6) nm, calculated using the stopping and range of ions in matter (SRIM) software package. The ^{15}N radiation dose is chosen such that on average each nanopillar hosts a single NV center. Nanopillar waveguides with an apex diameter of 100 nm and height of $1\text{ }\mu\text{m}$ are etched into the diamond.

The shape of the diamond plate is then lithographically defined on the surface opposite to the nanopillar using a photoresist. After exposing and developing the photoresist, a layer of Titanium is thermally evaporated on the structured diamond surface. After lift-off of the photoresist mask, this layer acts as an etch mask for a dry etching process, which etches down all uncovered regions of the diamond. The Titanium layer is then removed, leaving behind arrays of individual diamond plates attached by weak joints to the substrate frame. Finally, the diamond surface is cleaned and oxygen terminated by boiling in a tri-acid mixture. After cleaning, the NV centers in the diamond plate arrays are characterized using a combination of optically detected magnetic resonance (ODMR), $g^{(2)}$ autocorrelation and count stability measurements. The best performing NV centers are selected for the fabrication of the AFM tips.

Our tips are sourced from [Qnami AG](#), which uses a diamond plate $19\text{ }\mu\text{m} \times 6\text{ }\mu\text{m}$ in size. These diamond plates are then detached from the substrate frame by breaking off the weak joints, and are attached to the end of a pulled quartz rod using a UV curable adhesive. The other end

of the quartz rod is attached to one prong of a quartz tuning fork. The tuning fork is electrically excited by an integrated piezoelectric in a Nanosensors™ Akiyama-probeⁱ footprint.

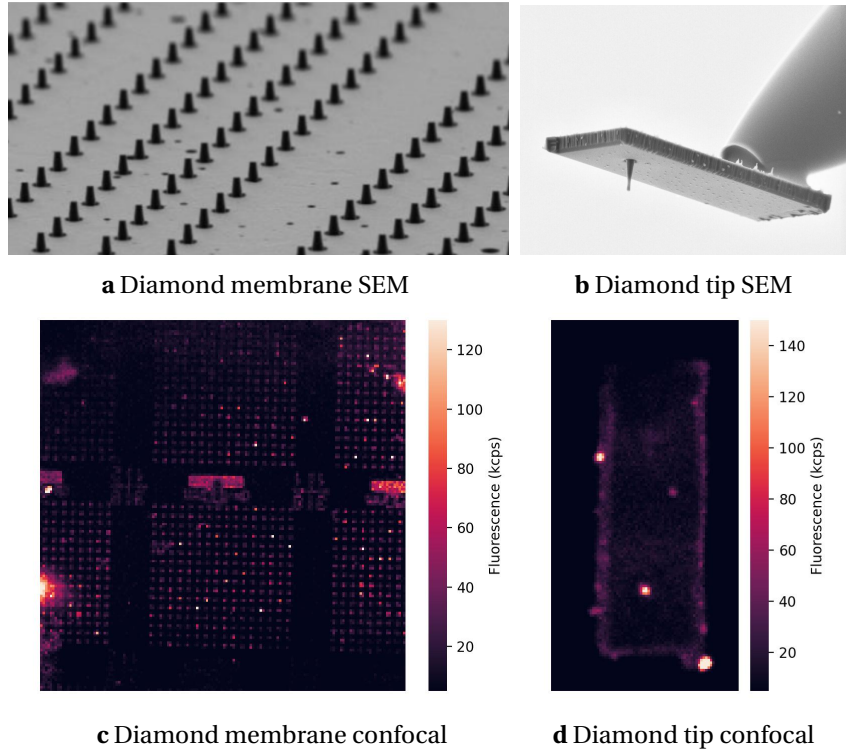


Fig. 1.2: Scanning electron microscopy (SEM) (a, b) and laser scanning confocal microscopy (c, d) images of NV centers in diamond membranes and diamond tips. SEM images from Momenzadeh et al. [9] and Garbini [10] respectively.

1.2 Initialization, control and readout

Once NV centers have been fabricated inside diamond, they need to be initialized, controlled and read outⁱⁱ. In the following sections, we derive the initialization and readout processes for NV centers starting from its ground state Hamiltonian. The control process is then derived by adding in an interaction and control Hamiltonians to the NV ground state Hamiltonian.

1.2.1 Ground state spin Hamiltonian

The pure diamond lattice has a tetrahedral symmetry, and belongs to the T_d point group. Introducing the NV defect into the lattice reduces the symmetry to the C_{3v} point group, whose symmetries are shown in Fig. 1.3a. Associated with the C_{3v} point group are three irreducible representations (or basis sets) – A_1 , A_2 and E . Each representation has a character under a symmetry element operation, which can be used to construct single electron orbital

ⁱThe Akiyama-probe was named after its inventor, Dr. Terunobu Akiyama, during his work at the University of Neuchâtel, Switzerland in 2001.

ⁱⁱInterestingly, NV centers used as quantum sensors meet 3 out of the 5 DiVincenzo's criteria¹¹ for constructing a quantum computer.

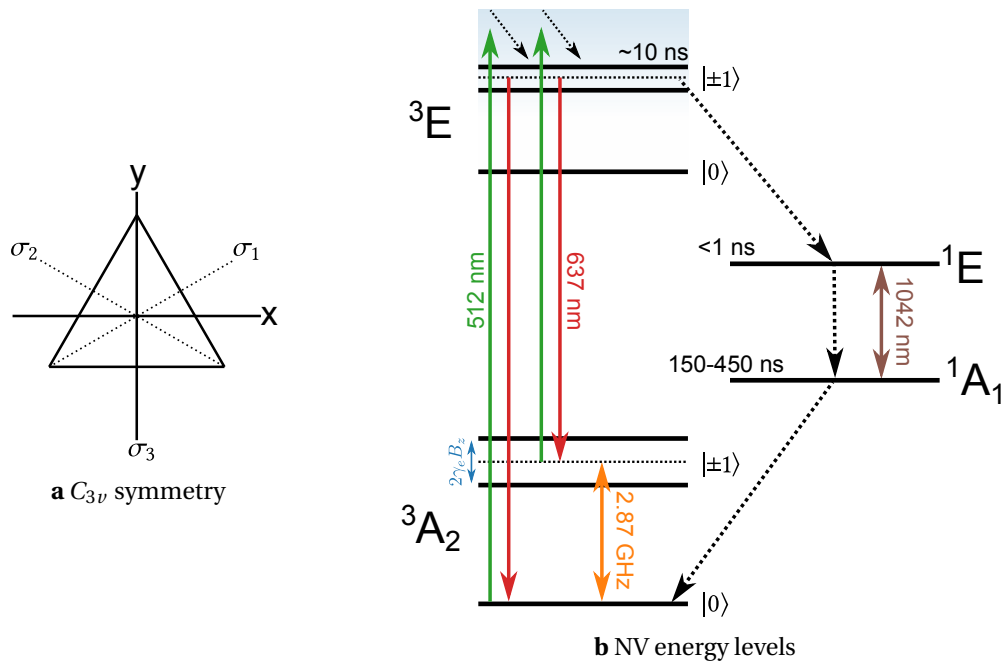


Fig. 1.3: **a** Mirror planes and rotation axes of the C_{3v} point group. The symmetry elements of C_{3v} are the identity operation $\{E\}$, three-fold clockwise and counter-clockwise rotations $\{C_3^+, C_3^-\}$, and mirror planes $\{\sigma_1, \sigma_2, \sigma_3\}$ (also referred to as $\{\sigma_d, \sigma_e, \sigma_f\}$ in certain works). **b** Simplified energy level structure of the NV center within the 5.5 eV diamond band gap. The 3A_2 and 3E configurations are spin triplets, and the 1A and 1E configurations are spin singlets.

representations. From the wavefunction representation of the dangling bonds, four single electron orbitals can be extracted — $a_1(1), a_1(2)$ of A_1 symmetry and e_x, e_y of E symmetry^{12,13}. The energetic ordering of the orbitals is done by finding a basis in which the electron-nuclear Coulomb interaction can be diagonalized. This basis is then used to develop the multi-electronic ground and excited state configurations.

The ground state of the NV center has six electrons with the orbital configuration given by $[a_1(1)]^2[a_1(2)]^2(e_x e_y)^2$. The first excited state is formed by exciting an electron (or de-exciting a hole) from $a_1(2)$ to e_x or e_y , resulting in the orbital configuration $[a_1(1)]^2[a_1(2)]^1(e_x e_y)^3$. Taking the Coulombic interaction of the system along with the anti-symmetric spatial configuration of the electrons, a ground state triplet is obtained with the 3A_2 configuration¹⁴. The excited state is also a triplet, with the 3E configuration. In between the ground and excited states, the singlet levels 1A and 1E are also present. The singlet levels are populated by an intersystem crossing (ISC) from the 3E manifold. The different configurations, state lifetimes and first order transitions are shown in Fig. 1.3b.

The complete ground state spin-Hamiltonian (Eq. 1.1 in units of \hbar) oriented in a magnetic field oriented along the NV axisⁱ includes descriptions of the electronic and nuclear spin-spin interactions, hyperfine interactions and interactions with magnetic and strain fields.

$$\mathcal{H}_{gs} = \underbrace{D_{gs}S_z^2 + E(S_x^2 - S_y^2)}_{\text{zero field and strain interactions}} + \underbrace{A_{\parallel}S_zI_z + A_{\perp}(S_xI_x + S_yI_y)}_{\text{axial and off axial hyperfine interaction}} + \underbrace{PI_z^2}_{\text{quadrupole interaction}} + \underbrace{\mu_B \mathbf{S} \cdot \bar{\mathbf{g}} \cdot \mathbf{B}}_{\text{electronic Zeeman interaction}} + \underbrace{\mu_N \mathbf{I} \cdot \bar{\mathbf{g}}_N \cdot \mathbf{B}}_{\text{nuclear Zeeman interaction}} \quad (1.1)$$

where,

- $\hat{S}_{\{x,y,z\}}$ electronic spin operators
- $\hat{I}_{\{x,y,z\}}$ nuclear spin operators
- \mathbf{B} static applied magnetic field

Under the assumption of low crystal strain, the lattice strain constant E (≈ 1 MHz¹⁵) is negligible compared to the zero field splitting.

For ${}^{14}\text{N}$ the perpendicular hyperfine constant A_{\perp} is -2.1 MHz to -2.7 MHz and the parallel hyperfine constant A_{\parallel} , is -2.1 MHz to -2.3 MHz¹⁵⁻²⁰, both of which are negligible compared to the zero field splitting.

The nuclear quadrupole for ${}^{14}\text{N}$ P is -4.8 MHz to -5.1 MHz¹⁵⁻²⁰ and can also be neglected.

The nuclear magneton μ_N is much smaller than the Bohr magneton μ_B ($\mu_N \approx 10^{-3} \mu_B$), so the electronic and nuclear Zeeman interaction can be approximated to a purely electronic

ⁱFor simplicity, we assume the NV axis is oriented along \hat{z}

interaction.

In the presence of a strong magnetic field $\mathbf{B} = B_z$, the g-factor tensor \bar{g} can be reduced to its components parallel to z .

Making the above approximations, a simplified expression for the ground state spin-Hamiltonian (in units of \hbar) is obtained.

$$\mathcal{H}_{gs} = D_{gs} \hat{S}_z^2 + \mu_B g_{\parallel} B_z \hat{S}_z \quad (1.2)$$

1.2.2 Optical pumping and fluorescence contrast

To readout the NV center, the ground state ${}^3A_2 |0, \pm 1\rangle$ sublevels are off-resonantly optically excited to the 3E manifold in a spin preserving transition. The excited 3E state has a lifetime of ≈ 10 ns, after which its population decays via two possible channels — (i) a photonic de-excitation into the NV 3A_2 ground state around the ZPL at 637 nm, *or* (ii) an ISC into the singlet 1A and 1E states. In general, the probability of the $|\pm 1\rangle$ sublevels decaying via the ISC channel is $\approx 30\%$ higher than the $|0\rangle$ sublevelⁱ. Conventional optical cycling results in a contrast of around 25 %²¹, and by optimizing the laser power and pulse time to maximize shelving into the NV singlet states whilst minimizing two-photon ionization, can be extended up to 33 %²². Note that these are purely *optical* initialization and readout methods. Using spin-to-charge conversion methods the contrast can be further increased to 42 %²².

After undergoing an ISC, the population is shelved for 150 ns to 400 ns in the singlet 1A_1 state, during which no photonic emission around the NV ZPL takes place. This leads to a photoluminescence (PL) rate difference between the ground state sublevels, which forms the basis for NV spin state readout. Fig. 1.4 shows the PL as a function of time, with a 3 μ s long 515 nm laser pulse applied at 150 ns. At short excitation times, a clear PL contrast is present between the $|0\rangle$ and $|\pm 1\rangle$ sublevels. At longer excitation times the spin populations undergo optical pumping into ${}^3A_2 |0\rangle$, as the sublevel is preferentially populated via both the photonic de-excitation and the ISC channels. This forms the basis for NV spin state initializationⁱⁱ, where at longer excitation times in Fig. 1.4, the PL of the “bright” and “dark” levels converge.

1.2.3 Control and interaction Hamiltonians

In section § 1.2.1 a simplified spin-Hamiltonian for the NV center ground state was developed. In this work, the NV is used as a magnetic field sensor. To actually perform the sensing operation two additional interactions are important – the interaction of the sensor with an oscillating control field, *and* the interaction of the sensor with the magnetic field of the system.

ⁱThe difference in probabilities is caused by an enhanced spin-orbit coupling between triplet ${}^3E | \pm 1 \rangle$ states and the metastable singlet states

ⁱⁱThis scheme allows for $\approx 90\%$ spin polarization of the NV center at room temperature

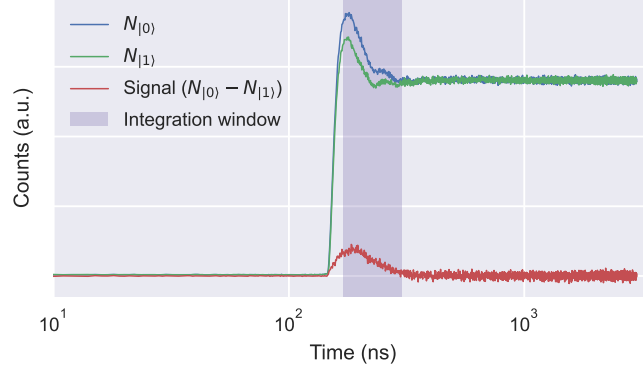


Fig. 1.4: Timetrace of NV counts (in arbitrary units) on application of a 515 nm laser pulse. The integration window is used to compute the NV spin state using the scheme described in [Appendix A.1](#).

Control Hamiltonian Control over the NV sensor can be achieved by MW driving fieldsⁱ. NV spin state transitions can be driven by control fields perpendicular to the static field. This can be realized by a control Hamiltonian \mathcal{H}_c . Under the assumption of a static magnetic field along the z -axis, [Eq. 1.3](#) represents a general form of a control Hamiltonian.

$$\mathcal{H}_c = \mu_B g_{\perp} [B_x \sin(\omega_x t) \hat{S}_x + B_y \sin(\omega_y t) \hat{S}_y] \quad (1.3)$$

Interaction Hamiltonian The interaction of the NV center with the system to be sensed can be described by a magnetic dipolar interaction \mathcal{H}_i . The interaction consists of a single NV center having ground state spin \mathbf{S} and gyromagnetic ratio γ interacting with N spin species having spins \hat{S}_j with gyromagnetic ratios γ_j located at distances r_j from the NV center.

$$\mathcal{H}_i = \frac{\mu_0}{4\pi} \sum_{j=1}^N \frac{\hbar \gamma \gamma_j}{r_j^3} [3(\mathbf{S} \cdot \hat{r}_j)(\hat{S}_j \cdot \hat{r}_j) - \mathbf{S} \cdot \hat{S}_j] \quad (1.4)$$

In the limit where the Zeeman shift is much larger than both the hyperfine interaction and magnetic interactions, [Eq. 1.4](#) can be reduced to [Eq. 1.5](#), where θ_j is the angle between the vector joining the two spins and the external magnetic field.

$$\mathcal{H}_i = \frac{\mu_0}{4\pi} \sum_{j=1}^N \frac{\hbar \gamma \gamma_j}{r_j^3} [1 - 3 \cos^2(\theta_j)] \quad (1.5)$$

ⁱThe frequency of the driving field depends on the Zeeman shift of $|0\rangle \leftrightarrow |\pm 1\rangle$

1.3 Optically detected magnetic resonance (ODMR)

Now that we have a theoretical understanding of how to initialize, control and readout an NV center, we can ask the question of how to use this information to perform a measurement. In this section, we will discuss the measurement technique of optically detected magnetic resonance (ODMR). ODMR is a technique that allows for the detection of a magnetic field by measuring the frequency shift of a microwave-driven transition. The technique is based on the fact that the transition frequency is shifted in proportion to the applied magnetic field, which can be measured by a microwave spectrometer. A measurement performed using this technique is shown in Fig. 1.5.

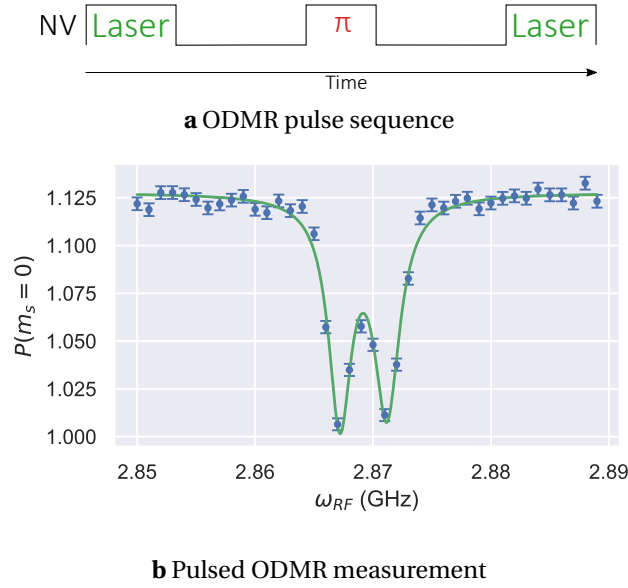


Fig. 1.5: **a** Laser and MW pulse sequence used in pulsed ODMR. **b** Pulsed ODMR measurement on a single NV center in a diamond tip. Error bars indicate photon shot noise. Data fit to a double Lorentzian dips corresponding to the $|0\rangle \leftrightarrow |+1\rangle$ and $|0\rangle \leftrightarrow |-1\rangle$ transitions.

In this work we use pulsed ODMR, i. e. the laser and microwave pulses are applied at distinct times from one another. In pulsed ODMR, the spin state is initialized by a $\approx 3 \mu\text{s}$ laser pulse, and subsequently manipulated by $\approx 100 \text{ ns}$ microwave pulses. The spin state is read out by another $\approx 3 \mu\text{s}$ laser pulse. During the spin manipulation period, no laser radiation is applied. This allows for a measurement robust against laser power and frequency instabilities. The manipulation is also coherent, as the spin-state remains unchanged between the spin manipulation pulsesⁱ.

The microwave is swept over a range of frequencies, and the spin state will only be modified when the frequency of the microwave pulse matches the transition frequency of the $|0\rangle \rightarrow \pm|1\rangle$ spin states. A π -pulse is realized when the duration and power of the pulse is sufficient to flip the NV between the $|0\rangle \leftrightarrow \pm|1\rangle$ states. The line width of this transition can be estimated by the Fourier product of the rectangular π -pulse profile and the Gaussian profile of width $1/T_2^*$.

ⁱWithin the limits of NV spin coherence time T_1 , or phase coherence time T_2

The maximum magnetic field sensitivity of the NV center depends primarily on two factors – the *number* and the *coherence time*, of the NV centers. As the number of NV centers increases, so does the total phase pickup, effectively leading to higher sensitivities. However, this also generally has the effect of lowering the coherence times due to dipole-dipole couplings between the NV centers. Sensitivity can be roughly expressed by $\eta \approx 1 \text{ nT}/\sqrt{N\tau}$, where N is the number of NV centers, and τ is the coherence time. Sensitivity itself has the units of $\text{T}/\sqrt{\text{Hz}}$, or in other words, the minimum magnetic field detected after 1 s of integration. DC sensitivity is limited by the T_2^* coherence time, or in other words, the time for which the NV can maintain a coherent phase relation in a superposition state. AC sensitivity is limited by the T_2 coherence time, where a refocusing pulse is applied while the NV is in a superposition state. The refocusing pulse effectively creates a filter envelope around $1/\tau$, and can be adjusted to tune out incoherent noise.

Generally speaking, T_2 is around two orders of magnitude larger than T_2^* , and thus AC sensitivity is much higher than DC sensitivity. Table 1.1 shows the sensitivity of the NV center for different number of NVs N and coherence times.

N	Single NV 1	Single NV (<i>iso.</i>) 1	NV ensemble 10^{11} ($100 \mu\text{m}^3$)
T_2^*	1 μs	228 μs	20 μs
T_2	300 μs	2 ms	50 μs
η_{dc}	1 $\mu\text{T}/\sqrt{\text{Hz}}$	20 nT/ $\sqrt{\text{Hz}}$	1 pT/ $\sqrt{\text{Hz}}$
η_{ac}	20 nT/ $\sqrt{\text{Hz}}$	4 nT/ $\sqrt{\text{Hz}}$	1 pT/ $\sqrt{\text{Hz}}$

Table 1.1: Magnetic field sensitivity of NV centers^{4,5,21,23–26}. Coherence times are typical values, and may differ based on the exact NV preparation method. N refers to the number of NV centers, and *iso.* refers to isotopically purified ^{12}C diamond samples.

1.4 ODMR pulse sequences

The last two letters of ODMR, *MR* or *magnetic resonance*, yield a huge amount of power. Intensive research over the past several decades has gone into developing and refining magnetic resonance techniques. These techniques were mostly applied to ensembles of spins, such as ensembles of nuclear spins in the human brain, measured using magnetic resonance imaging (MRI)ⁱ. These sequences work (nearly) as well when applied to single spin systems such as the NV center. Core to magnetic resonance is the ability to sequence measurements in time. In simple terms, it means controlling the spin state in such a way that we can tune the sensor to specifically measure the quantity of interest. In the following sections, we will briefly discuss the most relevant ODMR sequences for this thesis. In most cases, the initialization and readout laser pulses are similar in length to the ODMR sequence described previously, and are $\approx 3 \mu\text{s}$. The microwave pulse is $\approx 100 \text{ ns}$.

ⁱFun fact: MRI was originally called NMRI (nuclear magnetic resonance imaging), but “nuclear” was dropped to avoid negative associations from the general public.

1.4.1 T_1 relaxometry

The T_1 pulse sequence is used to measure the spin relaxation of the sensor spin. The idea is to initialize the sensor spin, wait for time τ , and then readout the spin state. The final state after reading out has the transition probability $p(\tau) \propto [1 - \exp(-\tau/T_1)]$, where T_1 is the spin relaxation time. The T_1 time represents the probabilistic limit for which the spin system maintains a non-Boltzmann or a polarized spin distribution.

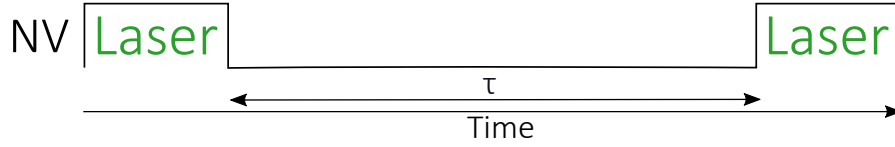


Fig. 1.6: The T_1 pulse sequence.

1.4.2 Ramsey T_2^* relaxometry

The Ramsey sequence is used to measure static magnetic perturbations. The measurement involves putting the sensor in a superposition state $|+\rangle = (|0\rangle + e^{-i\phi}|1\rangle)/\sqrt{2}$ via a $\pi/2$ pulse, leaving it to evolve for some time τ , then applying another $\pi/2$ pulse to project the spin state back to the sensor basis. The phase pickup ϕ is given by $\phi = \int_0^\tau dt' \gamma B(t')$, where γ is the coupling constant and $B(t')$ is the stray magnetic field. The final state after reading out has the transition probability $p(\tau) \propto \exp(-\tau/T_2^*) [1 - \cos(\omega_0\tau)]$, where T_2^* is the Ramsey coherence time. Measuring $p(\tau)$ gives rise to oscillatory Ramsey “fringes” from which the coupling between the spin sensor and the magnetic perturbations can be determined.

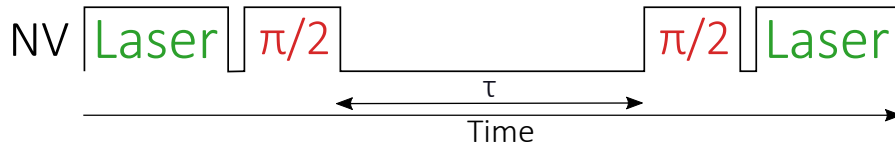


Fig. 1.7: The Ramsey pulse sequence.

1.4.3 Hahn-echo T_2 relaxometry

To cancel the effects of static perturbations on a Ramsey measurement, an additional π pulse is applied midway through the superposition sequence. This has the effect of refocusing the signal, and effectively creates a filter envelope around $1/\tau$, and can be adjusted to tune out incoherent noise. The net phase pickup in this case is $\phi = \int_0^{\tau/2} dt' \gamma B(t') - \int_{\tau/2}^\tau dt' \gamma B(t')$. The Hahn-Echo measurement determines T_2 , the time required for the amplitude of the echo signal to fall to $1/e$ of its initial value.

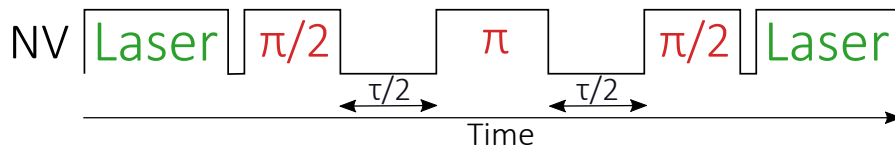


Fig. 1.8: The Hahn-Echo pulse sequence.

1.4.4 Double electron electron resonance (DEER) spectroscopy

External spins coupled to the sensor spin with coupling strength γ can be sensed using the double electron-electron resonance (DEER) sequence. In addition to performing a Hahn-Echo sequence on the sensor spin, a π pulse with frequency ν is applied to the external spin. The external spin generates magnetic signal $V(t)$. When ν matches the resonance of an external spin system, the NV experiences a net phase pickup $\phi = \int_0^{\tau/2} dt \gamma V(t) + \int_{\tau/2}^{\tau} dt \gamma V(t)$

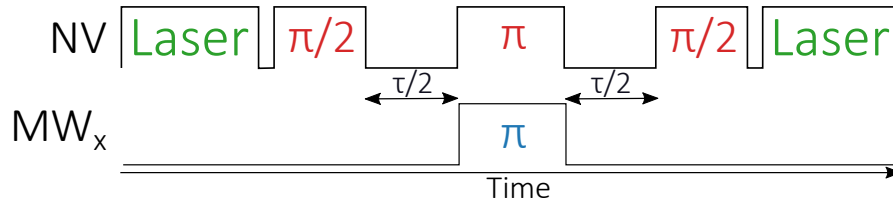


Fig. 1.9: The DEER pulse sequence.

1.5 NV scanning probe microscopy (NV-SPM)

As described in the previous sections, NV centers in diamond are highly sensitive and versatile magnetic field sensors. However, most magnetic materials of interest show a spatial variation in their magnetization. Understanding this spatial variation is critical to understanding the underlying physics of the material. This is where NV scanning probe microscopy (NV-SPM) comes in. NV-SPM is a technique that combines the NV's magnetic field sensitivity with a scanning probe microscopy (SPM), allowing us to generate raster magnetic stray field maps of the sample.

atomic force microscopy (AFM)ⁱ is a technique which is used to study materials in a surface-sensitive manner with high spatial resolution, even down to the atomic scale^{28,29}. It works by using a tiny, sharp probe to scan the surface of a sample, and detecting the atomic-scale forces between the probe and the sample. The basic operating principle of AFM involves using a cantilever with a sharp tip attached at the end. The cantilever is very thin and flexible, allowing it to bend in response to the forces acting on the tip. As the tip is moved across the surface of the sample, the forces acting on the tip change, causing the cantilever to bend accordingly. This deflection is measured by a piezoelectric element through a change in the voltage output, which is monitored and used to construct a high-resolution topography of the sample surface³⁰.

In NV-SPM, a standard piezoelectric AFM holder with a quartz tuning fork is used. A diamond plate containing a single NV nanopillar is attached at the end of one of the prongs (the fabrication of this plate has been described in § 1.1). With this configuration, we get the combination of the AFM's high-resolution imaging capability and the NV center's magnetic field sensitivity.

AFM can be operated in a variety of modes, the choice of which is conditional on the tip

ⁱThe first AFM was constructed by Binnig, Quate and Gerberin in 1986 and used a diamond tip attached to a flexible cantilever²⁷.

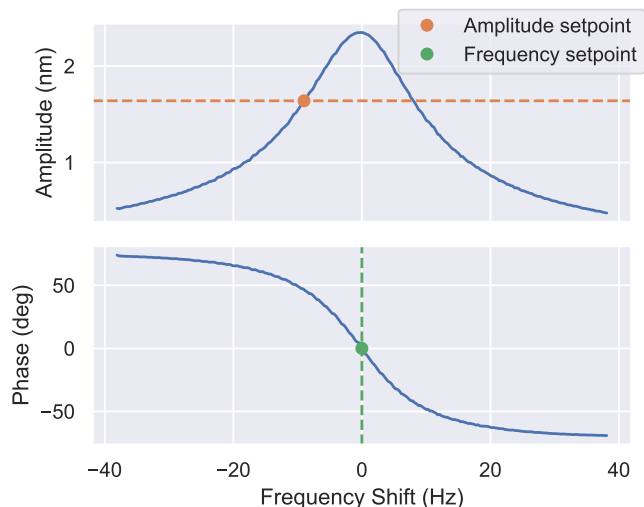


Fig. 1.10: AFM resonance curve of a NV-AFM tip in free space. The observed Q-factor, calculated from the slope of the phase shift around the resonance frequency, is 1834. In amplitude modulation mode the amplitude set point is set at $\approx 70\%$ of peak amplitude (dotted orange line). In frequency modulation, the frequency set point is set to the resonance frequency of 31.28 kHz (dotted green line).

and sample, along with the environmental conditions. In this work, for ambient pressure measurements we operate in intermittent-contact mode AFM and for vacuum measurements we operate in non-contact mode AFM. The modulated parameter in both cases is either amplitude or frequency.

Amplitude modulated intermittent-contact mode AFM At ambient conditions, a layer of water is present on the sample surface. When the tip is brought near the sample surface it can “stick” to the water meniscus, causing a sudden drop in tip oscillation amplitude. The drop in amplitude is compensated by a sharp response from the z phase locked loop (PLL) modulating based on the amplitude (response time ≈ 1 ms). This is performed in amplitude modulation mode, where the set point is set to $\approx 70\%$ of the peak amplitude of the tip oscillation (Fig. 1.10). Frequency modulated mode is unlikely to work in this case, as the tip oscillation frequency change is large and will likely fall out of the range of the FM-PLL.

Frequency modulated non-contact AFM At ultra-high vacuum (UHV) conditions, the tip is operated in frequency modulated mode, where the set point is set to the resonance frequency of the tuning fork. When the tip is near the sample surface, the long range Van der Waals interaction between the tip and the sample causes a change in the tuning fork resonance frequency (Fig. 1.10). This change in resonance frequency is compensated by a response from the z phase locked loop (PLL) modulated based on the frequency (response time ≈ 1 ms).

2 Readout & control of an endofullerene electronic spin

Most of my advances were by mistake.
You uncover what is when you get rid of
what isn't.

R. Buckminster Fuller

Parts of this chapter are published in

D. Pinto, D. Paone, B. Kern, T. Dierker, R. Wieczorek, A. Singha, D. Dasari, A. Finkler, W. Harneit, J. Wrachtrup, and K. Kern, “Readout and control of an endofullerene electronic spin”, [Nature Communications](#) **11**, 6405 (2020)

The endofullerene N@C₆₀ is formed by a single nitrogen atom (¹⁴N) sitting at the center of a C₆₀ fullerene cage, also known as a buckyball cage. The nitrogen atom remains isolated at the centrosymmetric I_h position inside the rigid carbon cage and retains its single-particle eigenvalues, in particular its electronic ground state quartet^{32,33}. These properties have led to it being proposed as an isolated, controllable and scalable qubit^{34–36}. However, the qubit spin state readout has proven to be extremely challenging, with results remaining inconclusive^{37,38}. In this chapter, the first readout and control of single N@C₆₀ spins using the NV center is demonstrated. Lower limits on coherence times are also reported along with quantitative estimates on the spin-spin coupling.

Author contributions

D. Pinto drop-coated the N@C₆₀ on the diamond, characterized the NV centers, and performed control measurements with support from D. Paone and B.K. D. Pinto, D. Paone., and B.K. performed the single-spin EPR measurements at LT-UHV under the supervision of J.W. and K.K. R.W. under the supervision of W.H. synthesized the N@C₆₀ samples and performed ensemble EPR measurements. D.D. and T.D. performed theoretical calculations and simulations. D. Pinto performed the analysis and drafted the manuscript, with contributions from all authors.

2.1 Structure and synthesis

N@C₆₀ is produced by the low-energy implantation of ¹⁴N inside C₆₀, as illustrated in Fig. 2.1a. The process is described well in Zhou and Porfyrakis [39]. To summarize, an effusion cell is used to sublimate a thin C₆₀ film on a copper target. During the formation of this film, the copper target is bombarded by ¹⁴N ions from an ion source. A fraction of these ions enter the C₆₀ cages to form N@C₆₀. The ion implantation process yields a filling factor (N@C₆₀/C₆₀) of around 10⁻⁴. To further separate the N@C₆₀ from C₆₀, high pressure liquid chromatography (HPLC) methods are used. HPLC utilizes the small difference in molecular weights and polarizability of the two species to separate them. N@C₆₀ is characterized using x-band cw-EPR, shown in Fig. 2.1b, where it shows a hyperfine coupling strength of 15.97 MHz.

The encapsulated nitrogen in the fullerene cage behaves like an atomic system inside a neutral molecular trap. Within a fixed cage geometry, the energy of the encapsulated N atom increases continuously as it moves away from the high symmetry I_h central site³². This well-shielded electronic spin (S=3/2) has prompted several proposals for fullerene-based quantum information processing systems^{35,40}. The spatial confinement within the C₆₀ cage leads to a reduction of volume available for the atomic wave-function, resulting in a net compression the ¹⁴N wavefunction. This is evidenced by a roughly 50% enhancement of the hyperfine coupling constant as compared to the free atomic value⁴¹. The electronic spin degeneracy of the spin 3/2 system is lifted by a static external field, giving rise to four electronic spin states $m_S = \pm 3/2, \pm 1/2$. The ¹⁴N nucleus ($m_I = 0, \pm 1$) introduces a hyperfine splitting to the lines, leading to 12 energy levels in total. The transitions are triply degenerate, as shown in Fig. 2.1b, where all transitions with the same color are degenerate.

The EPR spectrum of N@C₆₀ is shown in Fig. 2.1b. The sharp lines indicate very long relaxation times, with $T_1 \sim 1$ s at $T \sim 7$ K and $T_2 \sim 20 \mu\text{s} \sqrt{T}$ ⁴⁰. The primary decay mechanism is not from zero-field splitting modulation (a characteristic of $S \geq 1$ systems⁴¹) but from unresolved dipolar couplings³⁵.

2.2 Ground state spin Hamiltonian

Once single ¹⁴N atoms are encapsulated inside C₆₀ cages, we can write down a first approximate Hamiltonian for the ground state spin system. Eq. 2.1 represents the ground state spin-Hamiltonian (in units of \hbar).

$$\mathcal{H}_{gs} = \underbrace{D(\hat{S}_z^2 - 5/4)}_{\text{zero field interaction}} + \underbrace{A\hat{S}_z\hat{I}_z}_{\text{hyperfine interaction}} + \underbrace{\mu_B g_e B_z \hat{S}_z + \mu_N g_N B_z \hat{I}_z}_{\text{electronic and nuclear Zeeman interactions}} \quad (2.1)$$

where,

- \hat{S}_z electronic S=3/2 spin operator
- \hat{I}_z nuclear I=1 spin operator
- B_z magnetic field across N@C₆₀

2.2 Ground state spin Hamiltonian

The zero-field interaction (zfi) originates from a dipolar interaction between the three constituent electrons of ^{14}N . It is heavily dependent on cage symmetry. For a C_{60} cage of icosahedral (I_h) symmetry, the zfi is zero. However, larger zfi valuesⁱ can be engineered using chemical functionalization of the C_{60} cage^{42,43}. For the Zeeman interactions, the nuclear magneton μ_N is much smaller than the Bohr magneton μ_B . Thus the approximation to a purely electronic Zeeman interaction can be made.

Making the above approximations, Eq. 2.2 represents an effective spin-Hamiltonian (in units of \hbar).

$$\mathcal{H}_{gs} = A\hat{S}_z\hat{I}_z + \mu_B g_e B_z \hat{S}_z \quad (2.2)$$

The ground state energy level structure is shown in Fig. 2.1c. An EPR measurement is shown in Fig. 2.1b.

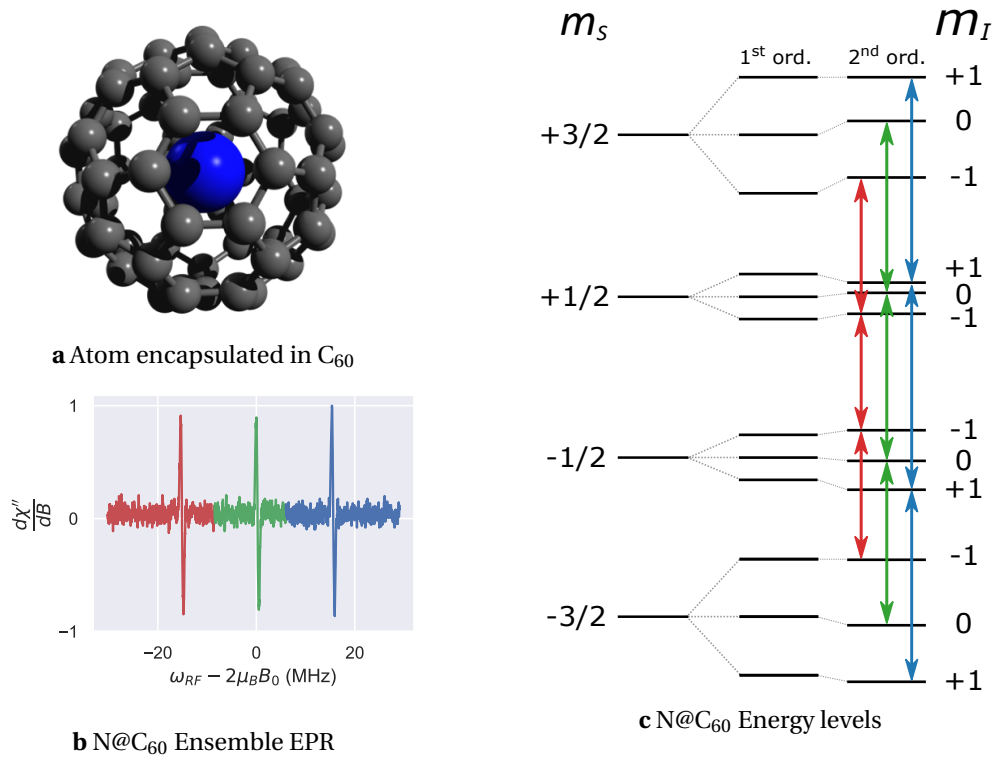


Fig. 2.1: **a** Artistic visualization of a C_{60} cage with a single encapsulated atom. **b** Ensemble $\text{N}@\text{C}_{60}$ EPR spectra measured in solution. **c** Energy level scheme of $^{14}\text{N}@\text{C}_{60}$ ground state ($S = 3/2, I = 1$) for a C_{60} cage with icosahedral symmetry and second order corrections of order $A^2/(\gamma_e f B) \approx 1$ MHz. Colors indicate transitions between spin states with $m_I = -1$ (red), $m_I = 0$ (green) and $m_I = +1$ (blue).

ⁱCurrently up to 30 MHz.

2.3 Preparing the sensor and system

Before performing the measurement, we need to prepare the N@C₆₀ solution to maximize the probability that a single N@C₆₀ cage is in the vicinity of an NV center, and isolate suitable NV centers for measurement. The following sections detail the steps taken during preparation of the sensor and the sample.

Preparing the NV sensor

The NV centers are implanted in a CVD type-IIa diamond grown along the [100] axis. Fabricated diamond nanopillars act as cylindrical waveguides with an apex and base diameter of 400 nm and 700 nm respectively, and a height of 1000 nm. Each pillar can be individually identified using labeling markers etched on the diamond surface. The depth of the NV centers is primarily governed by the implantation energy of ¹⁵N, which is varied from 2.5 keV to 10 keV. For sensing purposes, near-surface NV centers with long coherence times are desirable. The measurements in this work are performed on NV centers implanted at an energy of 5 keV, leading to an NV depth of around (5 ± 1) nm from the diamond surface⁴⁴.

The diamond surface is cleaned of any molecular adsorbates and the surface dangling bonds are oxygen terminated via boiling in a three acid mixture (equal parts of Nitric, Sulfuric and Perchloric acid) for a period of 4 h. The NV centers are then characterized at normal temperature and pressure (NTP). From the large set of available NV, suitable ones are shortlisted. To determine suitable NV centers for sensing, the following four criteria is applied. The NV should,

- i. be single, measured by $g^{(2)}$ -coherence function dip < 0.5 ,
- ii. be stable, measured by photo-luminescence bleaching or blinking,
- iii. have Hahn-Echo coherence $T_2 \geq 10 \mu\text{s}$,
- iv. allow for fast spin manipulation ($t_\pi \leq 150 \text{ ns}$), at reasonable driving power

Preparing the N@C₆₀ spins

The goal in this experiment is to demonstrate the coupling of single NV centers to single N@C₆₀ spins. To achieve this, a rough quantitative calculation is performed to estimate the concentration of N@C₆₀ required for coupling at the single spin level. To summarize, N@C₆₀ powderⁱ with a filling factor (N@C₆₀:C₆₀) of 10^{-4} is dissolved in a toluene solution at NTP, after which 1 μL of solution at a concentration of $0.1 \mu\text{mol L}^{-1}$ is drop-coated on the diamond surface and left to dry at NTP.

2.4 Double electron-electron resonance (DEER) spectroscopy

Once the sensor and sample have been prepared, they are transferred into a low temperature and ultra-high vacuum setup for measurement⁴⁵. We begin by developing a simple interaction Hamiltonian for the combined NV-N@C₆₀ spin system. Denoting the interacting spins as S_{nv} (NV electronic spin), S_{ef} (endofullerene electronic spin) and I_{ef} (endofullerene nuclear spin),

ⁱThe N@C₆₀ samples used in this work were produced and purified by M.Sc. René Wiczorek in the group of Prof. Wolfgang Harneit, University of Osnabrück, Germany

2.4 Double electron-electron resonance (DEER) spectroscopy

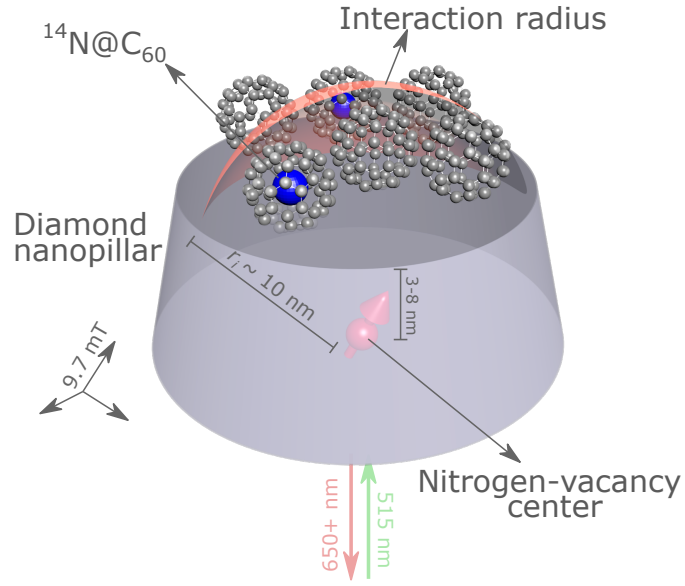


Fig. 2.2: Artistic visualization of single near-surface NV center with a disordered network of empty (C_{60}) and filled ($N@C_{60}$) cages within its interaction radius. The filling factor of the C_{60} cages in the experiment is $\approx 10^{-4}$. The NV is initialized and readout by pulsed 515 nm laser excitation. Spin control is achieved with a 20 μm thick gold wire near the diamond surface (not shown).

and applying a static magnetic field $\mathbf{B}_0 = B_0 \hat{z}$ aligned to the NV quantization axis, the spin Hamiltonian (in units of h) of the system reads as:

$$\hat{\mathcal{H}} = \hat{\mathcal{H}}_{\text{nv}} + \underbrace{\gamma_{\text{ef}} \hat{B}_0 \hat{S}_{\text{ef}} + A \hat{S}_{\text{ef}} \hat{I}_{\text{ef}} + D \hat{S}_{\text{ef}} \hat{S}_{\text{ef}}}_{\hat{\mathcal{H}}_{\text{ef}}} + \underbrace{J \hat{S}_{\text{nv}} \hat{S}_{\text{ef}}}_{\hat{\mathcal{H}}_{\text{nv,ef}}} \quad (2.3)$$

Here $\gamma_{\text{ef}} = g\mu_B/h \approx 28 \text{ GHz/T}$ is the gyromagnetic ratio of the endofullerene electronic spin, $|A| \approx 15.87 \text{ MHz}$ is the isotropic hyperfine coupling of the encapsulated ^{14}N , and $|D|$ is the zero-field interaction strength appearing in the absence of perfect icosahedral cage symmetry⁴⁶. The interaction Hamiltonian $\hat{\mathcal{H}}_{\text{nv,ef}}$ assumes higher external fields B_0 relative to the hyperfine interaction A and dipole-dipole interactions J i.e. $\gamma_{\text{ef}} B_0 \gg A \gg J$. The dipole-dipole coupling strength $|J| = \mu_0 \hbar \gamma_{\text{nv}} \gamma_{\text{ef}} / (2r^3) \approx 52 \text{ MHz} / (r/\text{nm})^3$ varies with NV and endofullerene separation r (in nm)³⁴.

The dipole-dipole interaction was probed at several single NV centers using pulsed double electron-electron resonance (DEER) spectroscopy^{23,47}. DEER spectroscopy utilizes periodic microwave (MW) pulses in a spin-echo sequence to preserve the phase coherence and enhance the magnetic field sensitivity of the NV center^{48,49}. The central spin-flip of the NV center is synchronized with a radio-frequency (RF) spin-flip pulse in a lock-in scheme. When the frequency of the RF pulse matches the transition frequency of an external spin, the NV center

basis states pick up a relative phase proportional to the magnetic field of the external spin. To increase the net phase pickup and suppress common mode noise, we chose the $m_s = \{\pm 1\}$ NV electronic spin sub-levels as sensor basis states²³. This double-quantum (DQ) pulse schemeⁱ is shown in Fig. 2.3a.

Fig. 2.3b center upper panel shows the single-spin EPR spectrum of N@C₆₀ at 4.7 K under an external magnetic field of 9.697 mT. The spectrum is obtained on averaging many individual single-shot experiments, and therefore represents a temporal average in which the N@C₆₀ spin system assumes all allowed configurations with a probability given by the temperature, and possibly by saturation effects due to finite shot repetition times. Three resonance peaks at 251.5(5), 271.4(1) and 288.7(7) MHz mark the hyperfine splitting of the endofullerene nitrogen. Note that after cleaning the diamond surface, the signal disappeared completely, indicating that the signal stems from the surface and not from impurities within the diamond itself.

The side transitions have an asymmetric splitting from the central transition, with splittings of (19.8±0.7) MHz and (18.1±1.7) MHz for the lower and upper transitions respectively. A possible cause of this is that drop coating the N@C₆₀ on the diamond surface introduced a deviation from the I_h cage symmetry, leading to a preferential orientation of the endohedral spins. This would manifest itself as an asymmetric hyperfine interaction as the broken symmetry favors a certain hyperfine axis. This is further evidenced by a slight increase in hyperfine splitting as compared to EPR measurements, as the lowering of cage symmetry introduces a weak zero field splitting into the endohedral system. The central peak has roughly twice the amplitude of the side peaks, likely indicating the presence of an additional hyperfine-less parasitic spins in the surroundings. The resolution does not allow for resolving any internal hyperfine structure (to the second order).

Comparing single-endofullerene EPR (Fig. 2.3b center upper panel) with ensemble measurements (Fig. 2.3b bottom panel) on the same sample reveals good agreement between the central and upper hyperfine components. However, the single-endofullerene EPR spectrum shows two additional features – (i) the lowest-energy hyperfine transition is shifted downwards by ≈4 MHz, and (ii) the EPR line widths are broadened. Both of these experimental features can be modeled using second-order perturbation theory (discussed in Appendix B), and the result of the simulation is shown in Fig. 2.3b center upper panel, as a solid blue line. Firstly, the position of the three peaks can be best reproduced by using an isotropic hyperfine constant of 19 MHz for the spin-3/2 species instead of the usual 15.85 MHz, and an axial zero-field splitting (parameterized as D in Eq. 2.3) of 1.52 MHz. The former shifts the frequency of the hyperfine satellites relative to the central peak and the latter leads to an additional splitting within each hyperfine line.

The apparent enhancement of these parameters may be due to either covalent^{50–52} or non-covalent⁵³ chemical interactions between the fullerene and the diamond surface. The simulation uses an overall line broadening of 4 MHz, which is in agreement with the typical experimental power broadening expected from Fourier transformed 100 ns RF pulses

ⁱIn the DQ scheme, the NV sensing basis is switched from $|0, -1\rangle$ to $|\pm 1\rangle$.

2.4 Double electron-electron resonance (DEER) spectroscopy

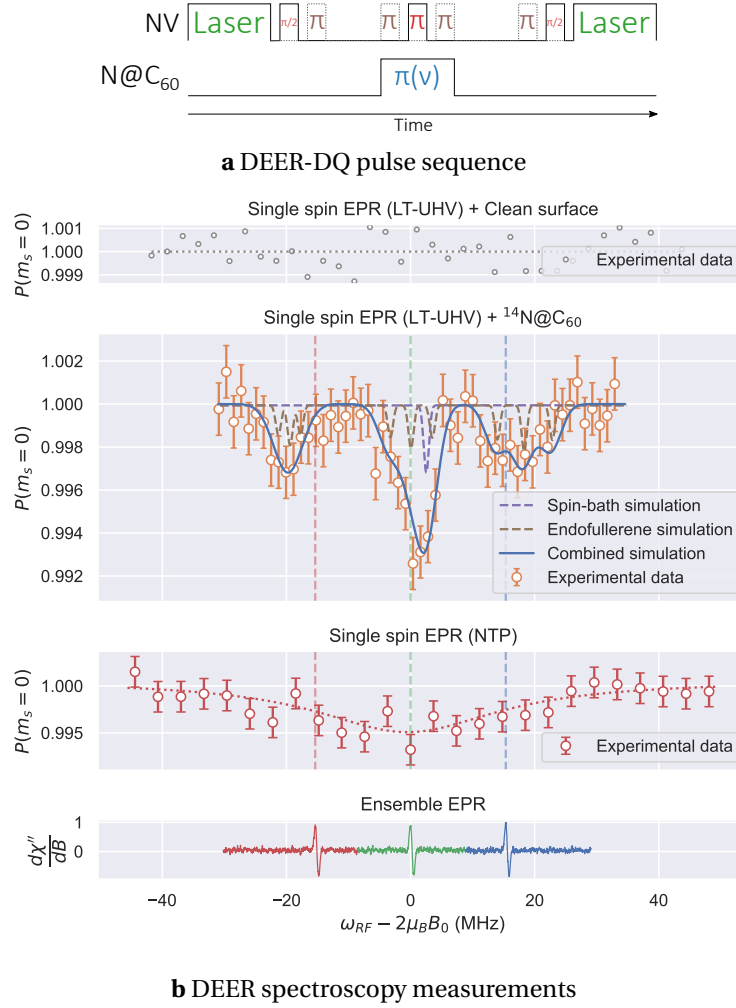


Fig. 2.3: **a** Single-spin electron paramagnetic resonance (EPR) realized using double electron-electron resonance (DEER) in the double quantum (DQ) basis. Brown pulses (dotted lines) and red pulses (continuous lines) address $|0\rangle \rightarrow |+1\rangle$ and $|0\rangle \rightarrow |-1\rangle$ NV transitions respectively. **b** *Top panel*, Low-temperature DEER-DQ spectroscopy on a clean surface. *Center upper panel*, Low-temperature DEER-DQ spectroscopy on a surface coated with N@C₆₀. The dashed brown and purple lines indicate the simulated spectrum of a single N@C₆₀ and weakly coupled spin-bath ($g = 2.03$) respectively (line widths reduced to 1 MHz for clarity). The solid blue line indicates the combined simulation with experimental line width. The simulated endofullerene has an isotropic hyperfine constant $a = 19$ MHz, axial zero-field splitting $D = 1.52$ MHz and a static magnetic field $B_0 = 9.687$ mT. Dotted vertical lines indicate positions of ensemble EPR hyperfine components. Error bars depict photon shot noise. *Center lower panel*, Spectrum decays under room-temperature (RT) thermo-optical load, dotted red line indicates fit to single Lorentzian model. Error bars depict photon shot noise. *Bottom panel*, Ensemble solution EPR data on the same N@C₆₀ sample measured across $\approx 10^9$ spins.

$1/(\pi \times 100\text{ns}) \approx 3.3\text{MHz}$. The peak intensities are modeled considering a weak coupling to a spin-bath ($g = 2.03$), which may originate from electronic spins in the drop-coated solution^{54,55}. Another possible interpretation of the single-endofullerene EPR peak intensities can be made by invoking non-thermal spin distributions, potentially caused by the NV inter-system crossings during laser excitation (see [Appendix B](#)).

At 4.7 K, we could observe the single-spin EPR signal over weeks, and N@C₆₀ itself is known to be thermally stable up to 550 K. However, when placing N@C₆₀ under the exposure of strong laser irradiation, ensemble experiments have demonstrated that it can undergo thermo-optical decay at temperatures well below 550 K⁵⁶. To test this, we raised the temperature of the system to 300 K and repeated the DEER measurement. We observe a complete suppression of any discernible side peaks along with the formation of a broad featureless central dip ([Fig. 2.3b](#) center lower panel). This behavior is consistent with previous attempts at room temperature endofullerene spin readout under laser irradiation³⁷. Ensemble EPR measurements have attributed the decay mechanism to the formation of a radical species in an adiabatic photo-reaction⁵⁷. Another possibility is the thermally-assisted rapid de-phasing of an intact N@C₆₀ spin.

2.5 N@C₆₀ spin control and relaxation

The sensor relaxation times can provide crucial information about the environment, such as the distance to a dipolar coupled spin. To determine the distance of the endofullerene from the NV center, we make a direct comparison of the temporal evolution of the NV phase pickup with and without a spin-flip on the central N@C₆₀ spin transition.

The spin-echo sequence on the NV center shown in [Fig. 2.4a](#) mainly refocuses the phase imprinted by nearby spins (i.e. a strongly coupled spin-bath), and the simple decoupling sequence does not affect the de-phasing caused by farther spins (i.e. a weakly coupled spin-bath). Hence the long-time behavior is unaffected by the π -pulse. As we start to flip the N@C₆₀ spin, depending on the time-scale of the phase evolution, the NV center either dominantly de-phases due to its coupling to the N@C₆₀, or to the weakly coupled spin-bath. This behavior is seen in [Fig. 2.4b](#), where a strong initial de-phasing due to the NV-N@C₆₀ interaction slowly relaxes to the de-phasing caused by the spin-bath. Hence the difference between the two de-phasing curves should display the expected behavior, i.e., a transition from a faster de-phasing caused by external spins towards a slower de-phasing from the local spin-bath.

Using a simple rate-equation model⁴⁷, we extract an NV-N@C₆₀ coupling strength of $\approx(0.29 \pm 0.02)\text{MHz}$ from the initial linear de-phasing, corresponding to an NV-N@C₆₀ separation $\approx 5.6(1)\text{nm}$. Considering the possibility of the additional presence of a finite number (<10) of unknown bath spins, the uncertainty in distance measurements is affected with an additional error bar of $\pm 1\text{nm}$.

The de-phasing and relaxation times of N@C₆₀ were long enough to generate and measure spin coherence, as shown by the Rabi oscillations (pulse sequence [Fig. 2.5a](#)). The Rabi nutation of the endofullerene spin is demonstrated in [Fig. 2.5c](#). Rabi oscillations are recorded by fixing

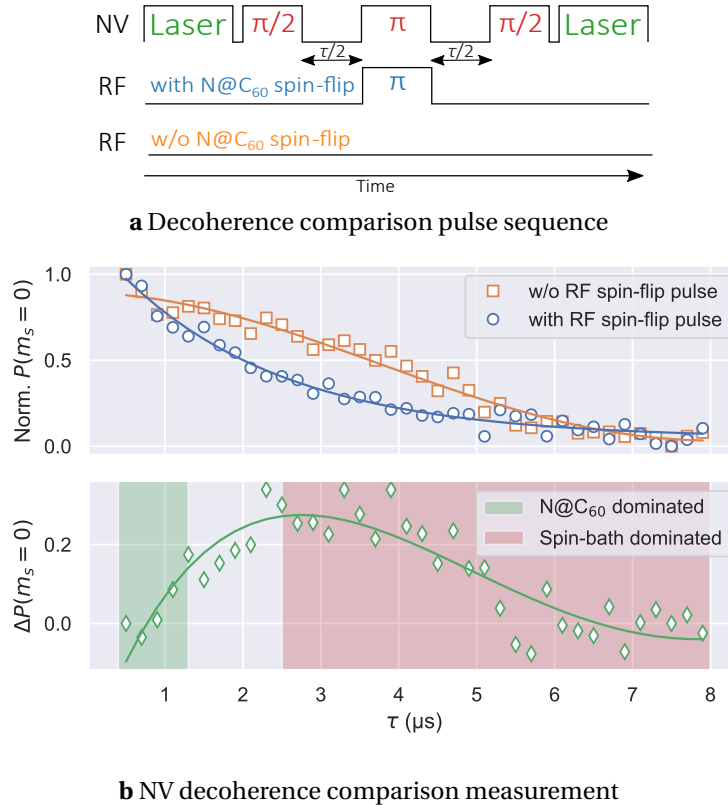


Fig. 2.4: **a** Pulse sequence comparing NV center Hahn-Echo decoherence in presence (first RF sequence) and absence (second RF sequence) of an RF spin-flip on N@C₆₀.

b *Top panel*, Direct comparison of the temporal evolution of the NV Hahn-Echo signal with and without a spin-flip on the coupled N@C₆₀.

Bottom panel, Difference in NV center decoherence at short evolution times versus longer evolution times reveals the clear separation of timescales at which the NV-N@C₆₀ interaction is dominant.

the RF frequency at the central ($m_I = 0$) and upper ($m_I = +1$) peaks in Fig. 2.3b center upper panel, and varying the pulse duration time τ . The Rabi frequency displays the characteristic square-root scaling with driving power (Fig. 2.5b). The Rabi control allows for rapid pulsed control of the endofullerene spin-level populations, with spin-state switching rates tunable up to $\nu_R = (12.47 \pm 0.01)$ MHz.

The $|m_I = 0\rangle$ oscillations have a higher contrast (1%) as compared to $|m_I = +1\rangle$ (0.4%). Accounting for equivalent measurement time in both cases, the difference in contrast is consistent with the spectroscopic measurements. The difference in Rabi periods is accounted for by noting that the RF driving power differ by around 5 dBm, with the $|m_I = +1\rangle$ transition driven at higher power. The Rabi period alone, however, is not sufficient as a figure of merit. A more suitable figure of merit is *how many* spin flip operations can be performed within the decay time $T_{1\rho}$ ⁱ of the spin system. Based on the analysis, it can be concluded that $|m_I = +1\rangle$ is preferable for performing spin operations as it is not influenced by hyperfine-less parasitic spin systems in the environment.

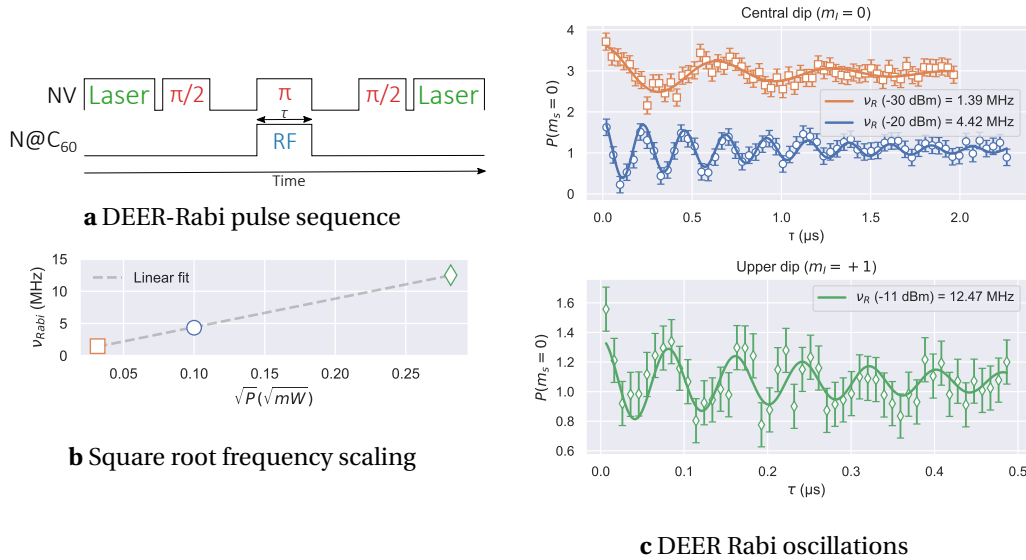


Fig. 2.5: **a** Pulse scheme for driving Rabi oscillations on endofullerene spins and probing with a single NV center. **b** Characteristic square-root behavior of Rabi frequency with RF driving power. **c** Rabi oscillations on the endofullerene central ($m_I = 0$) and upper ($m_I = +1$) hyperfine components. Solid line is fit to an exponentially decaying sinusoid. Error bars indicate photon shot noise.

2.6 Coherence of N@C_{60} spins

The previous section covered relatively simple quantum operations. For the practical use of N@C_{60} , a more general approach to quantum operations is required. A practical way to achieve generality is to measure how long the quantum system can hold phase coherence. To measure

ⁱ $T_{1\rho}$ stands for the T_1 in the rotating frame, as the system is under RF driving.

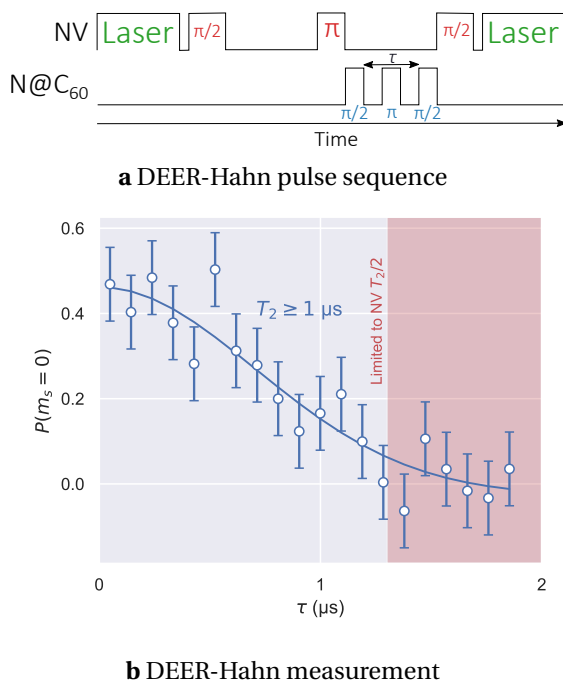


Fig. 2.6: **a** Pulse scheme for probing endofullerene spin-echo phase coherence. **b** Spin-echo measurements place a lower limit of $T_2 \geq 1 \mu\text{s}$ on the phase coherence times. Solid line indicates exponentially decaying sinusoidal fit, error bars indicate photon shot noise.

this, we performed a spin-echo on the endofullerene within half of the free evolution time in the NV spin-echo (Fig. 2.6a). The result is a characteristic Hahn decay in Fig. 2.6b, with an observed decay time of $C_{60} \geq 1 \mu\text{s}$. For NV centers with a spin-echo coherence of $T_2^{NV} \approx 2.5 \mu\text{s}$, this leads to a maximum measurable coherence time of $T_2^{NV}/2 \approx 1.25 \mu\text{s}$. Thus the time represents a lower limit on N@C₆₀ coherence due to the measurement being constrained to a single branch of the NV spin-echo. The maximum measured ensemble endofullerene coherence time is around $190 \mu\text{s}$ ⁵⁷, and thus probing and controlling such spins requires near-surface NV centers with significantly longer coherence times. This can be achieved through the chemical surface modification of diamond, or by doping the diamond with n-type impurities⁵⁸.

2.7 Conclusion

In conclusion, we have demonstrated electron spin resonance with readout and control on the endofullerene $^{14}\text{N}@C_{60}$ using a near-surface nitrogen vacancy center in diamond. The surface adsorption on to the diamond surface appears to enhance isotropic hyperfine constants and zero-field splitting of the fullerene cage. The use of fullerenes such as $^{31}\text{P}@C_{60}$, which has hyperfine interactions an order of magnitude larger than $^{14}\text{N}@C_{60}$, may permit spin control without strong surface effects. Recent advances in C₆₀ self-assembly, or fullerene packed CNTs, opens a path for scaling endofullerene systems⁵⁹. Furthermore, the nuclear spin of the encapsulated atom allows for nuclear quantum memories interfaced with electron spin

Chapter 2. Readout & control of an endofullerene electronic spin

“buses”^{60,61}. This can be realized with pulse schemes such as Hartman-Hahn, which transfer polarization from the NV center to the endofullerene electronic and nuclear spins. Combining these techniques together open up incredibly exciting possibilities of building large-scale endofullerene quantum machines⁶².

3 Construction of a low-temperature & ultra-high vacuum NV-SPM

Premature optimization is the root of all evil.

Donald Knuth

In the previous chapter we demonstrated the readout and control of single endohedral fullerenes using NV centers in diamond. However, the measurement also demonstrates the limitations of having a “fixed” NV center. We relied on the statistical distribution of N@C₆₀ to find one within the sensing radius of an NV center. This required measuring double electron-electron resonance on ≈ 40 NV centers in total, and finding the N@C₆₀ within the sensing radius of one of them. Not only is this tedious, but it also limits us from performing measurements on more interesting systems like 1D arrays of N@C₆₀ spins packed into a carbon nanotube³⁵, or even using the self-assembly properties of C₆₀ to create a structured 2D array of N@C₆₀ spins⁵⁹.

We can be freed of such limitations by combining the NV with a scanning probe microscope (SPM). The SPM allows us to rapidly generate a topographical map of the sample surface, and then use the NV to generate magnetic raster maps of the regions on interest. In this chapter, we describe the construction of a novel NV scanning probe microscope operating at low temperature and ultra high vacuum. The goal of this system is to explore the novel and sensitive spin-phenomena underlying magnetic structures. In particular, the physics of frustrated magnetic ordering⁶³, domain walls⁶⁴, (anti)-skyrmions⁶⁵, merons⁶⁶, multi-ferroics⁶⁷ and single molecules^{31,35}. The construction of the setup proved to be highly challenging, but is both timely and of broad interest to both the quantum materials and nitrogen vacancy communities.

3.1 Setup goals and constraints

Exploring such a wide array of magnetic systems poses significant experimental challenges, as the physics of these materials strongly depends on their environment. To be useful, the setup must be capable of operating over a wide range of physical scales, which are listed below,

- *Pressure*, ambient $\rightarrow 10^{-10}$ mbar. For performing highly surface sensitive measurements, such as sensing spins in single molecules like $^{14}\text{N}@C_{60}$.
- *Temperature*, room temperature $\rightarrow 4.2$ K. For controlling the interplay of thermal and spin-spin interactions in correlated materials.
- *Vector magnetic field*, Zero-field $\rightarrow 1$ T. Like temperature, vectorial magnetic fields strongly affect the spin-spin interactions in correlated materials.

There is no system available on the market capable of supporting NV scanning probe magnetometry that can operate over these physical scales. In this chapter, we describe the design and construction of a new experimental system. We start by laying out the objectives required to achieve the above goals,

- Building a *measurement head* capable of nano-positioning a sample and tip, an AFM to maintain a constant sensor-sample separation, and allowing *in-situ* transfer of sample and tip, detailed in § 3.2.
- Building an *ultra-high vacuum* and *low temperature* system to operate at pressures $\sim 10^{-10}$ mbar and temperatures ~ 4.2 K, detailed in § 3.3 and § 3.4 respectively.
- Performing *laser scanning confocal microscopy* using a pulsed 515 nm laser with single photon detection from 650 nm to 750 nm, and the ability to perform second-order correlation measurements, detailed in § 3.5.
- Generating *pulsed microwave excitation* ranging from 2 GHz to 20 GHz with ~ 50 ns pulse lengths, detailed in § 3.6,
- Applying *vector magnetic fields* up to 1 T aligned along the quantization axis of the NV center, detailed in § 3.7.

Over the next sections, we go into each of these aspects of the system in detail, and describe the construction challenges and bottlenecks, along with the solutions we have implemented. To ensure reproducibility, we also provide an itemized list of the exact components used in the construction of the system.

3.2 Measurement head

The measurement head is the heart of the NV-SPM. It is primarily responsible for maintaining a constant separation between the sample and tip. A CAD diagram of the measurement head is shown in Fig. 3.1. It is composed of three main components: the *nano-positioning piezoelectric stage*, the *tip/sample stage*, and the *AFM preamplifier*.

3.2.1 Nano-positioning piezoelectric stage

For positioning the tip and sample with nanoscale precision, a combination of piezoelectric positioners and scanners are utilized. The positioners offer a wider range of motion, while the scanners offer higher resolution. The positioners utilize a slip-stick motion generated by a sawtooth waveform, where the voltage across the piezoelectric element is rapidly increased, causing it to slip, and then the voltage is turned off, causing it to stick. The scanners utilize a linear waveform, where the voltage is continuously increased, causing the piezoelectric

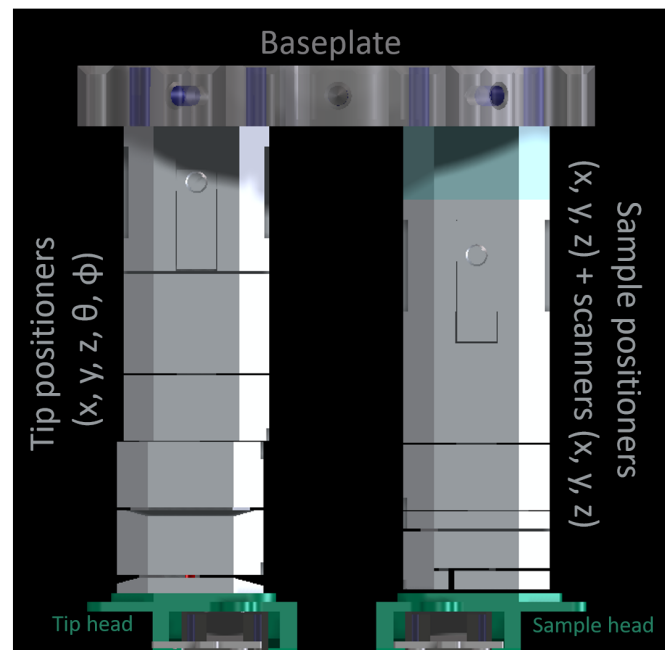


Fig. 3.1: CAD diagram of the piezoelectric stack on the measurement head, rendered in [PTC Creo](#). A list of the components used is shown in [Appendix C.1](#).

element to slip.

The positioners are used to move the sample and tip to the desired location, and the scanners are used to fine tune the position of the sample. In this system, the absolute position of the positioners is resistively encoded and read out using a closed-loop feedback controller (attocube ANC350). The piezoelectric motors are mounted in a stack configuration, where each subsequent motor is screwed into the previous. The top motor in the stack is mounted onto a fixed Titanium baseplate. To minimize the probability of the motors loosening over time due to vibrations, the motors are screwed into each other with split washers. However, after extensive operation, it is very likely that the motors will loosen. This is not a serious problem, however, as the motors can be easily re-tightened after dis-assembly. Note that this needs to be done cautiously, as over-tightening the screws can easily lead to permanent damage to the fragile piezoelectric motors.

The piezoelectric elements are composed of a PZT ceramic actuator encased in a Titanium body, which can operate at pressures of 10^{-11} mbar, temperatures from 1 K to 423 K, and magnetic fields up to 35 T. For the tip, we have 5-axis control over the position of the tip with positioners along (x, y, z, θ, ϕ) . (x, y, z) are the standard Cartesian coordinates, and (θ, ϕ) are the polar coordinates of the tip. For the sample, we have 3-axis control with positioners along (x, y, z) and 3-axis control with scanners along (x, y, z) .

The piezoelectric positioners need low resistance ($\leq 5 \Omega$) cabling to operate correctly. High resistance cabling smoothens out the sharp sawtooth waveform, resulting in non-linear ex-

tension and retraction during the slip-stick motion. We use 0.224 mm thick Copper wires for connecting the positioners, with an average resistance of $\leq 2 \Omega$ for ~ 2 m of cabling. The scanners, on the other hand, can function well with higher resistance wiring, and are connected with 0.125 mm thick Copper wires, with an average resistance of $\leq 5 \Omega$ for the same length of cabling.

To control the piezoelectric positioners we use two sets of controllers, with a switch-box to allow switching specific channels between the controllers. The attocube ANC350 controller is used for the positioners, as it contains a built in closed-loop feedback controller, allowing for absolute position readout. The position readout is factory calibrated and stored in a look-up table, which is loaded into the controller during measurement. The Nanonis™ SC4 + HVA4 controllers are used for the scanners, as they are fully integrated into the Nanonis™ software, where along with the OC4 controller they can easily perform atomic force microscopy measurements. We also occasionally use the Nanonis™ PMD4 for controlling the positioners, but in the open-loop configuration.

An itemized list of all the nano-positioning components used is given in [Appendix C.1](#).

3.2.2 Tip/sample stage

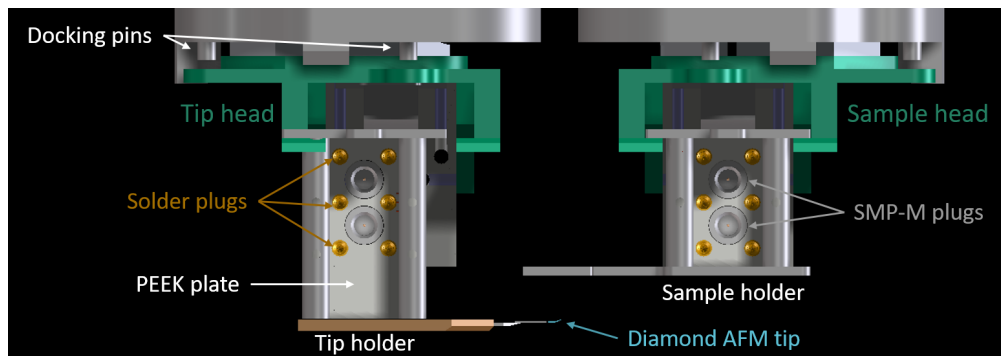
The base of the piezoelectric stage described in the previous section is connected to the tip/sample stage. The tip/sample stage consists of two main components – the *tip/sample head*, and the *tip/sample holder*.

Tip/sample head The head is screwed into the base of the piezoelectric stack, and is responsible for keeping the tip and sample holders in place as well as for supporting the tip/sample connector sockets. The tip/sample head is fabricated out of Type-5 Titanium and consists of two channels, whose width was chosen to support the Ferrovac flag style plate design⁶⁸. At the center of the channel a spring is mounted, this pushes down on the tip/sample flag plate, allowing it to sit firmly in position. The connector sockets are epoxied into a polyetheretherketone (PEEK) plate, which has holes drilled out for the connectors. The connectors will experience a longitudinal strain when a tip/sample is exchanged, and the epoxy needs to be able to withstand this strain. To this end, Torr-Seal® was the epoxy of choice, due to its UHV compatibility and high tensile shear strength (≈ 70 bar).

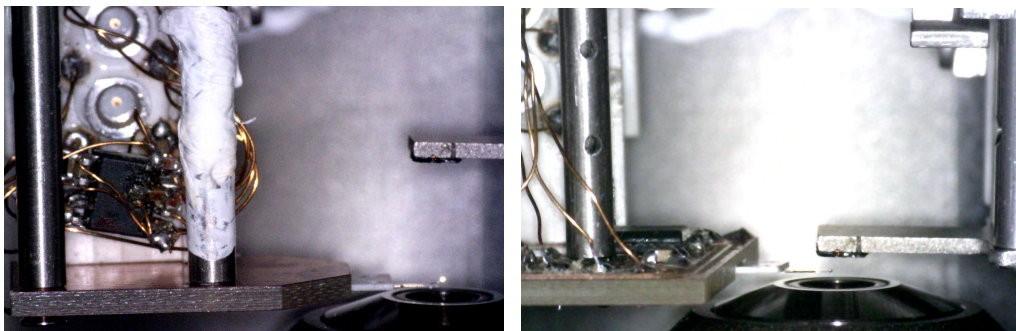
On each head, there are eight connector sockets in total: six crimp sockets (Allectra 212-PINF-25-S) and two SMP-M sockets (SV Microwave SF1132-6067). The six crimp sockets are crimped (using Allectra 214-CTOOL-HQ) to either 0.125 mm Copper wires or 0.15 mm Manganin wiresⁱ. The two SMP-M sockets are connected directly with custom manufactured SMP-M to SMA cables (Teledyne Stormflex® 047).

To minimize shear strain on the piezo stack during tip/sample exchange, the head is moved to a docking position. In the docking position, the head is driven into two pins fabricated on the

ⁱNote that for all non-coaxial cables in the setup, crimping was used wherever possible due to its excellent mechanical stability across a range of temperatures.



a Tip/sample CAD



b Separated configuration

c Integrated configuration

Fig. 3.2: a CAD diagram of the tip/sample head and holder, rendered in PTC Creo. Picture of the tip holder with an NV-AFM tip and preamplifier mounted in the separated (b) and integrated (c) mount configuration. In both cases the sample holder contains a multi-ferroic magnetic sample epoxied to the Titanium plate. A list of the components used is shown in Appendix C.2.

Titanium housing, effectively “locking” the position of the head, and preventing any motion along (x, y) axis. Note that despite this locking mechanism, tip/sample exchange is a complex process that requires great care and attention to avoid damaging the fragile piezoelectric stack. During tip/sample exchange the strongest (dis-)engagement force is applied by the two SMP-M sockets (~ 11 N). At ambient conditions there is a layer of water vapour on the socket surface lubricating the engagement and disengagement of the socket and plug. At UHV, this lubricant is not present. To ensure that the tip/sample exchange can be performed at UHV, a sharp knife can be used to slightly scrape down the surface of the socket, effectively reducing the engagement force and making tip/sample transfer safer.

Tip/sample holder The holder uses a Ferrovac flag style plate, manufactured out of Type-5 Titanium. The plate is mechanically held in place with a spring connected to the tip/sample head. The connector plugs are epoxied (again using Torr-Seal®) into a PEEK plate, which has holes drilled out for the connectors. On each holder, there are eight connector plugs in total, six solder plugs (Fischer Elektronik PK1G) and two SMP-M plugs (SV Microwave 1132-4005). The tip/sample holder can be exchanged *in-situ*, i. e. without breaking vacuum or temperature. The exchange is performed by grabbing the Ferrovac flag plate using a compatible pincer-grip wobble-stick (VAb MDWS-ZO 350). A CAD diagram of the tip/sample head and holder is shown in Fig. 3.2a.

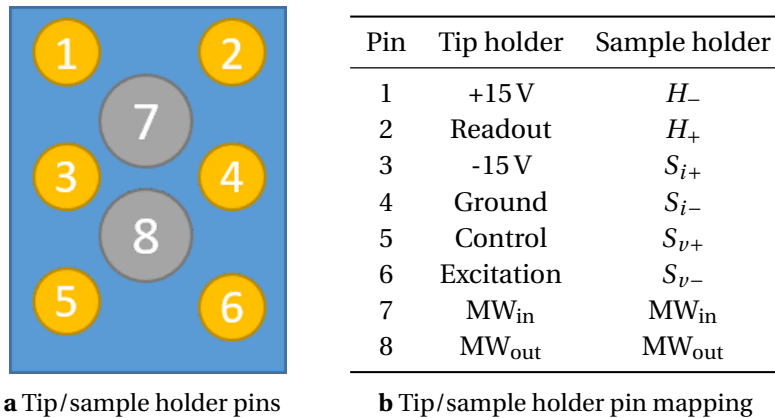


Fig. 3.3: **a** Numbered layout of the pins (viewed from the socket side) on the PEEK plate. Pins in gold are solder plugs (Fischer Elektronik PK1G) and pins in gray are SMP-M plugs (SV Microwave 1132-4005). **b** Pin mapping of the tip/sample holder. On the tip holder, the pins are primarily used for the AFM and AFM preamplifier. On the sample holder, pins 1 & 2 can be used for a sample heater and pins 3 – 6 can be used for a four-probe temperature sensor.

Tip holder The solder plugs are used for the AFM readout (R) and excitation (E) channels, along with preamplifier power supply ($V_+ = +15$ V, $V_- = -15$ V) channels, and the signals are referenced to ground channel (G). The SMP-M plugs are used for microwave input $MW_{tip, in}$ and output $MW_{tip, out}$. An image of the tip holder is shown in Fig. 3.2 and the layout is given in Fig. 3.3.

We use a star configuration \star , where all grounds in the system are connected to a reference ground. In our system, the reference ground is realized with a thick Copper plate screwed into the top of the cryostat, and also connects the ground of the Nanonis™ preamp power supply (AGND) and all cable shield ground. In most standard configurations, the star itself is connected to an Earth ground, which is usually a thick metal plate buried underground. However, in our testing, this actually leads to higher ground noise levels. We have found that the best way to reduce ground noise is to leave the grounding of the star open, which essentially means using the large metal body of the system itself acts as a reference ground. Note that in such a configuration it is important to ensure that there are no stray metal objects in contact with the system, as they can create ground loops.

The tip holder itself is modular, and can support a wide range of tip mounting configurations. We experimented with two main types of mounts – an *integrated mount*, where both the tip and AFM preamplifier are mounted on a custom designed PCB, and a *separated mount* where the tip is mounted on a PEEK plate and the AFM preamplifier is hanging. The separated mount is shown in Fig. 3.2b, and the integrated mount is shown in Fig. 3.2c. In both cases the circuit of the AFM preamplifier remains the same, as described ahead in § 3.2.3.

Sample holder The six solder plugs can be used to apply a DC/low-frequency signal to the sample. An example of this could be PID controlled feedback loop involving a sample heater (H_+ , H_-) and a four-probe temperature sensor (S_{i+} , S_{i-} , S_{v+} , S_{v-}). Another option is to apply (or measure) a voltage across or a current through the sample. The SMP-M plugs are used for microwave input $MW_{\text{sample, in}}$ and output $MW_{\text{sample, out}}$. An image of the sample holder is shown in Fig. 3.2 and the layout is given in Fig. 3.3. The sample itself can be mounted to the holder using a variety of methods. The simplest method is gluing the sample to the Titanium plate of the sample holder, we typically use GE Varnish (IMI 7031) due to its LT-UHV compatibility, along with it being thermally conducting and electrically insulating.

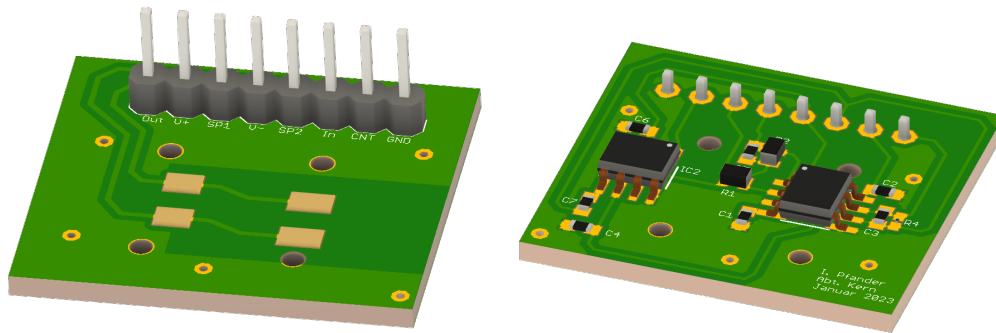
3.2.3 AFM preamplifier

The third and final component of the measurement head is the AFM preamplifier. It primarily serves three purposes:

- it acts as a trans-impedance amplifier, converting the small current signal from the AFM tip to a voltage signal
- it amplifies the voltage signal
- it compensates for parasitic capacitive coupling between the AFM excitation and readout channels

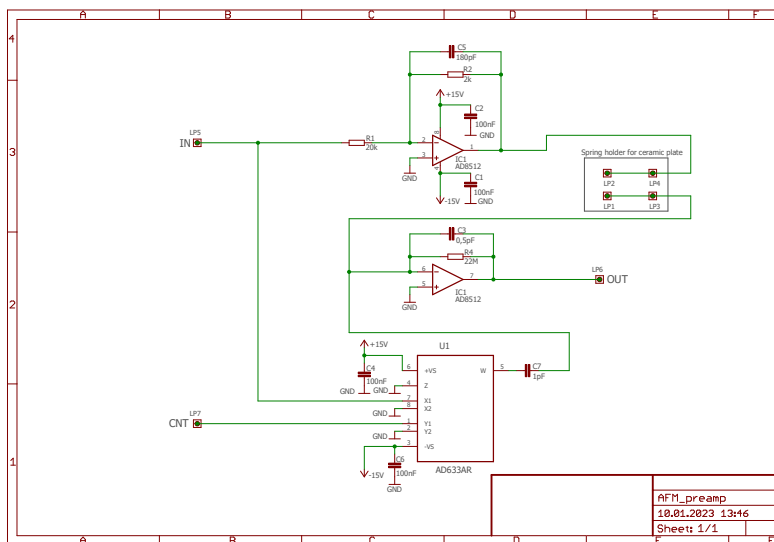
The AFM tip is electrically excited. In order to minimize noise pickup on the readout channel, the preamplifier needs to be mounted as close to the tip as possible. We mount the preamplifier on the tip holder itself, which gives the additional flexibility of performing *in-situ* preamplifier replacements in case of damage.

The preamplifier circuit diagram is shown in Fig. 3.4c, which is based on a reference circuit



a

b



c

Fig. 3.4: a, b Bottom and top of the AFM preamplifier rendered in Autodesk EAGLE. c Circuit diagram of the preamplifier. A list of the components used is shown in Appendix C.3.

implementation by Nanosensors©. The excitation signal (IN) is first split into two halves. The first half is attenuated by a factor of 1/10 on channel 2 of the AD8512 op-amp (IC₁) and sent to the excitation piezoelectric on the tip (LP₂), while the other half is sent to channel 7 of the AD633 op-amp (IC₂). The strength of the compensation is tuned by adjusting control voltage CNT on channel 1 of IC₂. The output of the compensation circuit is combined with the readout piezoelectric on the tip (LP₁). The resulting signal is sent to channel 6 of the IC₁ op-amp for amplification. Post amplification, the output signal (OUT) is sent through ≈2 m Copper wires to a buffer amplifier located outside the cryostat. The buffer amplifier has unit gain, and only performs impedance matching, after which the signal is passed through a high-pass filter (>22 kHz passband) and sent to the Nanonis™ OC4 input channel.

Both IC₁ and IC₂ op-amps are powered by the same ±15 V power rails, and are capacitively coupled to the ground by 100 nF capacitors. The DC power source is the Nanonis™ OC4, ensuring the supply is grounding to AGND. The capacitive coupling of the power rails to ground is necessary to suppress any AC component of the power supply voltage. The IC₂ compensation circuit works by inverting half of the input (IN) and adjusting its phase using control voltage CNT and a 1 pF capacitor connected in series. This inverted signal is added to the readout channel to cancel out any effects of parasitic coupling between the excitation and readout channels at the tip.

The input voltage (IN) is set in the range of 1 V to 3 V, which implies a voltage of 50 mV to 150 mV at the excitation piezoelectric of the tip. The resulting output voltage (OUT) is around 20 mV. This small output voltage can be a problem for less efficient AFM controllers, as the analog-to-digital (AD) converter might be unable to fill the full range of the input voltage. This is generally not an issue for the Nanonis™ OC4, as it has an inbuilt gain of 0.1 to 1000 before the signal is sent to a 14-bit AD converter sampling at 40 MSs⁻¹. However, if necessary, a secondary stage amplifier such as a FEMTO® DLPVA-100-BLN-S can also be added.

3.3 Low temperature

Material	Thermal conductivity WmK ⁻¹		Thermal expansion 10 ⁻⁶ K ⁻¹	Electrical resistivity 10 ⁻⁸ Ωm
	300 K	10 K		
Phosphor bronze	67	1.7	18	16
Copper	400	1500	17	1.7
Manganin	22	1	19	48
Titanium	22	0.5	9	42
Macor	1.5	0.8	0.9	-
Aluminum	35	0.9	8.5	2.8
PEEK	0.26	0.24	72	-

Table 3.1: Thermal and electrical properties of materials used in the construction of the system⁶⁹⁻⁷¹.

The base temperature of the system is realized using a bath style cryostat. The cryostat consists

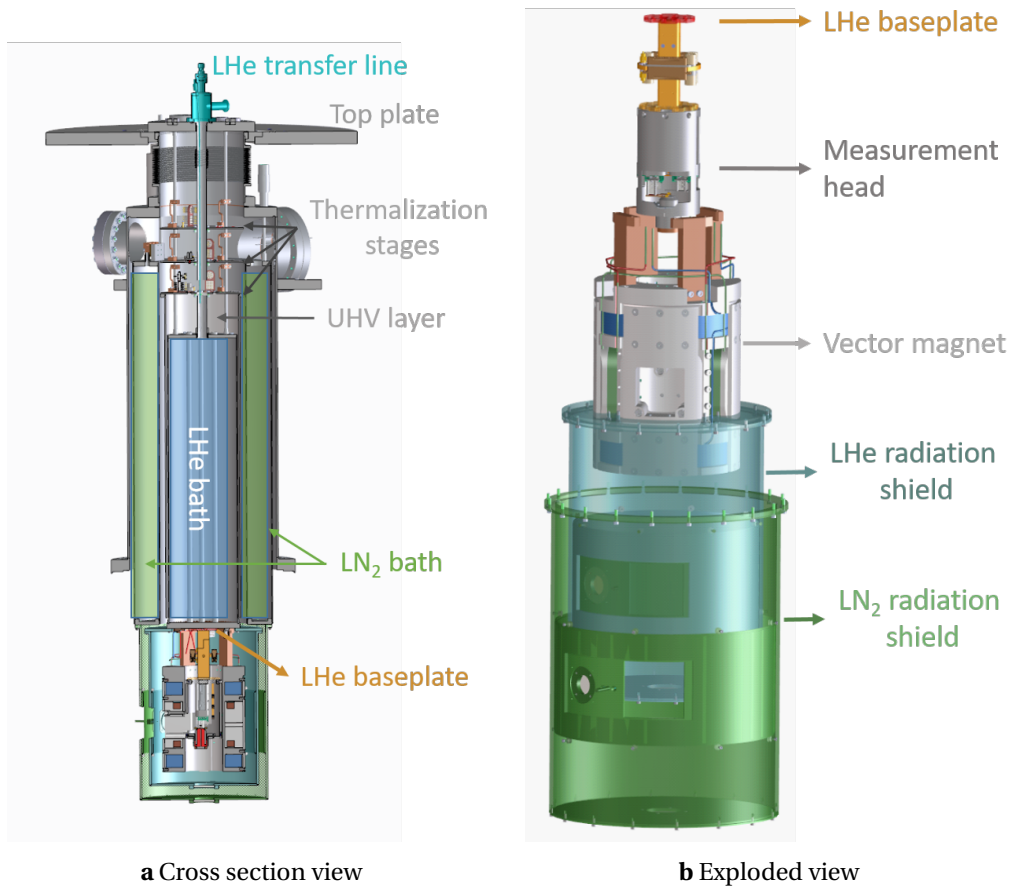


Fig. 3.5: **a** Cross section view of the cryostat highlighting the LHe bath which is cooled to 4.2 K and the LN₂ bath which is cooled to 77 K. **b** Exploded view of the cryostat base, showing the measurement head which is surrounded by the 3-axis vector magnet. The LHe and LN₂ radiation shields are thermally coupled to the LHe bath and LN₂ bath respectively.

of an inner core, composed of a 13.3 L liquid Helium-4 bath, and an outer core, composed of a 33 L liquid Nitrogen bath. The Helium insert i. e. Helium cryostat and the measurement head, is a distinct unit, and can be removed from the system without disturbing the Nitrogen cryostat. Note that this does require disconnecting the magnet thermalization leads via the inspector flanges, which is discussed further in § 3.7.

The outer body of the cryostat is manufactured from stainless steel. The thermal conductivity of SS, along with other materials used in the setup is given in Table 3.1. Furthermore the region between the inner and outer cores of the cryostat is evacuated to ultra-high vacuum. Due to this design there are two primary heat transfer mechanisms into the system – *thermal radiation* from the environment and *thermal conduction* through the electrical wiring.

Thermal radiation into the measurement head is minimized by the use of dual radiation shields, which are thermalized at LHe and LN₂ temperatures respectively. The radiation shields are manufactured from Aluminum and expose the measurement head to an effective radiation background of around 4.2 K. The shields feature a window mechanism, which can be opened or closed by a separate wobble-stick (VAb STWS-150). The window is opened during tip/sample transfer, and closed during measurement. The NV tip is initialized and readout optically, and to allow for optical access into the system, the base of each shield has a view port. The view ports have an applied anti-reflective coating from 525 nm to 975 nm.

Despite these measures, the cylindrical radiation shields are still relatively large, with the LN₂ shields ($h = 418\text{ mm}$, $r = 153\text{ mm}$) having a surface area of $\approx 0.47\text{ m}^2$, and the LHe shields ($h = 368\text{ mm}$, $r = 130\text{ mm}$) having a surface area of $\approx 0.35\text{ m}^2$. While the large shields are necessary to accommodate the large vector magnet, they have a deleterious effect on the overall hold-time of the system.

Thermal conduction into the measurement head via electrical wiring is minimized by a careful selection of materials. As was described in § 3.2.1 and § 3.2.2, the piezoelectric positioners, piezoelectric scanners and the AFM readout/excitation channels use either 0.224 mm or 0.125 mm thick single strand Copper wires. The temperature sensor leads are connected to the measurement head via 0.127 mm four-strand twisted-pair Phosphor Bronze wires. All remaining non-coaxial wires in the system are made out of 0.15 mm thick single strand Manganin wires. Both Manganin and Phosphor Bronze have a relatively low thermal conductivity and moderate electrical resistance, making them highly suitable for low temperature cabling. For MW transmission, the coaxial cables are made out of 1.4 mm thick Copper wires (Stormflex® 047).

There are a total of 96 non-coaxial wires in the system, and to reduce the thermal load on the cryostat, each wire is broken and thermalized at four different locations along the cryostat. The first three breaks happen at the cryostat baffles, and use a custom built Copper thermalization stage screwed into the baffle, as shown in Fig. 3.6b. The last break happens at the LHe baseplate.

There are a total of 4 coaxial wires in the system. These are not broken at the baffles, but are

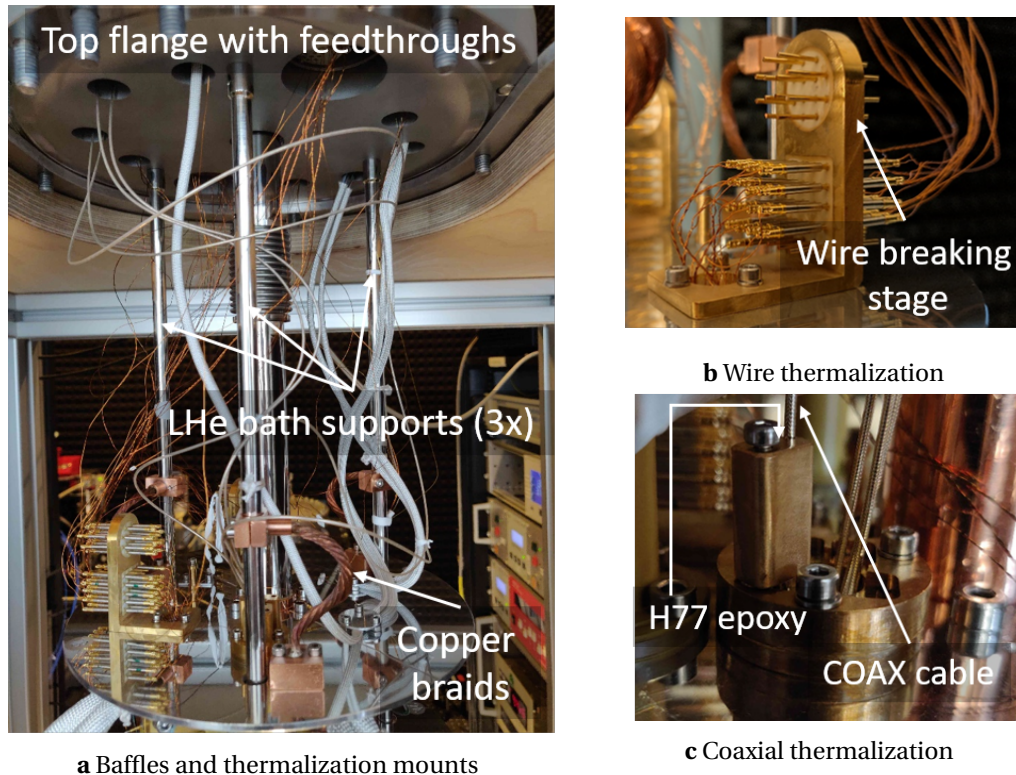
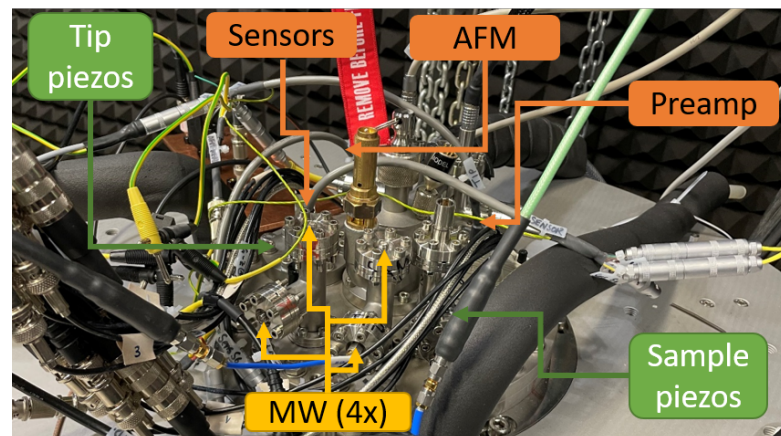
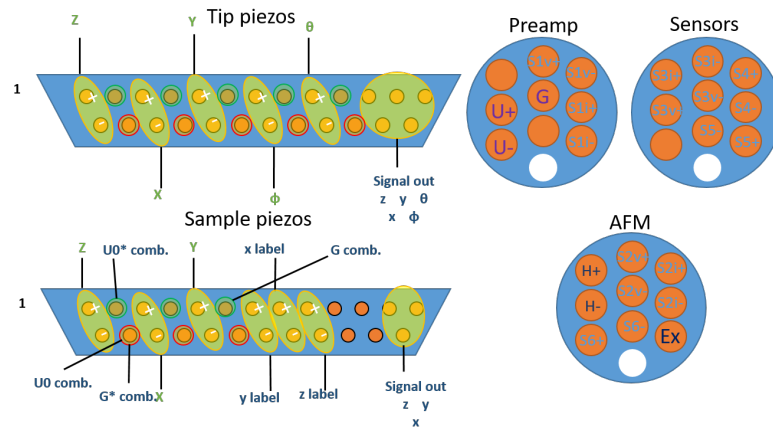


Fig. 3.6: **a** Thermalization stage just below top flange, showing the baffles and thermalization mounts. Two more thermalization stages are located below the bottom plate. **b** The non-coaxial wires are thermalized at the cryostat baffles using a custom wire thermalization mount. The thermalization mount is screwed into the baffle. **c** The coaxial cables are thermalized at the cryostat baffles using a custom built cable thermalization mount. The thermalization mount is epoxied to the cable and screwed into the baffle.



a Top plate connections



b Connector schematic

Fig. 3.7: **a** Image of the cryostat top plate connections. **b** Schematic of the cryostat top plate connections, showing the wiring for the sample and tip piezoelectric motors, the AFM with preamplifier, and the temperature sensors.

instead epoxied to a custom built Copper thermalization stage at each baffle. To this end, a thermally conducting epoxy (Epo-Tek® H77) is used to attach the cable to the thermalization stage. The thermalization stage is then screwed into the baffle, as shown in Fig. 3.6c. As with the non-coaxial wires, the last break happens at the LHe baseplate. An image of the top plate of the cryostat with the connectors is shown in Fig. 3.7a, and the corresponding schematic in Fig. 3.7b.

3.4 Ultra-high vacuum

The vacuum setup consists of a main chamber and a load-lock chamber, which can be independently pumped, with the main capable of reaching a base pressure (with the cryopump) of 10^{-10} mbar and the load-lock a pressure of 10^{-8} mbar. The two chambers are separated by a manual gate valve (VAT Series 10.8 DN63-200), allowing samples to be introduced into

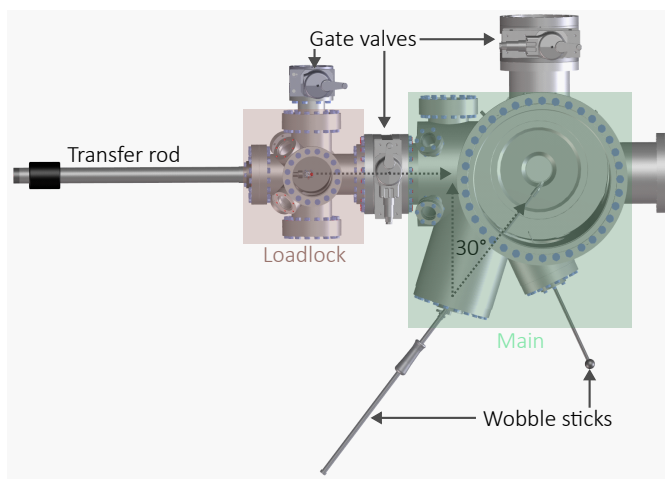


Fig. 3.8: CAD diagram showing the top view of the UHV chamber rendered in [PTC Creo](#). A list of the components used is shown in [Appendix C.4](#).

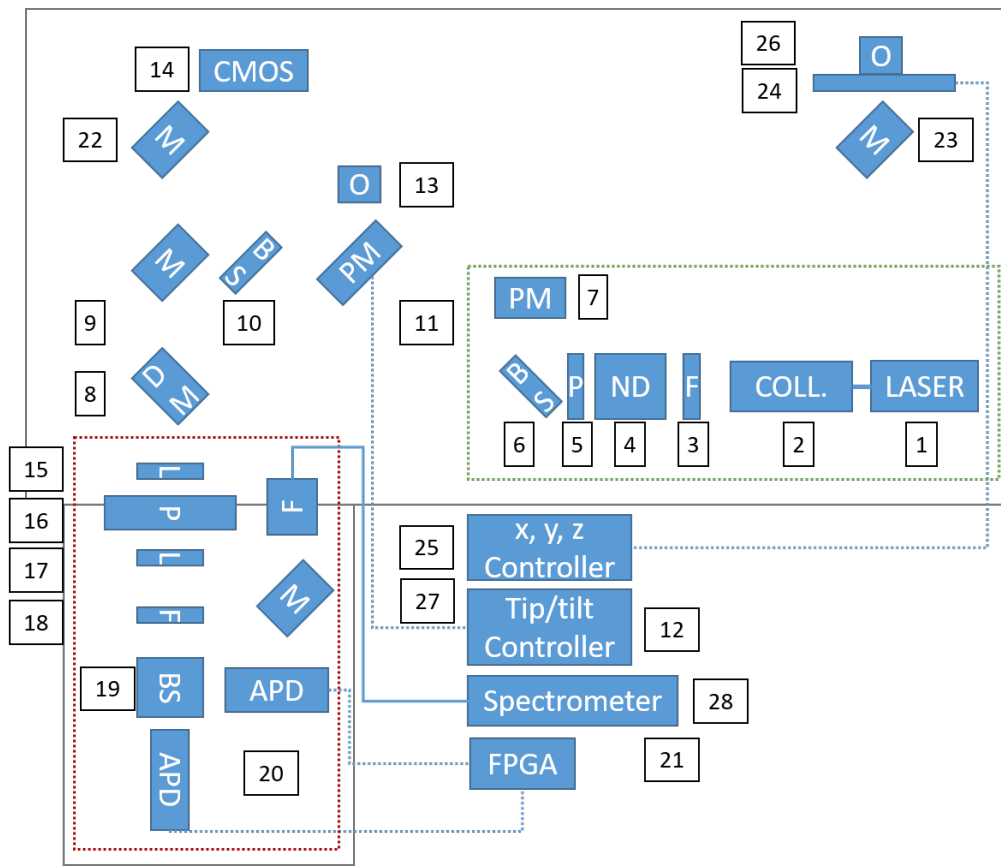
the load-lock while maintaining vacuum in the main chamber. A CAD model of the vacuum system is shown in [Fig. 3.8](#).

To evacuate the chambers, the setup is equipped with a range of different vacuum pumps – diaphragm pumps, turbomolecular pumps and ion pumps. Each pump operates in a different pressure regime. The diaphragm pump (Pfeiffer Vacuum MVP 070-3) pumps the system from ambient conditions (1180 mbar) to ≈ 1 mbar. A backing turbomolecular pump (Pfeiffer Vacuum HiPace 80) further pumps the system down to a pressure of 10^{-5} mbar. From here, two primary turbomolecular pumps (Pfeiffer Vacuum HiPace 300 H) are used to pump down to a pressure of 10^{-7} mbar. To reach ultra-high vacuum, the system is baked to 100°C for 24 h. After baking, the ion-getter pump (NEXTorr D300-5) is used to pump down to a pressure of 10^{-9} mbar. Once the system is at low-temperature and the cryopump is activated, we can reach a base pressure of 10^{-10} mbar.

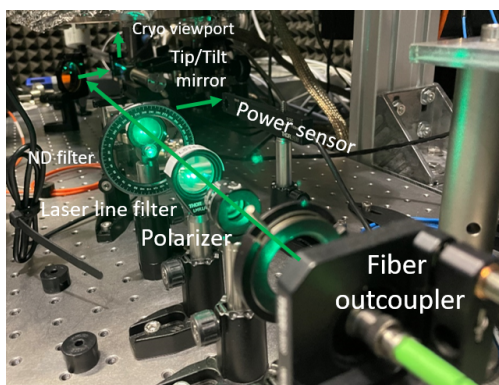
To transfer a tip/sample into the measurement head, the tip/sample is mounted on a magnetic transfer arm (VAb MDS 40-400) in the load-lock chamber at ambient conditions. The load-lock chamber is then pumped down to its base pressure. The manual gate valve between the load-lock chamber and the main chamber is opened, and the magnetic transfer arm is extended into the main chamber. From here, a wobble-stick (VAb STWS 150) is used to open the window on the radiation shields, and second wobble-stick (VAb MDWS-ZO 350) is used to move the tip/sample from the transfer arm to the measurement head. Once the tip/sample is mounted on the measurement head, the window on the radiation shields is closed, the transfer arm is retracted into the load-lock and the manual gate valve is closed.

3.5 Confocal laser scanning microscope

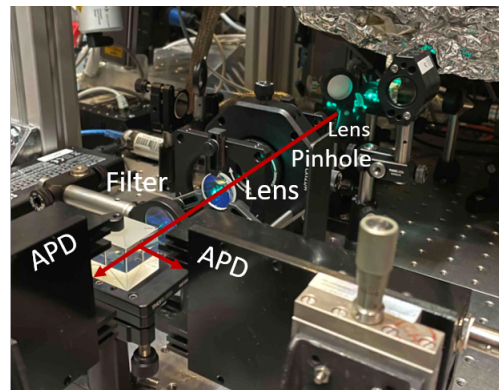
NV centers are optically initialized and read out. Confocal microscopy, in contrast to standard microscopy, allows for higher contrast and resolution. It does so by confining the focal spot to



a Optical schematic



b Excitation path



c Collection path

Fig. 3.9: a Indexed schematic of the optical layout. The green and red boxes indicate excitation path (b) and collection path (c) respectively. Black lines show the optical table. A list of all optical components along with their corresponding index is given in [Appendix C.7](#).

a volume near the optical diffraction limit. Roughly speaking, it does this by spatially filtering photons outside of the focal volume using a narrow aperture. For a laser operating in TEM₀₀ mode, the spatial distribution of intensity is given by Eq. 3.1.

$$I(x, y, z) = I_0 \exp\left(\frac{-2\left(x^2 + y^2 + \frac{z^2}{\chi^2}\right)}{w^2}\right) \quad (3.1)$$

where I_0 is the intensity at the center of the beam and w is the $1/e^2$ beam radius in the x, y plane. In the diffraction limit, χ is the ratio of the axial optical resolution in z and radial optical resolution in the x, y plane. The radial and axial resolution in the Rayleigh limit are given by,

$$r_{x,y} = \frac{0.61\lambda}{NA} \quad \text{and} \quad r_z = \frac{2\eta\lambda}{NA^2} \quad \Rightarrow \quad \chi = \frac{2.33\eta}{NA} \quad (3.2)$$

where the numerical aperture of the objective $NA = \eta \sin \theta$, λ is the wavelength of light, θ is the half angle of the focused light cone and η is the refractive index of the medium. Plugging in the values for our system ($\lambda = 515 \text{ nm}, \eta = 1, NA = 0.9$) into Eq. 3.2 we get lower limit for $\chi = 2.55$. In other words, the confocal volume is an oblate spheroid with a major axis length of $1.2 \mu\text{m}$ and minor axis length of $0.35 \mu\text{m}$. The resulting confocal volume is $0.6 \mu\text{m}^3$.

In our system, we can operate the confocal microscope in two modes – (a) by scanning the sample or (b) by scanning a mirror underneath/back of the objective. In the first case, the sample is moved along the (x, y) Cartesian axes to generate a 2D raster count rate map. In the second case, the mirror is moved along the (θ, ϕ) polar axes to generate a 2D raster count rate map. The mirror scanning mode is generally preferred as it allows for faster scanning using an ambient condition piezoelectric tip/tilt mirror. However, in this mode, the (θ, ϕ) range is limited to the back aperture of the objective lens, and off-axial aberrations are also more prevalent. Neither of these limitations is an issue for NV-SPM, as we are only dealing with a single NV center hosted in a $10 \times 6 \mu\text{m}$ diamond plate, which can be easily positioned at the geometric center of the objective lens, where such deleterious effects are avoided.

A schematic of the optical setup is shown in Fig. 3.9a. A 515 nm laser beam is generated by a diode laser (Toptica iBEAM-SMART-515-S) with an integrated angled physical contact (APC) fiber out-coupler. This fiber out-coupler is connected to a collimator (Thorlabs F110APC-532), after which the laser beam is passed through a laser line filter (Thorlabs FL514.4-10) and linear polarizer (Thorlabs LPVISA050-MP2). The intensity of the laser beam is adjusted using a continuously variable neutral density (ND) filter (Thorlabs NDC-50C-2M-A). The beam is then split with a 90:10 beam-splitter, where 10% of the beam is sent to a photo diode power sensor (Thorlabs S130C). The remaining 90% is reflected off a dichroic laser beam combiner (Newport 10Q20BB.1) and then reflected off a 45 deg mirror connected to a tip/tilt piezo platform into

the cryostat.

The laser beam passes through three fused silica viewports inside the cryostat, after which it is focused on the NV with a fixed semi-apochromat objective lens (Olympus MPLFLN100x). The light emitted from the NV is collected by the objective lens and passed through a dichroic laser beam combiner to the collection path. The collection path consists of a lens (Newport KPX076AR.14) – pinhole (Thorlabs P75D) – lens (Newport KPX082AR.14) combination. Any stray laser light is filtered by either a 650 nm or a 550 nm long-pass filter (Thorlabs FELH0650 or Thorlabs FELH0550) and split with a 50:50 beam-splitter cube (Thorlabs BS013), and each of the split paths contains a photon counting module (Excelitas SPCM-AQRH-WX). The photon counting modules generate a TTL pulse which is sent to a time-to-digital converter (Swabian Instruments Timetagger 20) which records the counts in memory where they can be read out using appropriate measurement software.

Camera We further added a 45:55 (R:T) pellicle beam-splitter (Thorlabs BP145B1) on a motorized flip mount (Thorlabs MFF101/M). The beam-splitter can be flipped into the optical path, collecting light and sending it to a camera. The light is focused onto a color CMOS sensor (Thorlabs CS165CU) using a plano-convex lens. The camera provides a live video of the tip/sample. This is useful for performing a rough optical alignment of the tip, and for adjusting the relative position of the tip and sample.

Spectrometer To measure optical spectra in the visible/NIR range (350 nm to 925 nm), a spectrometer can be added into the collection path. This is done by rotating a 45:55 beam splitter (Thorlabs BP545B1) into the collection path after the lens-pinhole-lens combination. The light is focused into a fiber in-coupled spectrometer (OceanInsight QE Pro) using a plano-convex lens.

3.6 Pulsed microwave

To control the spin state of the NV center, perpendicular oscillating microwave fields need to be applied (recall Eq. 1.3). For the maximum magnetic field strength (≈ 1 T), the effective Zeeman shift of the NV center ($\gamma_e = 28 \text{ GHz T}^{-1}$) is ≈ 28 GHz. This necessitates broadband pulsed microwave generation.

The pulse generation is sequenced and synchronized by an arbitrary waveform generator (AWG). The AWG (Spectrum DN2.663-04) has 4 analog channels and 8 digital (TTL) channels. The analog channels have a bandwidth of 400 MHz. The local oscillator (LO) (Rohde & Schwarz SMF100A) is capable of broadband frequency generation from 2 GHz to 20 GHz. The pulse sequence to be implemented is uploaded to AWG, and this is described further in § 3.8. The AWG and LO can be used in two configurations – *standard configuration* and *IQ configuration*,

Standard configuration In the standard configuration, only the digital channels of the AWG are used. The digital output of the AWG is dc shifted by a 5 V bias-T (Mini-Circuits ZFBT-6GW+) and sent to a solid-state switch (American Microwave SW-2184-1). This TTL line triggers the

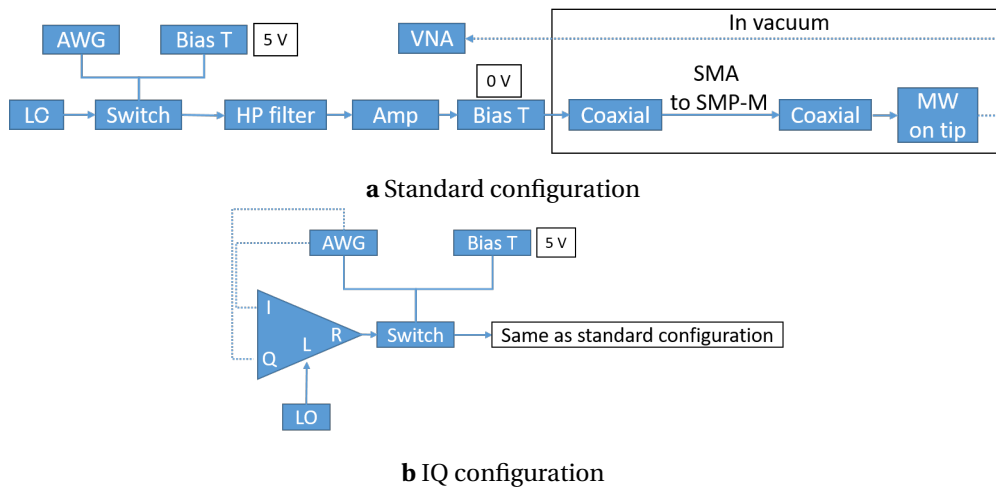


Fig. 3.10: **a** Schematic diagram of the pulsed microwave setup in a standard configuration. The standard configuration is suitable for measurements not involving phase shifted pulses. **b** Schematic diagram of the pulsed microwave setup in a IQ configuration. The IQ configuration uses the analog channels of the AWG (shown with a dotted line), as inputs to an IQ mixer along with the LO. The analog inputs of the AWG can be phase shifted relative to one another. A list of the components used is shown in [Appendix C.8](#).

switch into its ON/OFF configuration, with a ≈ 30 ns rise and fall time. The output of the switch is high-pass filtered (Mini-Circuits SHP-1000+) to remove any low frequency ringing, then sent to a broadband power amplifier (Spanawave GT-1000B). The output of the broadband amplifier is connected to a 0V bias-T (Pulsar BT-29-400S) to prevent any reflections from entering and damaging the sensitive amplification components. The output is fed into the vacuum chamber through SMA CF16 feed-through flanges. Inside the vacuum chamber, cryogenic cables (Teledyne StormFlex® 047) are used to transfer the MW to the measurement head. A schematic of this configuration is shown in [Fig. 3.10a](#).

IQ configuration In the IQ configuration, both the digital and analog channels of the AWG are used. The analog channels are used to generate the in-phase (I) and quadrature (Q) components of the microwave signal, which are fed into an IQ mixer along with the LO signal. The IQ mixer effectively extends the limited bandwidth of the AWG analog output (400 MHz) to the full frequency range of the LO (2 GHz to 20 GHz). This configuration is particularly useful for pulse schemes involving a phase shift between the microwave pulses, such as the XY8 or Hartman-Hahn pulse scheme. A schematic of this configuration is shown in [Fig. 3.10b](#).

Microwave on tip

The final stage of the microwave transmission is the tip. The tip holder contains two SMP-M connectors as described in [§ 3.2.2](#). The SMP-M connectors on the tip holder are connected by short coaxial cables (Amphenol RF 095-725-111-030) to PCB MW connectors (Rosenberger 18S101-40ML5) epoxied to tip holder plate. A $20\ \mu\text{m}$ thick gold wire is soldered between the

PCB connectors, and the distance between the wire and the NV tip is kept around $\approx 300 \mu\text{m}$. This gap is on the larger side, but is required to minimize the chances of damaging the tip during the wire bonding process. This will, however, lead to a modification in the microwave coupling strength ($\propto 1/r^3$). This modification can easily be compensated by adjusting the MW power at the output of the local oscillator to achieve $\approx 100 \text{ ns}$ π -pulse lengths. The microwave can be terminated at the tip with a 50Ω SMP-M termination, or can be fed back out through the second SMP-M connector for real-time monitoring with a vector network analyzer (VNA) (Rohde & Schwarz ZVL6). A CAD diagram of the microwave on tip is shown in Fig. 3.11.

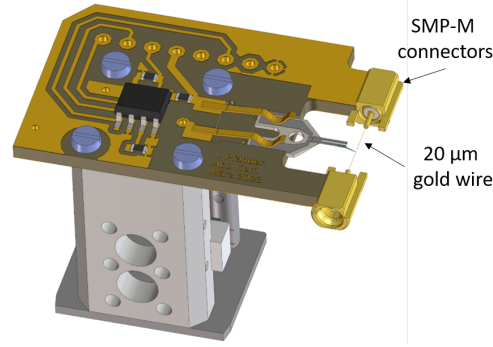


Fig. 3.11: CAD diagram of the microwave on tip rendered in PTC Creo.

3.7 Dry vector magnet

To apply magnetic fields aligned with the axis of the NV center and modify the Zeeman shift, a vector magnet is required. In our system, we use a Helmholtz pair design for each of the (x, y, z) axis. A Helmholtz pair consists of two coils separated by a certain distance and having equal radius. The magnetic field along the axis of the coil is given in Eq. 3.3, where I is the current in the wire, and γ is ratio x/R , where x is the axial distance from the center of the coil and R is the radius of the coil. μ_0 is the permeability of free space.

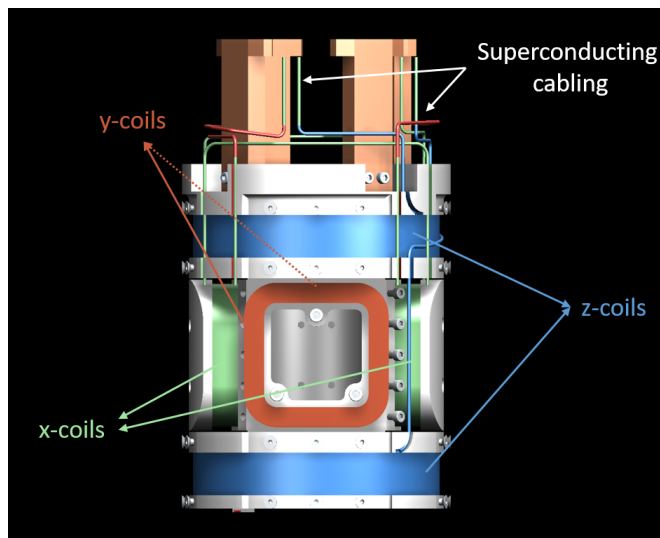
$$B(\gamma; I, R) = \frac{\mu_0 I}{2R} \left[\frac{1}{(\gamma^2 + \gamma + \frac{5}{4})^{\frac{3}{2}}} + \frac{1}{(\gamma^2 - \gamma + \frac{5}{4})^{\frac{3}{2}}} \right] \quad (3.3)$$

In the limit $\gamma \rightarrow 0$, i. e. near the geometric center of the Helmholtz pair,

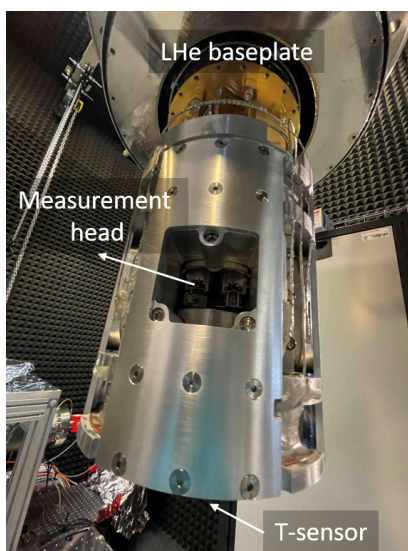
$$B(I, R) = \frac{\mu_0 I}{R \left(\frac{5}{4}\right)^{\frac{3}{2}}} \quad (3.4)$$

And the magnetic field is uniform at the center of the coils, i. e. $\partial^2 B / \partial x^2 = 0$.

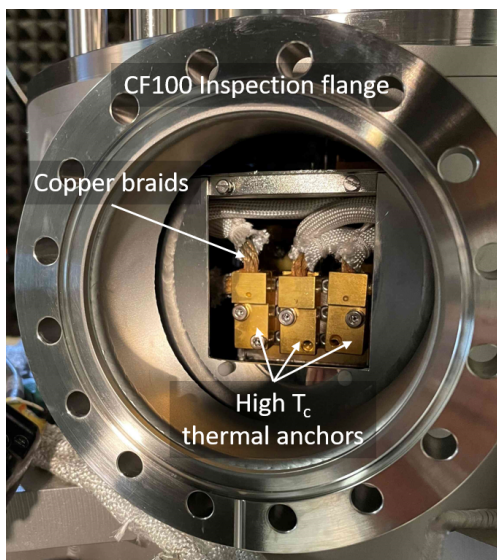
As shown in Fig. 3.12a, the Helmholtz pairs are wound with a low- T_c superconductor to



a CAD render



b Magnet picture



c High-T_c thermal anchors

Fig. 3.12: a CAD diagram of the magnet rendered in PTC Creo. b Picture of the magnet thermally coupled to the liquid Helium baseplate. Sample transfer is performed through the opening in the y-coil. c Liquid nitrogen thermal anchors for the high-T_c wires, viewed through the inspection flange near the top of the cryostat. A list of all the components used in the vector magnet is given in Appendix C.6.

maximize the effective magnetic field. Unlike most standard implementations, the magnets are *not* immersed in liquid Helium, due to three design constraints in the our system – (i) the NV needs a very homogeneous external magnetic field which requires the sample and tip located inside the magnet coils, (ii) we need to perform an *in-situ* exchange of tip/sample, and (iii) we need optical access into the system for excitation and readout of the NV center. In a UHV environment, this is highly challenging, as even a minor thermal short could trigger a full quenching of the superconducting coils. To minimize the possibility of a quench, the coils are strongly coupled to the liquid Helium baseplate with Copper plates, and the wires connected to the magnet are made from a high- T_c superconductor (Fig. 3.12b). The wires are thermally anchored to the liquid Nitrogen shield near the cryostat baffles to cool them below their superconducting temperature. When extracting the liquid Helium cryostat care must be taken to disconnect the thermal anchors via the inspection flanges (Fig. 3.12c).

The temperature of the magnet is carefully monitored during measurement by a sensor placed at the bottom of the z -coil (Cernox® CX-1070-SD). Additionally, three separate sensors (Lakeshore PT-102) are used to monitor the temperature at the top end of the high- T_c wires.

3.8 Measurement control with Qudi-Hira

Modern experimental systems require multiple hardware devices working together in synchronicity with real-time processing of measurement data. Additionally, this information needs to be saved in formats suitable for *ex post facto* analysis. To meet the demands of an NV-SPM operating at LT-UHV, we built Qudi-Hira.

Qudi-Hira is set of libraries built on top of the excellent open-source Qudi framework⁷². It is primarily written in Python, a high-level, general-purpose and dynamic programming language that has heavily gained popularity in the scientific community in recent years^{73,74}. The Qudi core handles module loading, module dependency resolution and module cross-connections, along with thread management and remote access.

An experiment module in Qudi consists of three parts – *hardware*, *logic* and *GUI*. The *hardware* module is responsible for low-level communication with hardware devices. The *logic* handles experimental control loops and data processing. The *GUI* is a graphical user interface that allows the user to interact with the experiment. Communication between the three parts is abstracted using interfaces (`abc.abstractbaseclass`) and is handled by the Qudi core.

Several modules, purpose built for NV-SPM at LT-UHV, have been developed in Qudi-Hira,

- Pfeiffer gauge pressure monitoring
- Lakeshore gauge temperature monitoring
- Twickenham liquid helium depth indicator monitoring
- Toptica iBEAM laser control
- Thorlabs PM100D power meter monitoring
- Spectrum AWG pulse generation and synchronization
- Nanonis raster scan control

The modules all support *conditional cross-interactions* and *parallel execution*. *Conditional cross-interactions* allow an interaction in one module to trigger an operation in another. For example, the Lakeshore temperature and Pfeiffer pressure monitoring modules can trigger a pulse sequence in the pulse generation module when a certain temperature and pressure is reached. The pulse generation module can then trigger a measurement in the raster scan control module. *Parallel execution* allows multiple modules to execute in parallel. For example, during the conditional sequence given above, the laser power and photon timetrace could be continuously monitored. This allows for a modular, flexible and extensible framework for building complex experimental schemes.

Out of these modules, the pulse generation and synchronization module, along with the raster scan control module are the most complex. Both of them are described in the following sections.

3.8.1 Pulse generation and synchronization

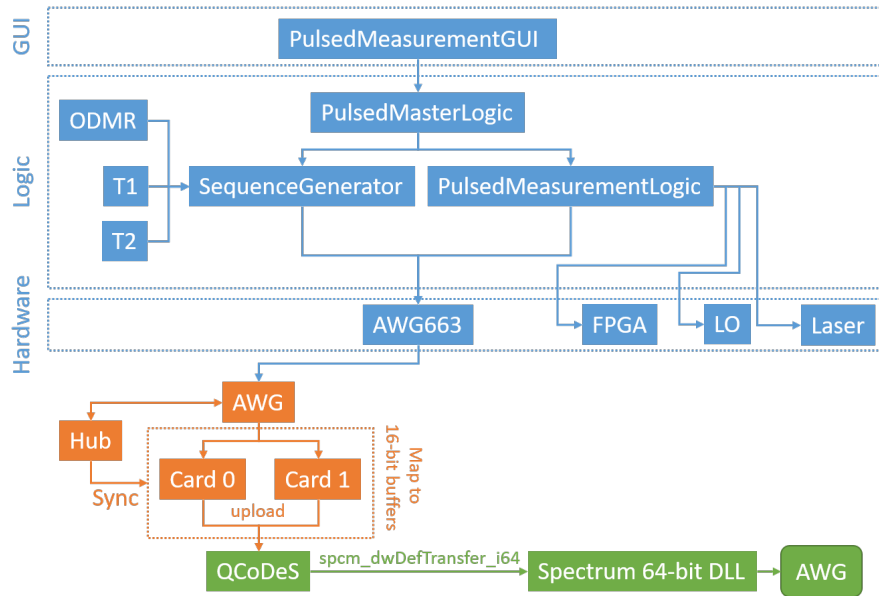


Fig. 3.13: Schematic layout of the pulse generation and synchronization. Modules in blue and orange are a part of Qudi-Hira, and modules in green are externally loaded.

As was described in § 1.4, ODMR pulse sequencing is core to the functionality of an NV-SPM. To this end, we developed a pulse generation and synchronization module for Qudi-Hira. The module is based on the Spectrum DN2.663-04 AWG, which is capable of simultaneously generating arbitrary waveforms across multiple channels at high sample rates (1.25 GSs^{-1}). Low level driver control is handled by loading the dynamic linked library (DLL) provided by Spectrum. The direct communication with the DLL is handled by QCoDeS community contributed drivers⁷⁵.

The QCoDeS drivers sit at the lowest level in the class hierarchy, and handle the responsibility of loading the Spectrum DLL. The AWG supports multiple cards, each of which is represented

by a Card class. Each Card class executes a buffered write method `spcm_dwDefTransfer_i64` to upload a 16-bit data sequence. The cards are kept indexed and synchronized by a Hub class. The Hub class can support an arbitrary number of cardsⁱ. The Hub and Card classes are instantiated in the AWG class. The AWG class is less abstract and was purpose-built to support only two cards (as is the case for our AWG hardware). Its primary function is to set all cards into a known initial state, and then perform a multi-threaded upload of the pulse sequence to all cards. The final hardware class layer is the AWG663 class which is responsible for exposing the hardware control methods to Qudi-Hira.

Within Qudi-Hira, pulses are created graphically using the `PulsedMeasurementGUI` module. Pulse sequencing often involves other hardware devices, such as the field programmable gate array (FPGA), laser and LO. This is handled by the `PulsedMeasurementLogic` module, which also interfaces with the AWG class.

These abstractions are *extremely powerful*, as they permit the creation of highly sophisticated custom pulse sequences without having to write a single line of codeⁱⁱ.

3.8.2 Raster scan control

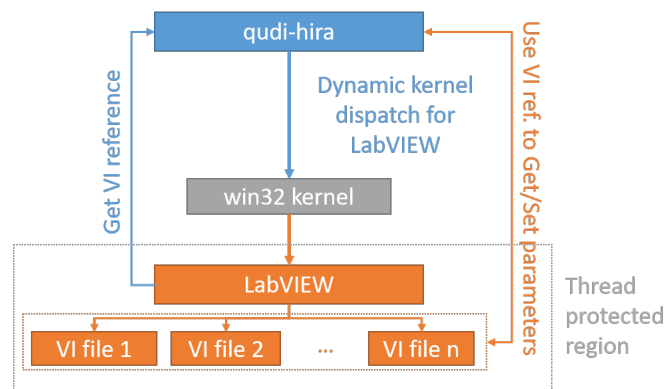


Fig. 3.14: Interface between LabVIEW™ and Qudi-Hira. The LabVIEW™ program is used to control the interface to the Nanonis™, and the Qudi-Hira is used to control the pulse generation and synchronization.

In the previous section, we detailed the process behind pulse generation and synchronization. However, for NV-SPM, we need an additional layer of abstraction. This is because an NV-SPM measurement is performed in a raster scanning pattern, where each pixel on the scan represents the result of a full measurement sequence. We use the Nanonis™ PLL controller to control the raster scanning pattern. This necessitates a connection between the Nanonis™ and Qudi-Hira.

There are a few different ways to achieve this. The simplest is to use a pixel TTL trigger generated by the Nanonis™ when it moves to a new point in the pattern. The trigger is sent

ⁱNote that the Spectrum AWG itself can support a maximum of 8 cards

ⁱⁱThis simplicity is only possible due to the advanced structure of the pulse generation (Fig. 3.13), which is around 7,000 lines of code

to the FPGA, which uses it as a signal to move to a different memory index. This scheme is particularly useful for generating 2-dimensional NV timetraces. A 1-dimensional calibrated timetrace has already been used to map Meissner screening in superconducting LSCO thin films⁷⁶. However, as this scheme only triggers the counting FPGA, it is limited to measurements that do not require a pulse sequence. For example, it cannot be used to perform ODMR measurements.

To perform more advanced measurement, a more generic interface is required. This is achieved by interacting with the Nanonis™ through a LabView™ VI. Methods contained in the LabView VI are called from Qudi-Hira. Since Qudi-Hira is multi-threaded, we need to initiate a thread locked dynamic dispatch to the LabView VI. This is done using the `comtypes` package, using the `comtypes.CoInitialize()` method to open an instance of LabView and then load the necessary VI files. A schematic of the interface between the two programs is shown in Fig. 3.14.

3.9 Ambient stage

As was described in § 3.4, the process of transferring a diamond tip into the cryo chamber is complex. Transfers should therefore be minimized, and tip properties should be tested before transfer. To this end, we have built an ambient stage for rapid testing of a diamond tip's optical, AFM resonance and microwave characteristics. The stage is shown in Fig. 3.15.

The ambient stage consists of an (x, y, z) piezoelectric translation stage (Physik Instrumente P-733.3), along with a custom built tip stage, which is a replica of its UHV counterpart. It features all the contacts for microwave and AFM. For optical access, the excitation path and collection paths remain the same as for the UHV stage, with the only difference being that dielectric mirror 9 (see Fig. 3.9a) is flipped down. This causes the laser to reflect off two secondary mirrors into the ambient objective (attocube LT-APO/VISIR/0.82). The position of the ambient objective can be precisely adjusted with a manual (x, y, z) translation mount (Thorlabs CXYZ1/M) to center the laser path relative to the diamond tip.

3.10 Active and Passive damping stages

Achieving nanoscale resolution in NV-SPM experiments requires damping the vibrations of the tip/sample. Mechanical vibrations are typically in the low frequency range, and are primarily comprised of building vibrations on the sixth floor (1 Hz to 20 Hz), and vibrations from turbomolecular pumps (10 Hz to 300 Hz). The frame of the setup is very stiff, which effectively decouples a majority of the lower frequency vibrations to the system. To further supplement this, we use a combination of active piezoelectric dampers (TMC Stacis 2100), primarily effective in the 0.6 Hz to 100 Hz range, and passive pneumatic dampers (Newport I-500), which are effective in the 10 Hz to 300 Hz range. The active dampers are located at the base of the machine, and the passive dampers are located between the UHV chamber and the cryostat top plate. Since the ambient stage (see Fig. 3.15) is mounted directly on the optical table, it can only utilize the active dampers, whereas the UHV stage can utilize both active and passive dampers (see Fig. 3.17).

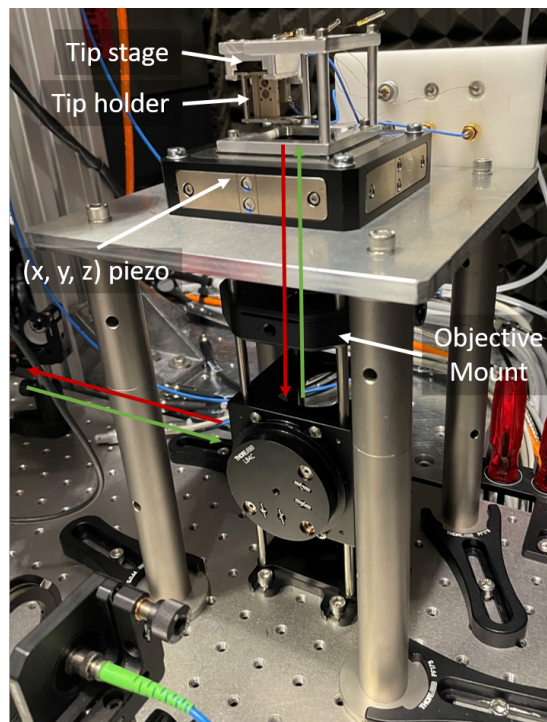


Fig. 3.15: Ambient stage for rapid testing of diamond tips. Optical properties, AFM resonance and microwave characteristics can be tested in this stage.

3.11 Final system

We have now described the construction of an NV-SPM capable of operating at ultra-high vacuum and low-temperature. A schematic overview of the system is given in Fig. 3.16. An image of the full system is shown in Fig. 3.17.

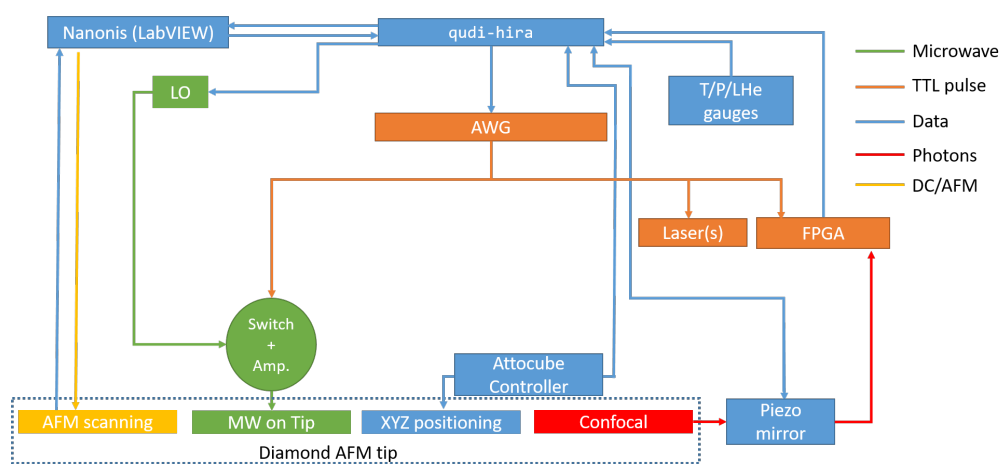


Fig. 3.16: High level experimental schematic. Acronyms – local oscillator (LO), arbitrary wave-form generator (AWG), field programmable gate array (FPGA), temperature/pressure/liquid helium (T/P/LHe).

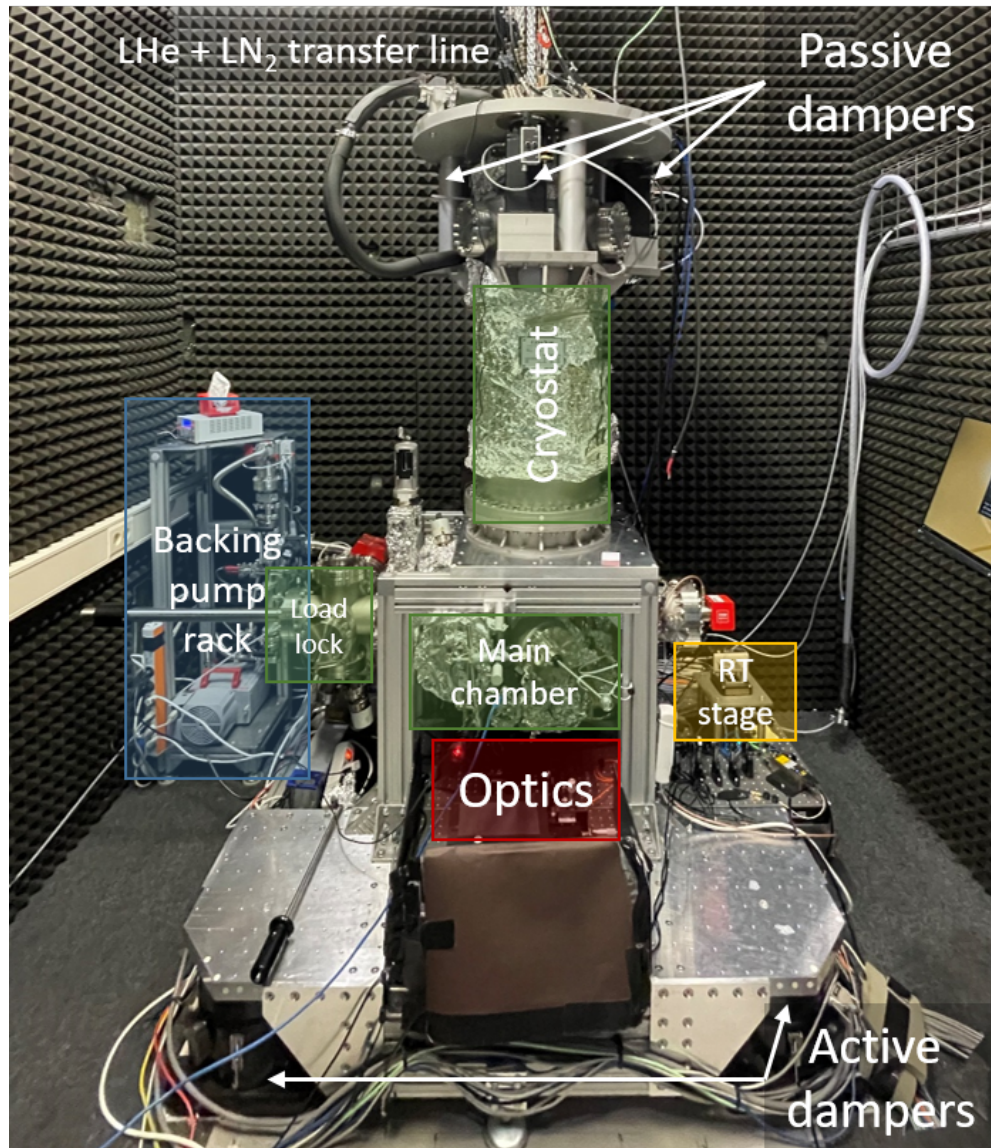


Fig. 3.17: Image of the final system.

4 Performance of the NV-SPM

The Universe is under no obligation to make sense to you.

Neil deGrasse Tyson

Before the system can be used to probe novel samples, we must benchmark the performance of the NV-SPM. The performance of the system is measured along several axes, each of which is described in the following sections. In § 4.1 we test the vacuum capabilities and low temperature performance of the system. § 4.2 describes the calibration of the vector magnet, along with its quench training to achieve its maximum magnetic field. In § 4.3, we test the NV count stability and the performance of the imaging platform, along with co-locating the position of the NV tip and sample. § 4.4 describes the process of optimizing the pulse shape and transmission function in the pulsed microwave system. In § 4.5, we combine both the confocal and pulsed MW to perform optically detected magnetic resonance measurements on a single NV center. Finally, we benchmark the performance of the AFM with a NV tip in § 4.6.

4.1 Ultra high vacuum and low temperature

To test the vacuum performance of the system, the double stage turbopumps backed by a membrane pump were used to evacuate the system to 10^{-6} mbar. At this pressure the system was baked up to 100°C (380 K) over a period of 12 d to remove any residual water and other contaminants. We limit the bake out temperature to 100°C due to the presence of the superconducting magnet in our system. The temperature and corresponding pressure variations are shown in Fig. 4.1a. Post-bakeout the system was allowed to cool down to 300 K over a period of 8 d.

After the system was thermalized at 300 K, the base pressure was measured to be 10^{-8} mbar. We then began the process of cooling the system down to 4.2 K. This is done in two steps, first the system is cooled to 77 K by filling the LN_2 bath with liquid Nitrogen, and held at this temperature for ≈ 2 d to allow the system to thermalize. After thermalization, the LHe bath is filled with liquid Helium-4. The process of this cool down is shown in Fig. 4.1b. In total the

first-time cool down (starting from room temperature to the base temperature) took around 6 d. This can be sped up by increasing the rate of refilling the cryogenic baths, but to avoid any damage to the system due to thermal contraction and to use the maximum cooling power from the cryogenics, the cool down was done at a slow rate. Note that during cool down the tip/sample piezoelectric motors *must* be grounded and un-docked, as the piezoelectric stack needs to freely move if it comes under tension due to thermal contraction.

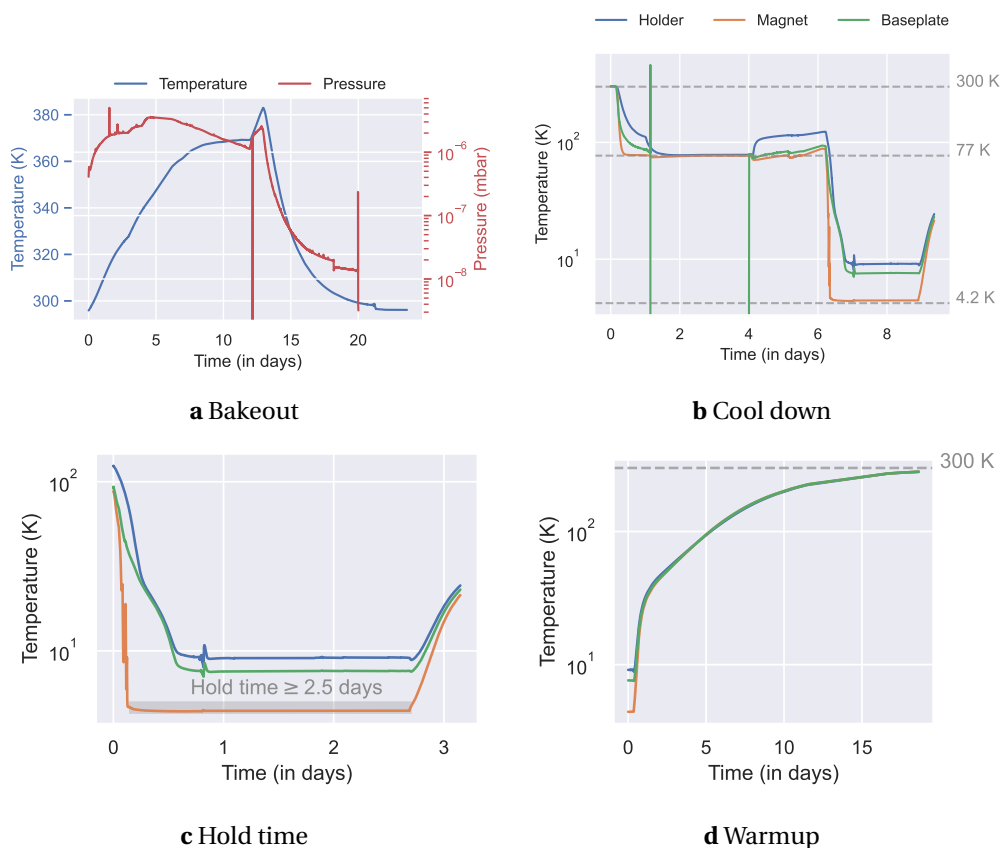


Fig. 4.1: **a** Temperature and pressure behavior during the bakeout process. The system was baked up to 100°C over a 12 d period to remove any residual water and other contaminants. Temperature of the system measured at three different locations on the cryostat – the LHe baseplate (green), the tip holder (blue) and the magnet base (orange). **b** Cool down of the system from 300 K to 4.2 K. The anomalous reading of the baseplate sensor near 77 K was due to a sensor malfunction. **c** Hold time of the system at low temperature, which is at minimum 2.5 days due to the incomplete thermalization of the system, as seen from the baseplate and holder sensors. **d** Un-assisted warmup of the system from 4.2 K to 300 K.

During the cool down of the system from 300 K to 4.2 K (Fig. 4.1b), the system temperature was monitored at three distinct locations – (i) at the tip holder (blue), (ii) at the magnet base (orange), and (iii) near the LHe bath baseplate (green)ⁱ. We observe that the temperature at

ⁱFun fact, there are around 600k data points in this image, as the temperature was probed every 10 s for several weeks.

each of these locations is not the same. The tip holder is consistently at a higher temperature than the magnet base and the LHe baseplate. The reason for this is that the tip holder is located at the end of a long piezoelectric stack and is therefore the last element to cool down. The magnet base is strongly thermally coupled to the LHe bath and registers the lowest reading accordingly. The magnet base thermalizes to ≈ 5 K, tip holder to ≈ 8 K, and the LHe baseplate to ≈ 7 K.

After the system is cooled down, we can measure its minimum hold time. The hold time represents a minimum as ideally the system would be held at LHe temperatures for a longer period of time (say a few weeks) to ensure complete thermalization. The hold time behavior is shown in Fig. 4.1c. We observe a minimum hold time of 2.5 d. This is on the low side, which is something we had predicted in § 3.3 given the large surface area of the radiation shields and corresponding increase in thermal radiation absorbed by the system. Another factor is the incomplete thermalization of the system, and we see that for ≈ 0.5 d the LHe baseplate and tip holder were still in the process of thermalizing. Once fully thermalized, we expect the system hold time to be around 3 d, which is slightly less than ideal but sufficient for our experiments. We then began an unassisted warmup of the system, which took around 20 d to completeⁱ.

4.2 Dry vector magnet

From the last section we observe a magnet base thermalization temperature of 5 K, this is excellent as the dry magnet consists of low- T_c superconducting coils that need to be held under 17 K to avoid unnecessary quenches. The magnet was manufactured by CryoVac GmbH, and the initial testing and calibration was also performed there. The result of these initial tests on the magnet z-coil is shown in Fig. 4.2a and Fig. 4.2b. The testing process involves increasing the current to the cold superconducting coils until a quench is observed. The quench current is then recorded and the process is repeated until the maximum quench current is reached.

A quench is a sudden transition of the superconducting coil from its superconducting state to its resistive state. It occurs when the field inside the magnet is too large, or the rate of change of the field is too fast (leading to eddy currents in the coil). During a quench, a spot on the superconducting coil enters into its resistive state, which causes rapid Joule heating of that spot. This heating raises the temperature of the surrounding regions, causing them to transition into the resistive state as well. This process continues until the entire coil is in the resistive state, at which point the magnet is no longer superconducting. The process can take a few seconds to complete and is accompanied by a rapid boil-off in the LHe bath. The general understanding is that quenches “train” the magnet and involve a material memory effect. The process of training a magnet involves a repeated process of steadily increasing the current until a quench is observed. After sufficient cycles, the magnet will be able to withstand a higher current without quenching.

In the first run, a total of 25 quenches were observed with the maximum quench current being 20 A. During the second run, only 3 quenches were observed and 20 A was successfully reached

ⁱThe warmup was performed over the Christmas break to minimize its time impact.

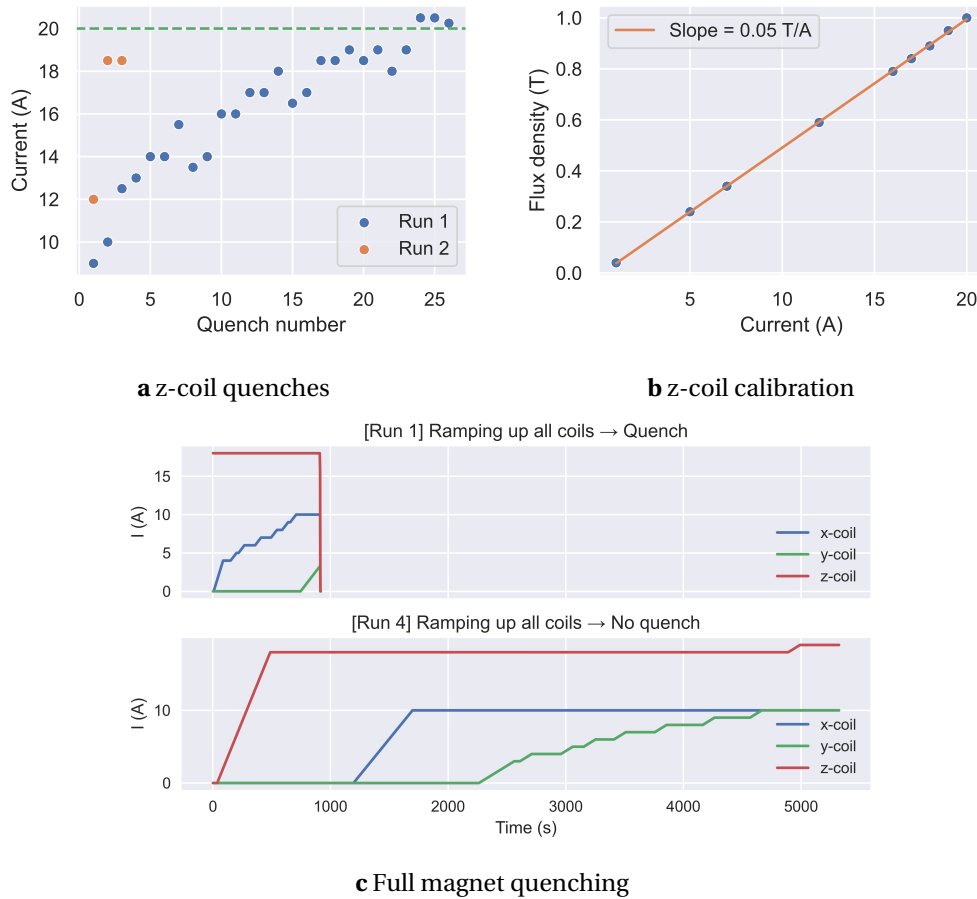


Fig. 4.2: **a** Current ramping the magnet z-coil performed at CryoVac GmbH. A total of 26 quenches were observed, with the quench current increasing steadily to a maximum of 20 A, which is the theoretical maximum operating value of the coil. **b** Calibration of the magnet z-coil performed at CryoVac GmbH. The flux density was measured with an independent field sensor during the current ramp. The extracted slope reveals a z-coil calibration of 50 mT/A. **c** In-house testing of the (x, y, z) coils. The maximum current applied was $I_x = 10\text{ A}$, $I_y = 10\text{ A}$, $I_z = 20\text{ A}$. The x and y coils have 1/2 the number of windings of the z-coil, giving a calibration of 25 mT/A, resulting in a maximum magnetic field is $B_x = 0.25\text{ T}$, $B_y = 0.25\text{ T}$, $B_z = 1\text{ T}$.

without quenching. The field calibration of the magnet z-coil was measured and provided by CryoVac GmbH with an independent magnetic field sensor located at the geometric center of the Helmholtz coils. The calibration curve is shown in Fig. 4.2b. The calibration curve is fit to a linear function resulting in a calibration coefficient of 50 mT/A.

This testing and calibration was performed on the magnet z-coil only by CryoVac GmbH. The final testing of the full magnet (x, y and z coils) was performed after integration into the NV-SPM. This is shown in Fig. 4.2c. Since the z-coil was already “trained” in prior runs, it did not quench in our testing. However, the x- and y-coils were untested, and took 4 runs to “train”. This is a significantly smaller than the 28 runs required for the z-coil, which is due to the fact that the x- and y-coils are much smaller (1/2 the number of windings) and have a lower maximum current (10 A vs 20 A). The corresponding calibration coefficient of the x and y coils is 25 mT/A.

The maximum quench current of the x- and y-coils was 10 A, and the maximum quench current of the z-coil was 20 A. Combining this with the corresponding calibration coefficients, we can calculate the maximum field of the magnet as $B_x = 0.25 \text{ T}$, $B_y = 0.25 \text{ T}$, $B_z = 1 \text{ T}$.

4.3 Confocal microscopy

For our system, optical imaging is performed with a confocal microscope. The confocal microscope permits the collection of light from the in-focus plane, while spatially filtering all out-of-focus light. The measured dark count rate of our confocal setup is ≈ 400 cps which is very close to the theoretical minimum value for two APDs (150 cps per APD). Essential to its operation is the objective lens, which defines the working distance at which the tip is placed and the light collection efficiency.

Vacuum compatible objectives like the apochromatic attocube VISIR 0.82 have demonstrated good operating performance when used with NV membrane samples (Fig. 4.3a). However, in our testing, they did not perform well with the diamond tips. While it was possible to get a confocal image of the diamond tip (Fig. 4.3b), it was extremely difficult to get the tip into focus reproducibly in a controlled manner, and given the very short working distance it required very specific alignment along the x, y, z, θ, ϕ axes. Even after alignment, we observed a significant drop-off in counts with time (Fig. 4.3c).

This drop off in counts can be attributed to two main factors – (i) the difference in construction between the diamond tip and the diamond membrane, and (ii) the limited working distance of the VISIR objective. The diamond membrane is a single crystal and in principle, can be brought arbitrarily close to the objective lens. The tip however, uses a diamond plate mounted at the end of a pulled quartz rod attached to a quartz tuning fork. The tuning fork and quartz rod add to the vertical offset of the diamond plate. This offset, which is of the order of $450 \mu\text{m}$, leads to a very fine margin within which the tip can be brought into focus. That being said, the offset is smaller than the working distance of the VISIR objective ($650 \mu\text{m}$), and *in principle* should allow the tip to sit in stable focus. However, any minor variations in the objective working distance from manufacturer specification, or even a slight rotation of the tip plate

either due to misalignment or due to unavoidable instabilities, will lead to contact of the tip body with the objective lens, leading to a significant drop-off in counts.

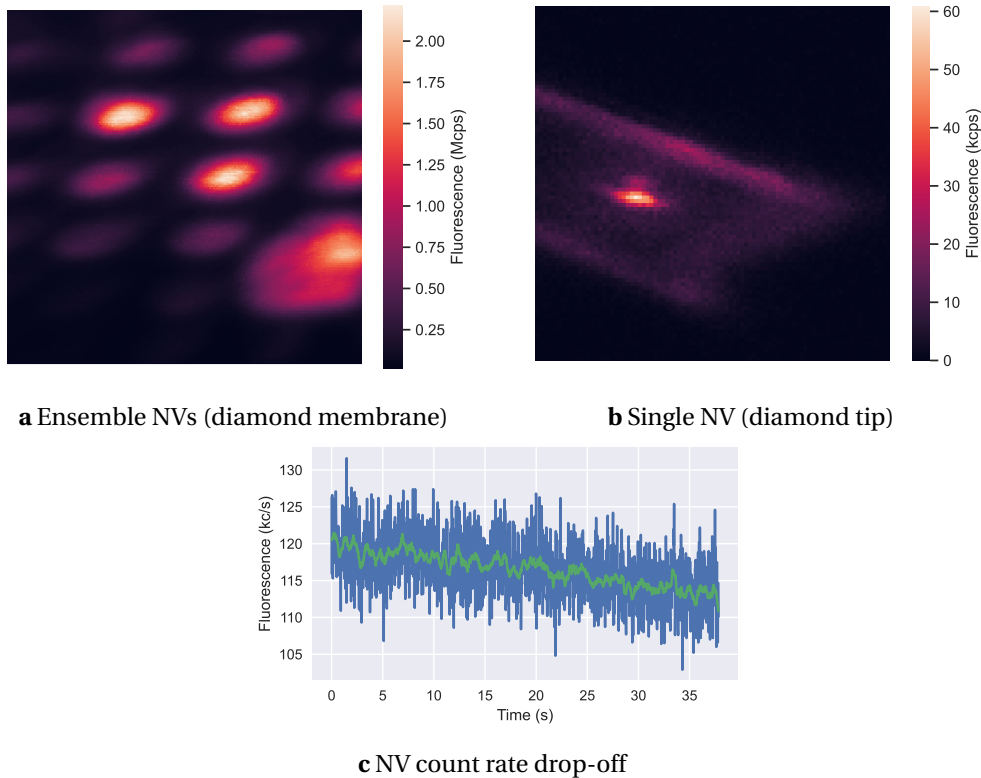


Fig. 4.3: Confocal microscopy with a VISIR objective at UHV conditions. The working distance of the objective is $650\mu\text{m}$ and the numerical aperture is 0.82. **a** Confocal image ($6\mu\text{m} \times 6\mu\text{m}$) of a diamond membrane with ensembles of NV centers in nanopillars. **b** Confocal image ($10\mu\text{m} \times 10\mu\text{m}$) of a diamond tip with a single NV center. **c** Drop-off in NV photon counts with time, likely caused by mechanical contact between the tip and the objective.

The solution to this problem is to use an objective with a larger working distance that does not sacrifice optical collection efficiency. We chose the semi-apochromatic Olympus MPLFLN100x objective, which has a 1 mm working distance and a numerical aperture of 0.9. With this objective we were able to get a stable confocal image of the diamond tip (Fig. 4.4a) with no drop-off in counts. We were therefore able to perform a saturation measurement on the diamond tip. In this measurement, the laser power is steadily increased when measuring the count rate. The counts from the NV center will show a hyperbolic behavior, increasing sharply initially until a certain point, after which they stabilize. This count behavior sits on top of a linearly increasing background count rate. The net behavior of the counts can be modeled as a hyperbolic saturation curve convolved with a linear background. The data and corresponding fit are shown in Fig. 4.4b. From the fit, we extract a saturation power of $17\mu\text{W}$ and saturation count rate of $\approx 40\text{kcps}$.

Note that unlike the VISIR, the MPLFLN is not low temperature or vacuum compatible as

per the manufacturer specifications. However, in our testing the objective functions well in UHV conditions. It is possible that after several thermal cycles, the objective performance may degrade. That said, the MPLFLN is a relatively inexpensive objective ($\approx 1/3$ the cost of the VISIR), and can be easily replaced if necessary.

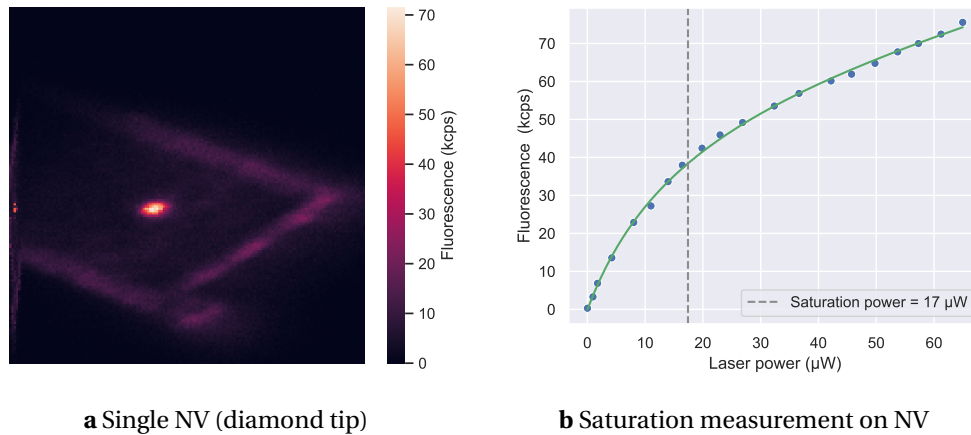


Fig. 4.4: Confocal microscopy with an MPLFLN objective. The working distance of the objective is 1 mm and the numerical aperture is 0.9. **a** Confocal image of a diamond tip with a single NV center. **b** Saturation measurement on the diamond tip. Data is a fit to a hyperbolic function convolved with a linear offset, revealing a saturation power of $17 \mu\text{W}$ and saturation count rate of ≈ 40 kcps.

4.3.1 CMOS camera for co-locating tip and sample

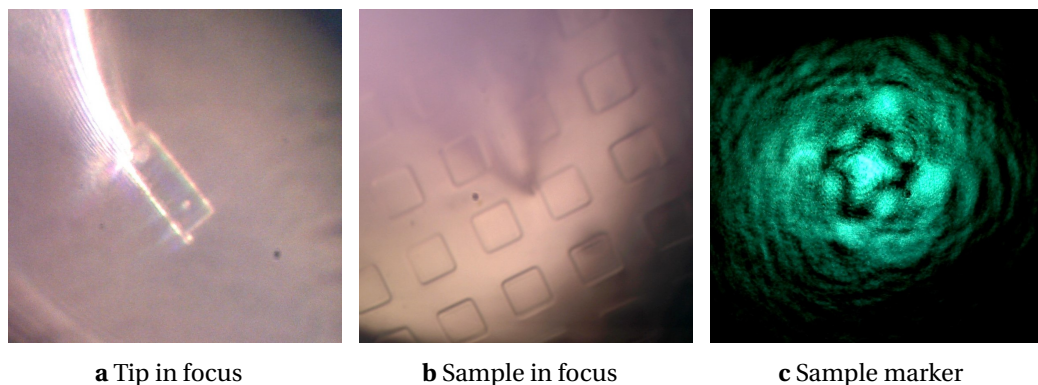


Fig. 4.5: CMOS camera image with white LED light illuminating **a** diamond tip **b** sample surface with a diamond tip. **c** Green laser illuminating a cross shaped marker on the sample surface. The CMOS camera is added into the optical path by rotating a beam splitter mounted on a motorized rotation stage. It can record real-time video at up to 30 fps and is used to co-locate the NV tip with markers on the sample surface.

In addition to the confocal microscope, we use a camera system to co-locate the NV tip with markers on the sample surface. The camera is brought into optical path by rotating a 50:50 beam splitter mounted on a motorized arm. The beam splitter sends the light to a plano-

convex lens which focuses it onto a CMOS sensor (see Fig. 3.9a for the full schematic). Such a camera system is essential for this setup, as it not only makes it easier to bring the NV tip into rough focus, but allows us to reproducibly measure specific areas of the sample. The illumination for the camera can be performed by the green laser, or by adding an additional white LED source into the path by rotating a 90:10 beam splitter. Fig. 4.5 shows images of the diamond tip and sample surface taken with the camera under different lighting conditions.

To ensure the camera image and the confocal correspond to the same area, we image the diamond tip with the confocal microscope, add the beam splitter(s) into the optical path, and then re-image with the confocal. If the two images are not the same, the optical path is adjusted, and the process is started again. We repeat this process until the two images are in perfect alignment.

4.4 Pulsed microwave control

Ground state spin transitions in NV centers are driven by MW excitations around the zero-field splitting frequency (2.87 GHz). This can be done in two ways – (i) by applying a continuous wave (CW) microwave field, or (ii) by applying a pulsed microwave field. CW excitation has several disadvantages as compared to pulsed excitation. First, CW excitation leads to additional local heating, having a deleterious impact on system stability and hold time. Second, CW excitation leads to a broadening of the ODMR lines, as it is applied alongside laser irradiation. Due to these disadvantages, we use pulsed excitation in all our experiments. In pulsed MW excitation, short pulses (≈ 100 ns) of MW radiation are applied to the NV center. There are two important parameters to be optimized when using pulsed excitation – (i) the *pulse shape*, and (ii) the *frequency transmission function*.

Pulse shape The pulse shape is the temporal profile of the MW pulse. Fig. 4.6a shows the raw pulse shape generated by a combination of the local oscillator and solid-state pulse generator. We observe a low frequency ringing artifact, both during the rise and fall of the pulse. To eliminate this ringing artifact we add in a dual high pass filter with a cut-on frequency at 1 GHz. Fig. 4.6b shows the pulse shape after the addition of the dual high pass filter.

Frequency transmission function For MW excitation, we use broadband local oscillators (1 GHz to 22 GHz) and broadband amplification (2 GHz to 20 GHz). However, components such as coaxial cables, connectors etc. show a frequency dependent transmission function. This can be probed with a vector network analyzer, the result of which is shown in Fig. 4.7a. We observe a roughly linear drop-off in power as a function of frequency (≈ 5 dBm/GHz). We can correct for this drop-off by applying a frequency dependent gain correction. The gain correction effectively inverts the transmission function, discretizes it to the frequency step of the local oscillator and stores the corresponding power in a look-up-table on the local oscillator. This has the effect of normalizing the transmitted power to the same level for all frequencies. Note that the transmission function strongly depends on tip/sample insertion force and the bonded MW wire, so it needs to be re-calibrated each time the tip/sample is

4.5 Optically detected magnetic resonance measurements

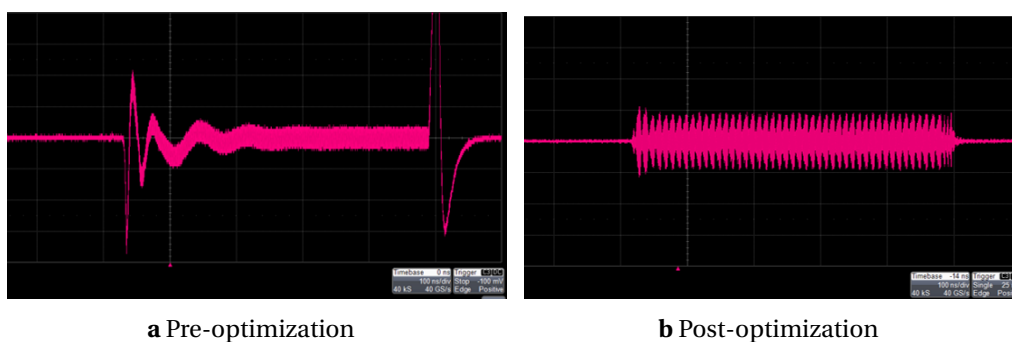


Fig. 4.6: **a** Pre-optimization, and **b** post-optimization of the MW pulse generation. The time axis is 100 ns per division, and the pulse itself is 500 ns in duration. The data is sampled at 40 GSs^{-1} on an oscilloscope.

exchanged.

During testing the power transmission we noticed that there was no signal transmission on both the tip/sample MW output line (Fig. 4.7b). After debugging, we concluded that this likely indicates a break somewhere along the MW line. To extract the location of the break, we performed a pulse reflection measurement. The pulse reflection measurement involves terminating a MW pulse of known width and amplitude to two points on the cryostat, and measuring the time difference between the two reflected pulses. The first point is chosen to be at the top plate of the cryostat (green line in Fig. 4.7c), and the second (unknown) point will be at the location of the break.

The time difference between the two reflected pulses can be used to extract the location of the break relative to the top plate of the cryostat. From the transmission of a MW signal in a coaxial cable, we can compute the speed of the signal $v = c(1/\sqrt{\epsilon_R}) \approx (2/3)c$, where ϵ_R is the relative dielectric constant of the coaxial cable conductor (copper coated with silver) and c is the speed of light in vacuum. The time difference between the two reflected pulses is measured to be $t \approx 16 \text{ ns}$. The distance between the two points can be extracted as $d = (vt)/2 \approx 1.6 \text{ m}^{\text{i}}$. This indicates the break is near the measurement head, and potentially could be caused by the cable coming under excess strain during low temperature operation, or during the bakeout process. Note that while this is undesired, it does not affect the operation of the system. We still have one MW line active on both the tip and the sample, which is sufficient for sending in pulsed MW signals. To operate in this configuration we will have to terminate the other end of the MW wire on the tip/sample with a 50Ω termination.

4.5 Optically detected magnetic resonance measurements

To test the optically detected magnetic resonance capabilities of the system we use a single NV center located inside diamond tip. The NV center is implanted with an energy of 12 keV, leading to a nominal lower bound on NV depth of 18 nm. A $20 \mu\text{m}$ thick gold wire was bonded

ⁱThe factor of 2 in the equation comes due to the pulse traveling twice through the MW line (transmission and reflection).

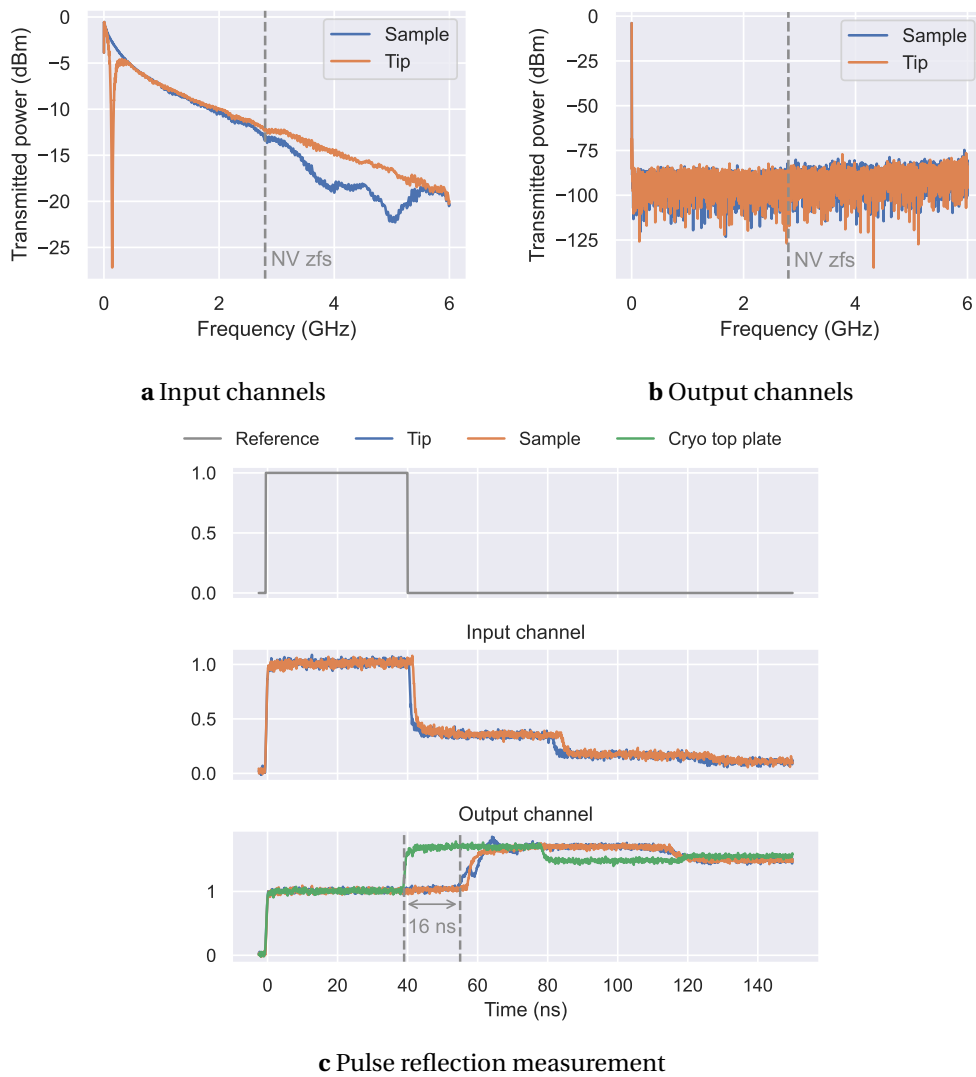


Fig. 4.7: **a** Transmission characteristics (S_{21}) of the MW input line at the tip and sample. **b** Transmission characteristics (S_{21}) of the MW output line at the tip and sample. **c** Finding the location of the microwave break in the transmission using reflection delay measurements. The reflection from the input line is as expected, the output line however shows a reflected pulse 16 ns delayed from a reflection at the top of the cryostat. The estimated break is located ≈ 1.6 m from the top of the cryostat. The features observed at higher times (80 ns and 120 ns) are higher order reflections in the MW line.

$\approx 300 \mu\text{m}$ away from the diamond plate (see Fig. 4.8a). The measurement was performed on the ambient measurement stage with no external field applied.

Fig. 4.8c shows the result of an ODMR measurement. The ODMR is measured by sweeping the microwave frequency and reading out the spin state of the NV center. When the microwave frequency matches the resonance frequency of an NV transition, the photons emitted by the NV center drop significantly due to the NV electron undergoing an ISC into the singlet states. This results in a characteristic double dip spectrum showing the $m_s = |0\rangle \rightarrow |\pm 1\rangle$ transitions of the $^3\text{A}_2$ ground state.

The ODMR spectrum is fit to a double Lorentzian model, revealing transitions at $\nu_{|0\rangle \rightarrow |-1\rangle} = 2.867 \text{ GHz}$ and $\nu_{|0\rangle \rightarrow |+1\rangle} = 2.871 \text{ GHz}$ with a contrast of $\approx 10\%$. The FWHM of the dips are 2.3 MHz and 2.6 MHz respectively. For more details of the fitting procedure, see Appendix A.

Fig. 4.8b depicts the Rabi oscillation. During this measurement the MW frequency is pinned to an NV transition, in our case the $m_s = |0\rangle \leftrightarrow |+1\rangle$ transition. The duration for which the MW pulse is applied is then varied, and the resulting spin state projection is read out. This causes the NV spin state to rotate around the x -axis of the Bloch sphere defined by the qubit basis states $m_s = |0\rangle, |+1\rangle$. However, due to decoherence channels in the system, the “length” of the spin vector will drop with time. This results in the characteristic $T_{1\rho}$ decay time, or T_1 in the *rotating* frame.

The Rabi oscillation is fit to an exponentially decaying sinusoid, revealing a Rabi frequency $\omega_R = 8.60 \text{ MHz}$ and $T_{1\rho} = (1.22 \pm 0.07) \mu\text{s}$, with a contrast of $\approx 7\%$.

Fig. 4.8d depicts the result of a Ramsey measurement, showing the Ramsey “fringes”. During this measurement, the NV is in a superposition state $|+\rangle = (|0\rangle + e^{-i\phi}|1\rangle)/\sqrt{2}$ via a $\pi/2$ pulse, followed by a free evolution for some time τ before applying another $\pi/2$ pulse to project the spin state back to the sensor basis. The phase pickup ϕ is given by $\phi = \int_0^\tau dt' \gamma B(t')$, where γ is the coupling constant and $B(t')$ is the stray magnetic field. The final state after reading out has the transition probability $p(\tau) \propto \exp(-\tau/T_2^*) [1 - \cos(\omega_0\tau)]$, where T_2^* is the Ramsey coherence time. Measuring $p(\tau)$ gives rise to oscillatory Ramsey “fringes” from which the coupling between the NV and the magnetic perturbations can be determined.

The Ramsey measurement is performed in alternating mode i. e. the second $\pi/2$ is alternated with a $3\pi/2$ pulse. This minimizes projection noise, as the NV superposition is alternatively projected onto the $m_s = |0\rangle$ and $|+1\rangle$ states. The Ramsey fringes are fit to an exponentially decaying sinusoid, revealing a Ramsey $T_2^* = (1.2 \pm 0.4) \mu\text{s}$, oscillation frequency $\omega_R = 4.36 \text{ MHz}$ and a contrast of $\approx 5\%$.

4.6 Atomic force microscopy

The AFM was tested with a variety of different tips and samples at ambient and ultra-high vacuum conditions. In our case, we use an all-electric excitation and readout for the AFM tuning fork. However, since we drive one of the electrodes attached to the tuning fork directly, we also observe a capacitive coupling between the excitation and readout lines. This crosstalk

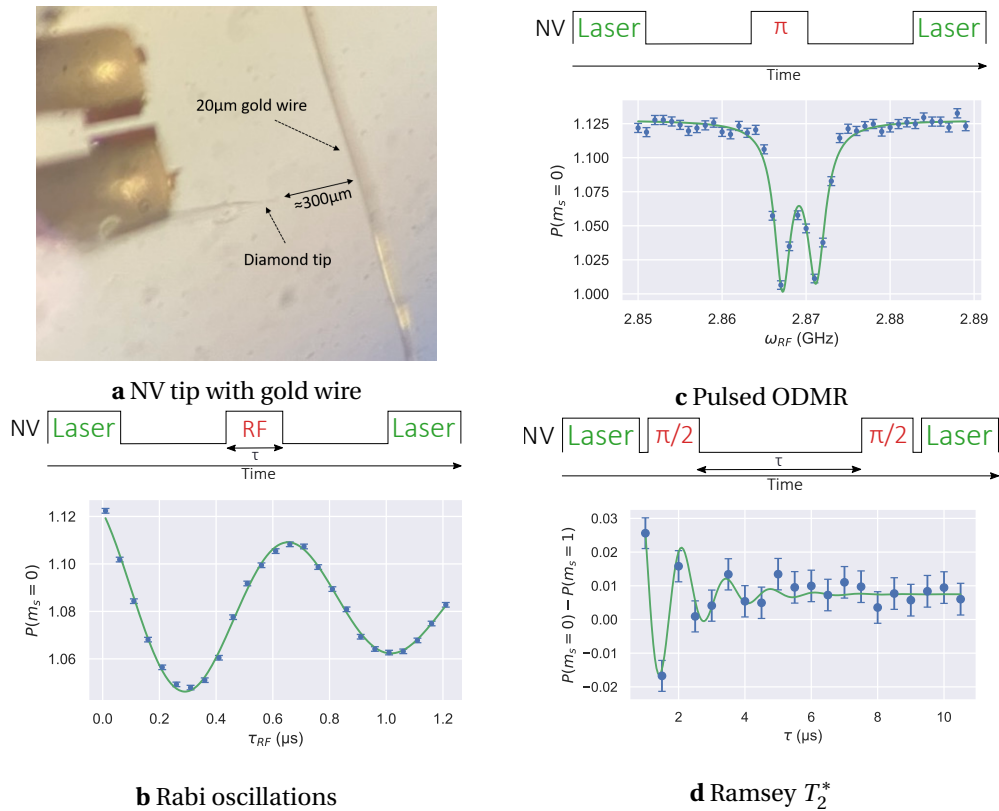


Fig. 4.8: **a** Camera image of a single NV AFM tip with a 20 μm gold wire bonded $\approx 300 \mu\text{m}$ away. Measurements on a single NV diamond tip showing the pulse sequence and results of, **b** Rabi measurement, data fit to an exponentially decaying sinusoid model. **c** Pulsed ODMR measurement, data fit to double Lorentzian dip model. **d** Ramsey T_2^* measurement performed in alternating mode, data fit to an exponentially decaying sinusoid. Error bars in all measurements indicate photon shot noise.

manifests itself by lowering the Q-factor of the resonance curve, along with introducing a Fano asymmetry in the corresponding line shape.

To counter the effects of this crosstalk, we use an op-amp to invert part of the excitation signal and then phase shift it by 270° . The circuit for this is described in § 3.2.3. This phase shifted signal is then added to the readout signal, where the parasitic capacitance signal is shifted in by 90° relative to the excitation signal. By carefully adjusting the amplitude of the inverted signal, we can cancel out the crosstalk, and recover the Q-factor and Lorentzian line shape of the resonance curve. The result of this is shown in Fig. 4.9a.

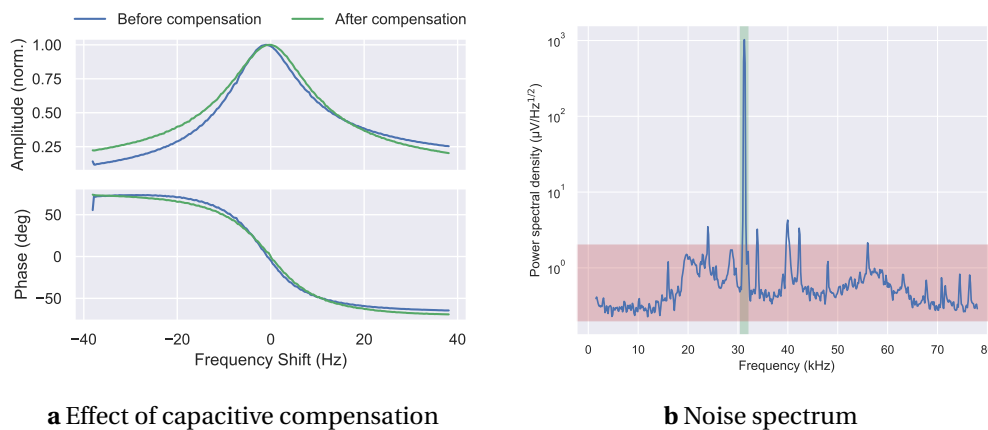


Fig. 4.9: **a** Frequency resonance curve before and after capacitive compensation. Resonance frequency is 31.256 kHz and the Q-factor of the compensated curve is 1834. **b** Noise spectrum of the AFM tip with the AFM signal (green shaded region) roughly three orders of magnitude larger than the noise floor (red shaded region).

After correcting for the parasitic capacitance, the AFM was tested in a variety of operating modes.

Amplitude modulation with excitation In this mode, the oscillation amplitude (excitation) of the tip is modulated by the AFM signal (amplitude). This is done by using PLL locked to the amplitude, and any changes in the amplitude are fed back into a P-T loop modulating the excitation.

Amplitude modulation with z-feedback In this mode, the oscillation amplitude (excitation) of the tip is kept constant, but the z piezo distance is modulated by the AFM signal (readout). This is done by using PLL locked to the amplitude, and any changes in the amplitude are fed back into a P-T loop modulating the z piezoelectric motor height.

Amplitude modulation with z-feedback and phase modulation In addition to the previous case, the frequency of the excitation is modulated to keep the phase constant. This is done by using PLL locked to the phase, and any changes in the phase are fed back into a P-T loop modulating the resonance frequency of the excitation.

In our testing, we get the best results in amplitude modulation with excitation, and amplitude modulation with z-feedback. All measurements presented ahead use either of these two modes.

4.6.1 AFM on Si/SiO₂ grating

The grating sample consists of a silicon substrate with a silicon dioxide layer deposited on top. The active area is 1 mm × 1 mm, and is divided into 4 × 4 chess fields, each with a size of 250 μm × 250 μm. A schematic of the grating is shown in Fig. 4.10a. The height of the grating is (19 ± 2) nm, and the chess pitch is 2 μm. The grating sample was first imaged with a commercial Bruker© AFM, the result of which is shown in Fig. 4.10b.

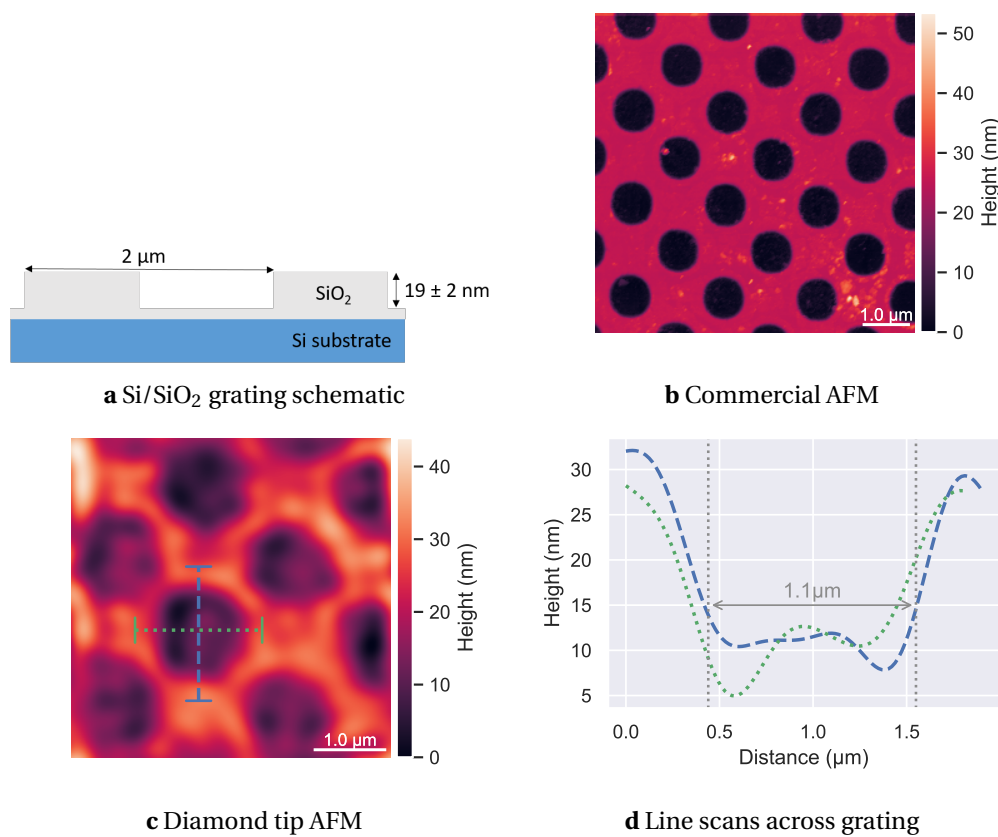


Fig. 4.10: **a** Schematic of the calibration grating sample. **b** AFM image of the calibration grating sample taken with a commercial Bruker© AFM. **c** AFM image of the calibration grating sample taken with a diamond tip. **d** Horizontal (dotted green line) and vertical (dashed blue line) scans across a grating showing a mean grating width of $\approx 1 \mu\text{m}$.

This grating sample was then imaged with a diamond tip using the amplitude modulation with z-feedback mode, the result of which is shown in Fig. 4.10c. From the image, we can clearly resolve several individual gratings, and a line scan across a grating is shown in Fig. 4.10d. We use this line scan to calibrate the piezoelectric scanners. The x , y and z scanners are calibrated by measuring the distance between, and the height of the gratings respectively.

5 Imaging domain walls in synthetic antiferromagnetic thin films

Magnetism, as you recall from physics class, is a powerful force that causes certain items to be attracted to refrigerators.

Dave Barry

Parts of this chapter are based on all-optical experiments in

D. Paone, D. Pinto, G. Kim, L. Feng, M.-J. Kim, R. Stöhr, A. Singha, S. Kaiser, G. Logvenov, B. Keimer, J. Wrachtrup, and K. Kern, “All-optical and microwave-free detection of Meissner screening using nitrogen-vacancy centers in diamond”, [Journal of Applied Physics](#) **129**, 024306 (2021)

Synthetic antiferromagnetic (SAF) thin films have become a key building block for spintronic technologies, particularly in the domain of magnetic storage⁷⁷. Unlike ferromagnetic materials, AF thin films only exhibit an atomic scale net magnetic moment. This weak magnetic nature places strict requirements on spatial resolution and magnetic sensitivity of the sensor, resulting in measurements performed using techniques such as X-ray photoemission electron microscopy^{78,79} and spin-polarized scanning tunneling microscopy^{80–82}. These techniques have demonstrated sufficient spatial resolution and magnetic sensitivity. However, they require either complex synchrotron facilities, or are limited to using only electronically conducting samples.

A more versatile approach is to image the stray magnetic fields or magnetic noise generated by the sample, with techniques such as magnetic force microscopy (MFM)^{83,84} and nitrogen vacancy scanning probe microscopy (NV-SPM)^{67,85–87}. NV-SPM in particular is non-invasive, and does not require exposing the sample to a magnetic field, such as those generated by an MFM tip. In addition to the ESR pulse toolkit we used previously (see [Chapter 2](#)), the NV also has the ability to perform all-optical relaxometry measurements. This measurement modality has been particularly successful, demonstrating fast acquisition times and high sensitivity⁸⁸.

In this chapter, we perform nanoscale, all-optical relaxometry measurements with an NV-SPM on antiferromagnetically coupled multilayer films. We observe clear domain wall structures, which are in good agreement with previously reported observations on such classes of materials^{89,90}, and also with our MFM measurements on the same sample, demonstrating the functionality of our NV-SPM.

Collaborations

Both antiferromagnetically coupled multilayer thin films were fabricated in the group of Jürgen Faßbender*. EBL of gold markers was performed by Toni Hache**.

*Helmholtz-Zentrum Dresden-Rossendorf e.V., Institute of Ion Beam Physics and Materials Research, Dresden, Germany

**Max Planck Institute for Solid State Research, Stuttgart, Germany

5.1 Multilayer films of Co, Pt and Ru

Multi-layers consisting of [Co/Pt] and [Co/Ru] are popular systems for studying domain wall structures^{91,92}. The Co-Pt interface introduces a symmetry breaking effect resulting in a perpendicular magnetic anisotropy, and the adjacent layers couple ferromagnetically. Replacing the Pt at specific intervals with Ru results in a system with antiferromagnetic (AF) coupling between the adjacent layers⁹⁰. The result, $[[\text{Co}(4\text{Å})/\text{Pt}(7\text{Å})]_{X-1}/\text{Co}(4\text{Å})/\text{Ru}(9\text{Å})]_N$, is made up of N ferromagnetic $[\text{Co}(4\text{Å})/\text{Pt}(7\text{Å})]_X$ sub-layer stacks with perpendicular anisotropy. Each sub-layer stack is AF coupled to adjacent sub-layer stacks⁹⁰. Below critical values of X and N , an AF ground state is observed. As X and N are increased beyond the critical point, the AF ground state transitions to a ferromagnetic stripe domain ground state⁸⁹.

The ferromagnetic stripe domain is formed by a naturally occurring domain wall shift within each [Co/Pt] sub-layer relative to the neighboring sub-layers⁹⁰. This is shown schematically in Fig. 5.1a. In ferromagnetic thin films with perpendicular anisotropy, this effect is mediated by the balance between exchange, anisotropy and dipolar energies⁹³. The exact proportion of the different energies results in distinct sample “modes”, which can either be horizontally or vertically correlated. Horizontal correlation results in a ferromagnetic ground state, while vertical correlation results in ferromagnetic stripe domains⁹⁰. A schematic diagram of the vertically correlated states is shown in Fig. 5.1b.

5.2 Measurement principles

The imaging measurements are performed with a single NV center inside a diamond tip with parabolic geometry⁹⁴. The tip is implanted with ¹⁵N at an energy of 12 keV, leading to a nominal depth of (17 ± 6) nm. The nominal depth is calculated using the SRIM software package, and represents a lower bound value. The tips are manufactured by Qnami AG (Qantilever MX+), and are mounted onto a custom tip holder (see § 3.2.2). The measurements were performed at ambient conditions with zero applied external field ($B_z = 0$).

The imaging principle is based on the spin dependent PL response of the ground state of

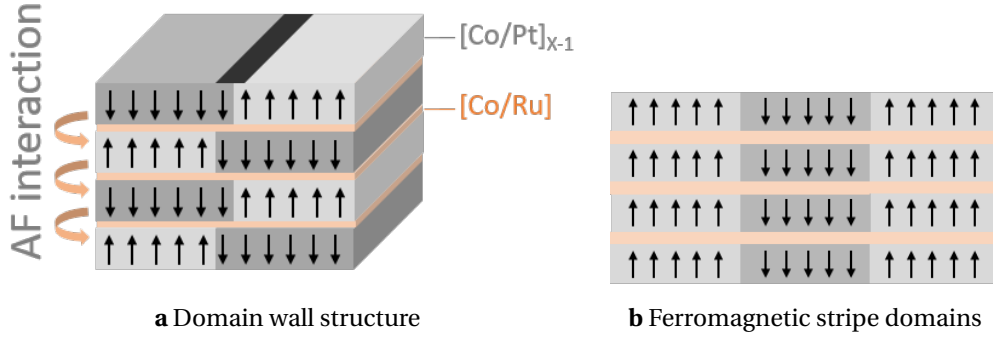


Fig. 5.1: Schematic illustrations of the antiferromagnetically coupled multilayer sample $[[\text{Co}(4\text{\AA})/\text{Pt}(7\text{\AA})]_{X-1}/\text{Co}(4\text{\AA})/\text{Ru}(9\text{\AA})]_N$. **a** Magnetic domain wall structure in N antiferromagnetically coupled layers of $[\text{Co}(4\text{\AA})/\text{Pt}(7\text{\AA})]_{X-1}$ separated by layers of $[\text{Co}(4\text{\AA})/\text{Ru}(9\text{\AA})]$. **b** Vertically correlated remanent states forming ferromagnetic stripe domains with alternating out-of-plane and in-plane magnetization.

the NV center. This is shown schematically in Fig. 5.2a, where $m_s = 0$ is the “bright” state and $m_s = \pm 1$ are the “dark” states. When exposed to laser illumination, the steady state spin population is formed by a competition between the spin relaxation rate $\Gamma_r \approx 1/T_1$, and optically pumped spin polarization rate Γ_p , which is function of applied optical excitation power. Generally, the NV operated is under the condition $\Gamma_r \ll \Gamma_p$, which efficiently polarizes the NV into $m_s = 0$. However, in the presence of magnetic noise, this dynamic changes such that $\Gamma_r \sim \Gamma_p$, degrading the NV spin polarization and reducing the emitted photoluminescence, effectively writing the magnetic noise into the NV-PL signal^{95–97}.

Maximizing the NV-PL contrast requires a balance between the spin relaxation rate and the optical pumping rate. This requires careful tuning of the optical excitation power. The variation of NV counts as a function of optical excitation power is shown in Fig. 5.2b, where a saturation power $P_{\text{sat}} = 177\mu\text{W}$ is observed. For all measurements, unless otherwise specified, the NV was excited with a laser power of $\approx 60\mu\text{W}$, corresponding to $P/P_{\text{sat}} = 0.33$. The NV count rate for this power is ≈ 180 kcps.

5.3 NV-SPM on an (X=7, N=17) multilayer

The first multilayer sample probed was $[[\text{Co}(4\text{\AA})/\text{Pt}(7\text{\AA})]_6/\text{Co}(4\text{\AA})/\text{Ru}(9\text{\AA})]_{17}$. To give us reference points in the AFM scans, cross-shaped gold markers were defined on the surface of the sample using electron beam lithography (EBL). Fig. 5.3a shows a $15\mu\text{m} \times 15\mu\text{m}$ MFM scan over the region surrounding a gold marker. We observe an extremely dense array of domains covering the sample. Fig. 5.3b shows an $6\mu\text{m} \times 6\mu\text{m}$ NV photo-luminescence scan over a similar region neighboring a gold marker. The gold marker itself shows up very clearly with a high count rate, likely due to optical emission from the gold in the NV emission range. However, we do not clearly resolve any magnetic structures in the region around the marker. This is somewhat strange, as based on the size of the structures observed in the MFM, the domains should be well within the spatial resolution of the NV-SPM.

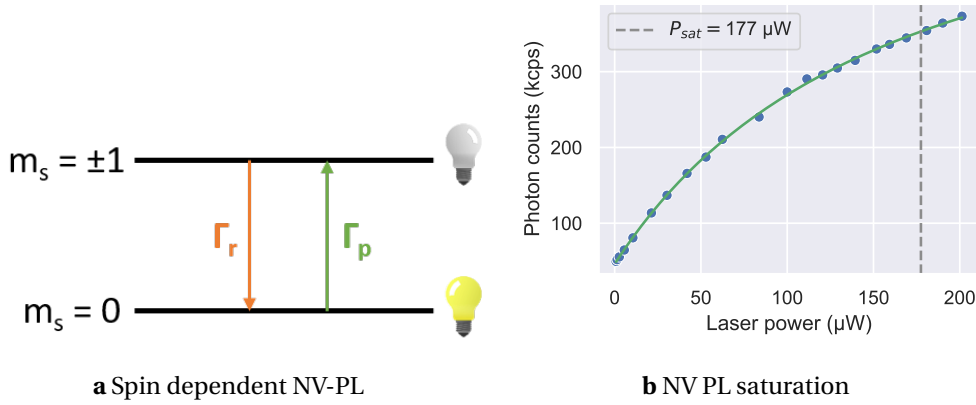


Fig. 5.2: **a** Simplified two-level structure of the NV center ground state showing the spin relaxation rate Γ_r , and optically pumped spin polarization rate Γ_p . **b** Optical saturation curve of a single NV center in a parabolic diamond tip. Data fit to a hyperbolic saturation function, revealing a saturation power $P_{sat} = 177 \mu\text{W}$.

We do however, observe larger features showing an oscillatory pattern in the PL. These are shown in Fig. 5.3c. The features are extremely clear, with a contrast of $\approx 25\%$, but are too broad to be domain walls, so their origin is unclear. However, we observed them consistently in several regions of the sample. The corresponding AFM scans also confirmed that there was no topographical origin associated with these features.

5.3.1 Variation with scan height and laser power

To gain more information about these features, we can look to the measurements performed by Finco et al. [88], where they observed that the contrast of surface magnetic structure was a function of NV-sample distance and laser power. To test this, we performed a series of NV-SPM scans with the NV-sample distance varied up to 700 nm^i , and with the laser power varied from $P/P_{sat} = 0.02$ to 0.14 . All the scans are normalized to the mean value of the fluorescence counts obtained from the full confocal scan.

Fig. 5.4a shows the variation in NV-PL as a function of NV-sample distance. The zero point in this figure is defined as the point just above where the oscillation amplitude of the AFM tip drops sharply, indicating tip-sample contact. The height values are read out from a calibrated z -piezoelectric scanner. However, we would like to stress that we have observed non-linear behavior in the motion of our piezoelectric scanners (discussed further in § 3.2.1), and the height values should only be treated as rough estimates of the distance. We observe a sharp drop in feature contrast as the NV tip moves away from the sample, clearly indicating that the presence of a surface feature.

Fig. 5.4b shows the variation in NV-PL as a function of laser power. The features are visible at all laser powers, however the contrast drops significantly at low laser powers. This is likely due

ⁱNote that due to the non-linear behavior of the piezoelectric motors, this value at best is rough approximation.

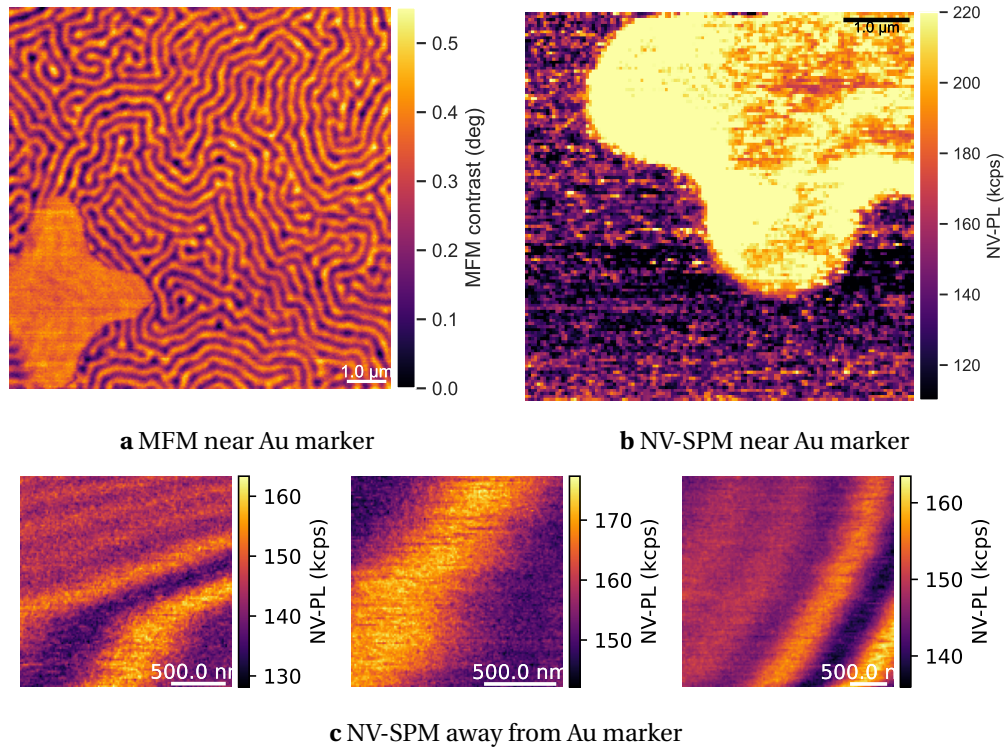


Fig. 5.3: Magnetic force microscopy (MFM) and NV-SPM measurements performed on $[[\text{Co}(4\text{\AA})/\text{Pt}(7\text{\AA})]_6/\text{Co}(4\text{\AA})/\text{Ru}(9\text{\AA})]_{17}$. **a** $15\mu\text{m} \times 15\mu\text{m}$ MFM scan showing an antiferromagnetic ground state along with a gold marker etched using EBL. **b** $6\mu\text{m} \times 6\mu\text{m}$ NV photoluminescence scan clearly resolving the gold marker, but showing no clearly discernible features outside the marker. Scan performed in AM mode with z-feedback ($f_0 = 31.274\text{kHz}$, $A_{\text{set}} = 3.3\text{nm}$). **c** NV-PL scans on different parts of the sample showing broad oscillatory features. The features only appear on the PL, and have no topographic signature. Scans performed in AM mode with excitation feedback ($f_0 = 31.274\text{kHz}$, $A_{\text{set}} = 1.7\text{nm}$)

to the fact that the NV-PL signal has a high noise floor at low laser powers, moving closer to saturation power improves the image contrast.

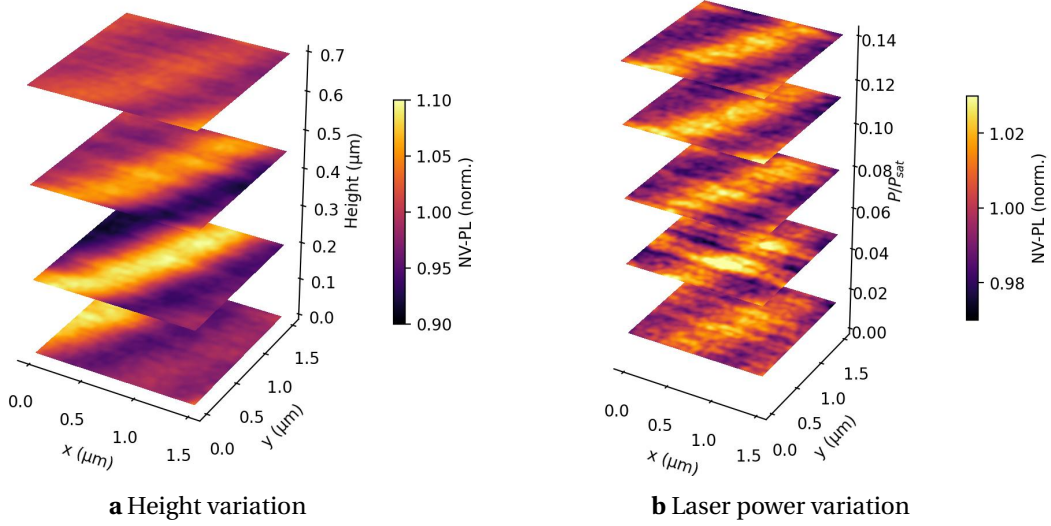


Fig. 5.4: **a** Variation of the oscillatory features with height of the NV tip from the sample. As the tip moves further from the sample the contrast of the features drops significantly. **b** Variation of the oscillatory features with laser power. The features show a high noise floor at very low laser power, which drops significantly as we move closer to saturation power $P_{\text{sat}} = 177 \mu\text{W}$. In both figures the data is normalized to the mean counts of the scan, all scans performed in AM mode with excitation feedback ($f_0 = 31.274 \text{ kHz}$, $A_{\text{set}} = 1.7 \text{ nm}$)

In summary, the NV-SPM measurements on $[[\text{Co}(4\text{\AA})/\text{Pt}(7\text{\AA})]_6/\text{Co}(4\text{\AA})/\text{Ru}(9\text{\AA})]_{17}$ do not clearly resolve the dense domain wall structures that is expected based on our MFM measurements. We instead observe a broad oscillatory feature across several areas on the sample. A possible explanation for this is that the stray field of the sample experienced by the NV-center is simply too strong given the tip-sample proximity. This is consistent with the fact that the stray field is proportional to the number of layers in the sample, in this sample ($X = 7$, $N = 17$), which is quite high. To quantitatively estimate this, we can perform ODMR measurements with the NV tip, but this is beyond the scope of this thesis. Therefore, to reduce the stray field, we tested the NV-SPM with a sample with $X = 6$, $N = 4$. The measurements on this sample are described in the next section.

5.4 NV-SPM on an (X=6, N=4) multilayer

As described in the previous section, we only observe broad oscillatory features on a multilayer sample with $X = 7$, $N = 17$. In this section, we describe the measurements performed on a sample with $X = 6$, $N = 4$. This sample has a completely distinct magnetic structure, as is evidenced by the MFM measurements shown in Fig. 5.5a. Unlike the highly dense “ensemble” of small domains in the previous sample, this sample only shows a few large and clearly defined domains. The observed domains vary significantly in size, with the largest domain $\approx 20 \mu\text{m}^2$ in size, and the smallest domain $\approx 3 \mu\text{m}^2$ in size.

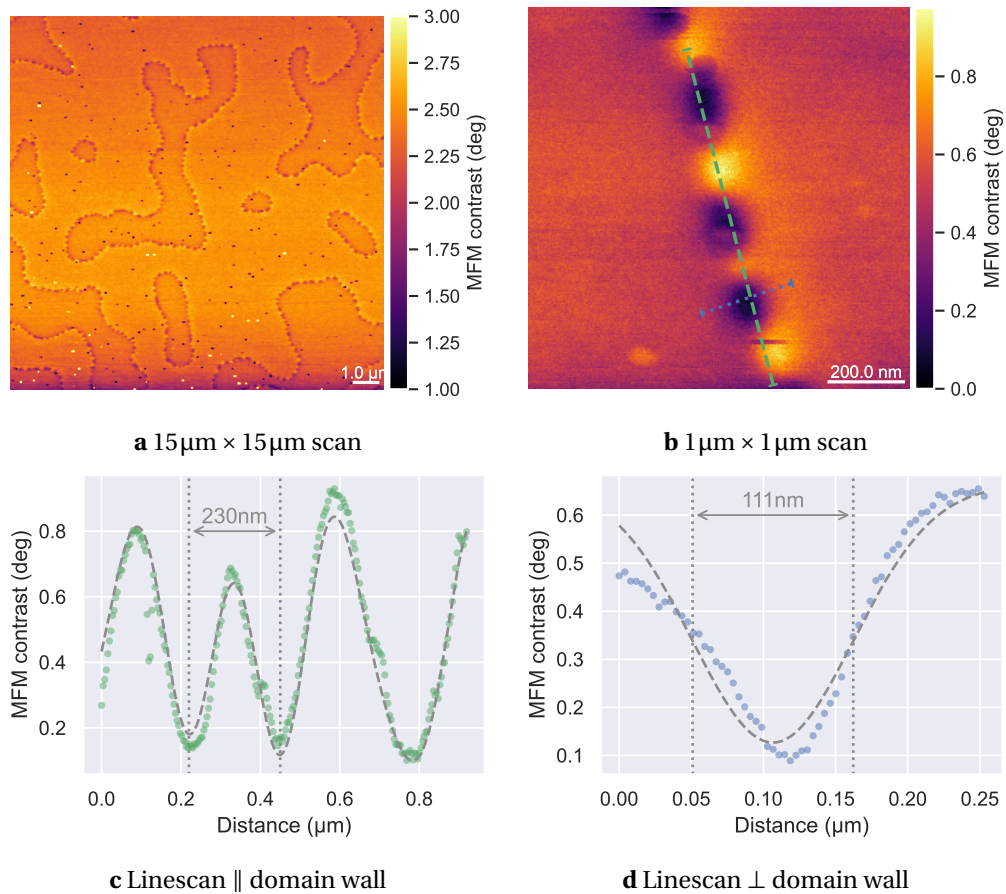


Fig. 5.5: Magnetic force microscopy (MFM) measurements performed with a commercial MFM on $[[\text{Co}(4\text{\AA})/\text{Pt}(7\text{\AA})]_5/\text{Co}(4\text{\AA})/\text{Ru}(9\text{\AA})]_4$ where, **a** is a $15\mu\text{m} \times 15\mu\text{m}$ scan showing the surface covered with magnetic domain walls, and **b** is a $1\mu\text{m} \times 1\mu\text{m}$ scan showing a single domain wall with a stripe pattern. **c** Line scan across the domain wall (dashed green line), gray dashed line indicates sinusoid fit showing a stripe pattern with a periodicity of (230 ± 3) nm. **d** Line scan through the domain wall (dotted blue line), gray dashed line indicates Gaussian fit showing a domain wall width (FWHM) of (111 ± 5) nm.

Zooming into the domain wall, shown in Fig. 5.5b, we can clearly resolve a ferromagnetic domain stripe pattern as described in § 5.1. To extract quantitative information about the domain wall structure, we take a line scan across (dashed green line) and through (dotted blue line) the domain wall. Fig. 5.5c shows a line scan across the domain wall, clearly resolving the oscillatory behavior of the stripe pattern. The data is fit to a sinusoidal function, and the period of the oscillation was found to be (230 ± 3) nm. Taking a line scan through the domain wall at one of the dark regions (see Fig. 5.5c), and fitting the data to a Gaussian function, we extract a wall width (FWHM) of (111 ± 5) nm. We would like to stress that these exact values are not sacrosanct, and the size of the stripes can vary across a domain wall depending on the exact nature of spin orientation in the [Co/Pt] layers.

The sample was then probed with the NV-SPM. Recall that as the NV sees a higher stray field, it will increase the spin relaxation rate $\Gamma_r \approx 1/T_1$. Under continuous laser excitation i. e. constant optically pumped spin polarization rate Γ_p , the steady state of the system will not polarize efficiently into $m_s = 0$, leading to a drop in the NV-PL signal. Fig. 5.6a shows a $6\mu\text{m} \times 6\mu\text{m}$ scan of the NV-PL signal. We observe a relatively flat background PL, punctuated by several sharp lines where the PL is quenched, clearly resolving several domain wall structures. We note here that resolving the full stripe pattern of the domain wall would require quantitative measurements such as ODMR.

Zooming into a domain wall (Fig. 5.6b), and taking a line scan through the wall (dashed blue line). We see a clear drop in NV-PL (Fig. 5.6c), with a contrast of $\approx 18\%$. The data is fit to a Gaussian function, revealing a wall width (FWHM) of (155 ± 4) nm. To estimate how strongly the steady state spin population was affected by the presence of the domain wall (see § 5.2), we use a T_1 relaxometry measurement (pulse sequence in Fig. 1.6). The tip was first placed on top of an anti-ferromagnetic (AF) domain and the NV spin relaxation was measured to be (281 ± 66) μs . The tip was then moved to the domain wall, revealing a T_1 of (100 ± 18) μs . Finally, the tip was retracted from the sample, and the T_1 was found to be (2.4 ± 0.4) ms. The large drop in spin coherence near the sample indicates the presence of strong magnetic field noise, which is further enhanced at the domain wall, and is consistent with the observed drop in NV-PL.

This measurement clearly indicates that our NV-SPM is capable of probing weak magnetization at the nanoscale. In the next section, we discuss the challenges of performing a similar measurement with a conventional diamond tip geometry.

5.5 Permanent quenching of conventional NV tips

Using a single parabolic diamond tip, we were able to comfortably measure on several different magnetic samples for several weeks. Unfortunately (and maybe even interestingly), this was not the case for conventional diamond tips. Across three different conventional diamond tips, we observed a permanent NV quenching effect after approaching a magnetic sample. Fig. 5.7c shows two examples of confocal scans taken on conventional diamond tips before and after approach. Note that the confocal scans make it clear that the tip was not damaged in

5.5 Permanent quenching of conventional NV tips

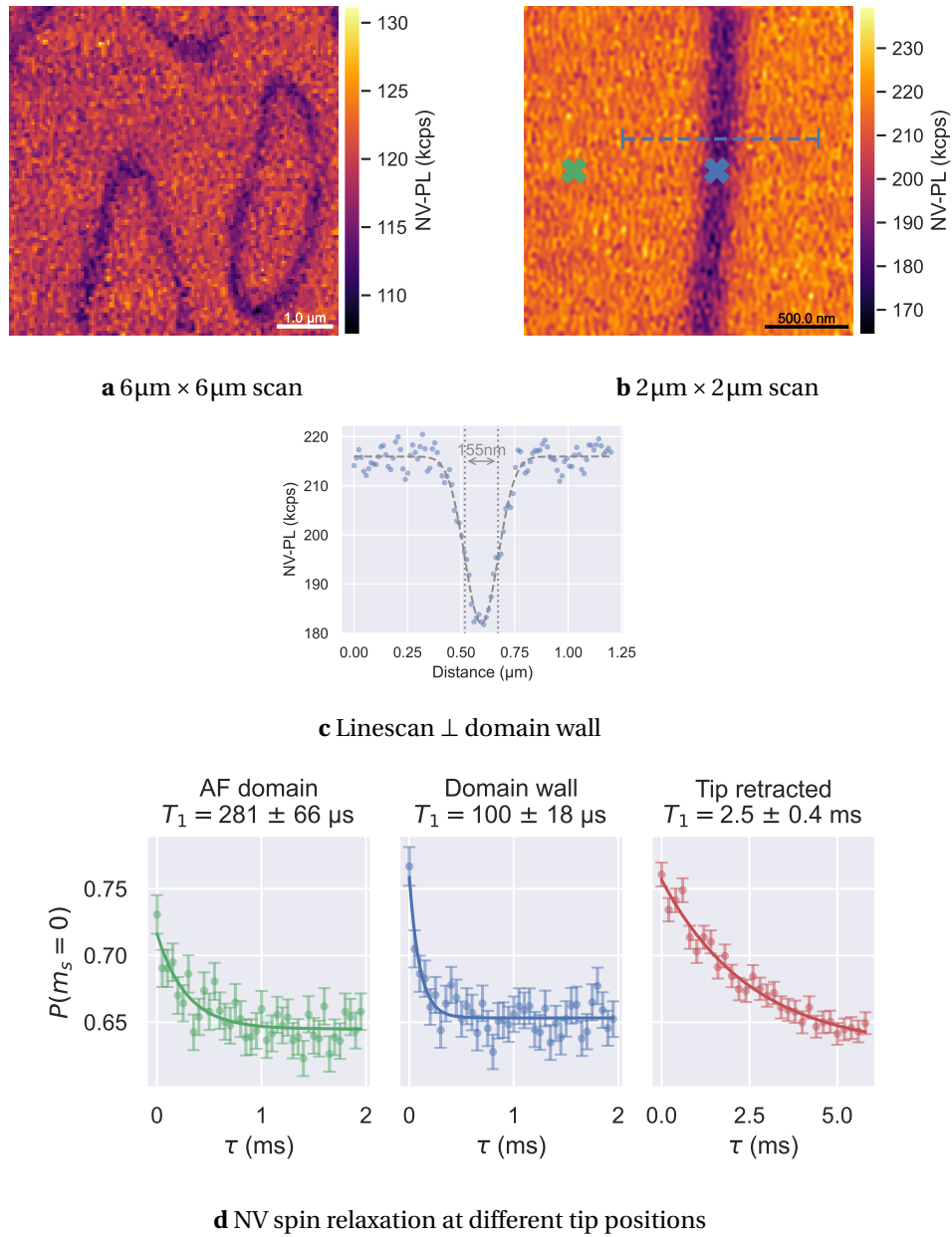


Fig. 5.6: NV-SPM photo-luminescence maps on $[[\text{Co}(4\text{\AA})/\text{Pt}(7\text{\AA})]_5/\text{Co}(4\text{\AA})/\text{Ru}(9\text{\AA})]_4$ where, **a** is a $6\mu\text{m} \times 6\mu\text{m}$ scan resolving several anti-ferromagnetic domains separated by ferromagnetic domain walls. Total acquisition time for the image was 17 min 13 s. Scan performed in AM mode with z-feedback ($f_0 = 28.269\text{ kHz}$, $A_{\text{set}} = 1.4\text{ nm}$). **b** A $2\mu\text{m} \times 2\mu\text{m}$ scan showing a single domain wall. Dashed line indicates line scan through domain wall. Crosses indicate the positions of the AF domain and domain wall used for the spin relaxation measurements. **c** Line scan through the domain wall, gray dashed line indicates Gaussian fit showing a domain wall width (FWHM) of $(155 \pm 4)\text{ nm}$. To improve statistical estimates, a $\approx 100\text{ nm}$ wide domain wall region was averaged to generate the profile. **d** NV spin relaxation curves measured for three different tip positions. The T_1 time is obtained from an exponential decay fit (solid line).

any way during approach, but the fluorescence of the single NV center has been completely quenched. The NV fluorescence was not recovered after the tip was fully retracted from the sample, indicating a permanent change in the tip.

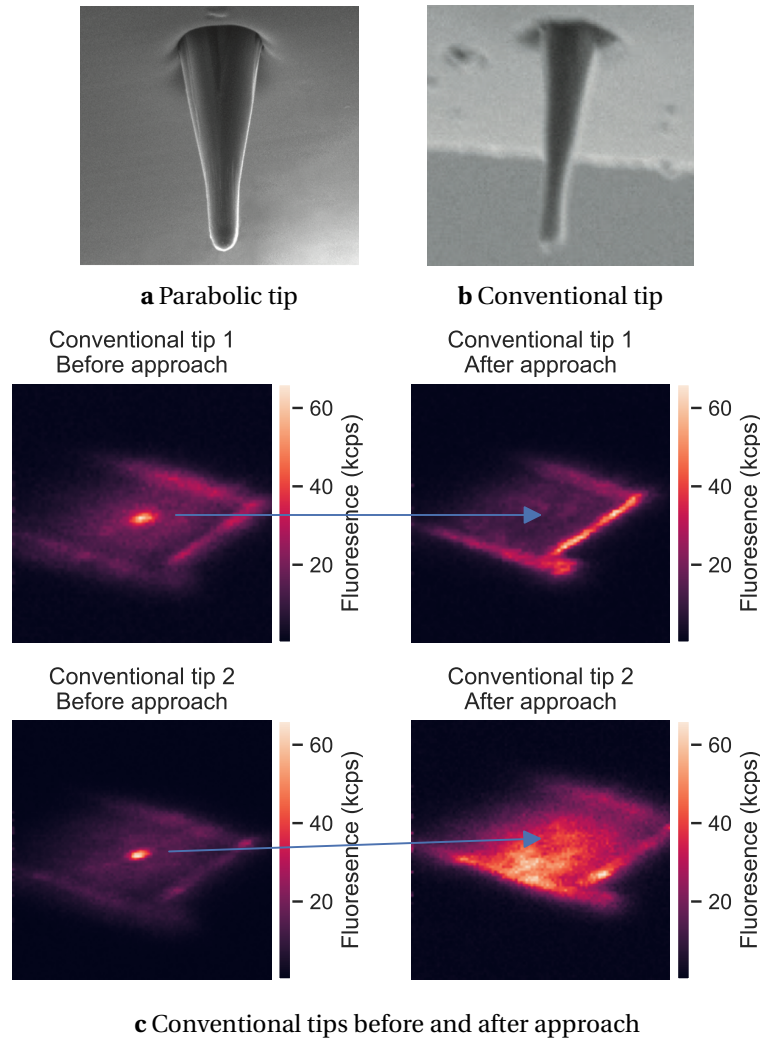


Fig. 5.7: SEM images (from Qnami AG) of, **a** parabolic diamond tip (apex diameter 200 nm) and **b** conventional diamond tip (apex diameter 100 nm). **c** Confocal scans of two different conventional diamond tips before and after approach on $[[\text{Co}(4\text{\AA})/\text{Pt}(7\text{\AA})]_5/\text{Co}(4\text{\AA})/\text{Ru}(9\text{\AA})]_4$. Complete NV quenching is observed in both cases with no damage to the tip itself. The NV fluorescence was not recovered after retracting the tip, likely indicating loose magnetic material on the sample surface has been picked up by the tip.

The most likely explanation for this is that the tip is picking up magnetic material from the sample surface. This magnetic “dirt” sits near the diamond tip apex and generates a strong magnetic field in the proximity of the NV, completely quenching the NV fluorescence. We attempted to bleach the dirt by applying a strong optical excitationⁱ, but this did not recover

ⁱThis must be done with caution, as the NV itself can be ionized by strong laser irradiation

the NV fluorescence.

A possible explanation as to why this only happened for the conventional tips and not for the parabolic tips, could be attributed to their apex radius. The parabolic tips have a larger apex radius (200 nm) than the conventional tips (100 nm). This larger apex radius, while not ideal for AFM topographic resolution, could be creating a larger distance between the NV and the magnetic dirt picked up at the edges of the tip. Fig. 5.7a and Fig. 5.7b show SEM images of the apex of the parabolic and conventional tips, respectively. In order to perform measurements with more controlled surface properties, a cleaner environment, such as at UHV conditions could help solve this problem. In the next chapter, we examine the behavior of NV diamond tips in a vacuum environment.

6 Vacuum induced charge state transition of NV diamond tips

Protons give an atom its identity,
electrons its personality.

Bill Bryson

Parts of this chapter are based on dosing experiments in

J. N. Neethirajan, T. Hache, D. Paone, D. Pinto, A. Denisenko, R. Stöhr, P. Udvarhelyi, A. Pershin, A. Gali, J. Wrachtrup, K. Kern, and A. Singha, “Controlled Surface Modification to Revive Shallow NV⁻ Centers”, *Nano Letters*, 10.1021/acs.nanolett.2c04733 (2023)

As we have demonstrated over the course of this thesis, near-surface negatively charged NV centers are incredible quantum sensors. Despite this, they are also subject to a number of other effects, such as charge state transitions, which often lead to a loss of coherence. Such charge state transitions can have a particularly deleterious effect when the NV center is used under vacuum conditions. In this chapter, we demonstrate the first measurements examining the charge state behavior of the NV center in diamond tips as a function of vacuum. Using spectroscopic and second-order correlation measurements, we report a clear charge state transition from NV⁻ to NV⁰. We also observe anomalous effects related to the confocal “size” of the NV center when it undergoes this transition. Finally, we demonstrate that the vacuum induced transition to NV⁰ can be completely reversible.

6.1 NV center charge states

The NV center, as was described in [Chapter 1](#), is composed of a six electron system. Group theoretically, we can construct single electron orbital representations – $a_1(1)$, $a_1(2)$ of A_1 symmetry and e_x, e_y of E symmetry^{12,13}. In our analysis, we somewhat implicitly assumed a ground state configuration orbital configuration given by $[a_1(1)]^2[a_1(2)]^2(e_x e_y)^2$. The motivation for this choice is that it is the only configuration of the NV center resulting in a ground state level structure suitable for sensing purposes i. e. NV⁻.

However, there are two more additional configurations possible, namely $[a_1(1)]^2[a_1(2)]^2(e_y)$,

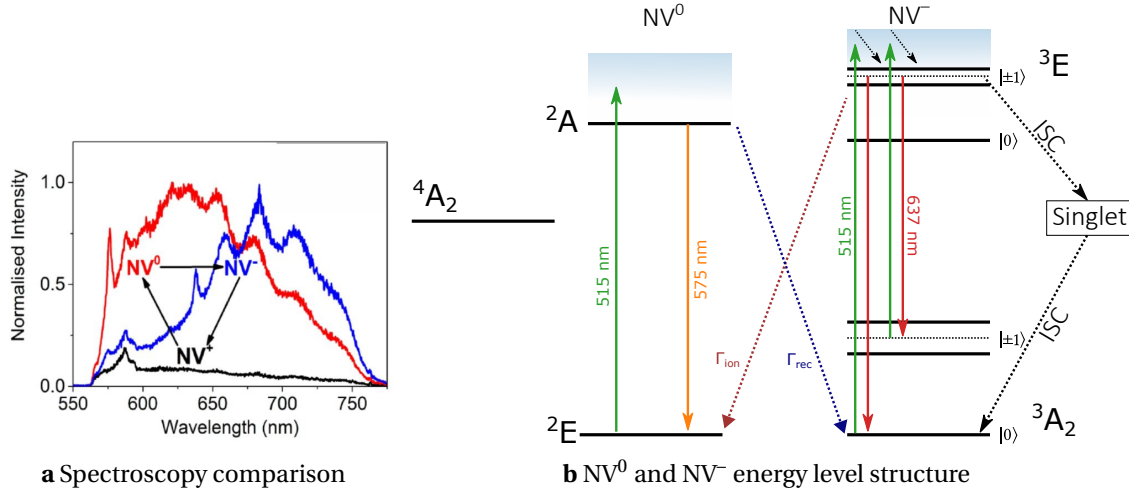


Fig. 6.1: **a** Spectroscopic comparison of the NV charge states. The NV^+ center is optically dark and does not show characteristic emission features. The NV^- exhibits a ZPL at 637 nm and NV^0 exhibits a ZPL at 575 nm. Figure adapted from Schreyvogel et al. [100]. **b** Energy level structure of NV^0 and NV^- with recombination rate Γ_{rec} and ionization rate Γ_{ion} .

and $[a_1(1)]^2[a_1(2)]^2$. These configurations represent the NV^0 and NV^+ charge states respectively. The different charge states vary in their ground state energy level structure, and as a result, their spectroscopic properties. This variation is shown in Fig. 6.1a. The NV^+ charge state is optically dark, and only the 2nd order Raman line is visible in the spectrum. The NV^0 charge state exhibits a zero-phonon line (ZPL) at 575 nm, with phonon sidebands appearing from ≥ 600 nm. The NV^- charge state exhibits a ZPL at 637 nm, with phonon sidebands appearing at ≥ 650 nm. The NV^+ charge state is the most unstable out of the three, and requires careful surface treatment to create⁹⁹. In contrast, both the NV^0 and NV^- charge states are relatively stable.

Under illumination, the charge state conversion dynamics can be described by a system of two first-order linear rate equations (see Aslam et al. [101]),

$$\dot{p}_- = \Gamma_{\text{ion}}p_0 - \Gamma_{\text{rec}}p_- \quad (6.1)$$

$$\dot{p}_0 = \Gamma_{\text{rec}}p_- - \Gamma_{\text{ion}}p_0 \quad (6.2)$$

where p_- and p_0 are the probability of the NV^- and NV^0 charge states respectively, and Γ_{rec} and Γ_{ion} are the recombination rate ($NV^0 \rightarrow NV^-$) and ionization rate ($NV^- \rightarrow NV^0$) respectively. Higher recombination and ionization rate lead to charge state instabilities in the NV center, adversely affecting the ability of the NV center to remain in its negatively charged configuration. This effect is demonstrably enhanced the closer the NV is brought to the diamond surface^{99,102,103}, likely indicating that surface effects are involved. The effect is also particularly enhanced under vacuum conditions, as we have previously demonstrated for diamond

membrane samples⁹⁸, and in this chapter we will demonstrate for diamond tips.

A possible hypothesis to explain this behavior could be that a water layer present on the diamond surface at ambient conditions could be acting as a charge reservoir. This would have the effect of enhancing the recombination rate, and effectively “polarizing” the NV into its negatively charged state. Interestingly, this would explain why low temperature measurements at moderate vacuum ($\approx 10^{-6}$ mbar) are able to mitigate the effect, as the water layer is frozen out. This would, of course, require that water layer is frozen out *before* full vacuum conditions are established. In our previous experiments involving water dosing of diamond membranes, we only observed a minor recovery of the NV⁻ charge state. This could be due to the fact that the dosing was carried out in a separate vacuum chamber with a transfer arm and wobble stick at room temperature. This would lead to the dosed water not “sticking” to the diamond surface, and instead desorbing under vacuum conditions.

A possible solution to this limitation could be to use an evaporator capable of dosing water *in-situ* i. e. directly into the cold measurement head. While technically possible, this is not an ideal solution as it would lead to the contamination of other components in the main vacuum chamber. A better solution is to use a LHe cooled transfer arm, which would keep the sample cold during dosing. The wobble stick used to move the sample between the measurement head and transfer arm is more complicated to cool. As a rough solution, the wobble stick could be cooled by holding it in contact with the nitrogen shield, which should cool it down to ≈ 100 K.

Extrapolating this hypothesis, it is quite clear that the *worst* condition for charge state stability is room temperature and ultra-high vacuum. In the next sections, we detail our measurements performed on multiple diamond tips under these exact conditions.

6.2 Preparation

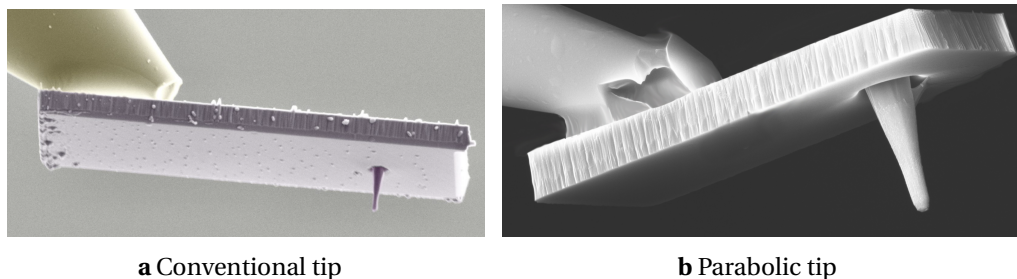


Fig. 6.2: SEM images of diamond tips in, **a** conventional geometry, the diamond plate is $19\mu\text{m} \times 6\mu\text{m}$ and, **b** parabolic geometry, the diamond plate is $18\mu\text{m} \times 8\mu\text{m}$. Images from Qnami AG.

For the measurements, we used three different diamond tips. Tips 1 and 2 use a conventional diamond nanopillar (Fig. 6.2a) to act as a waveguide for the emitted NV fluorescence. Tip 3 has a parabolic pillar geometry (Fig. 6.2b), which provides a $\approx 3\text{x}$ enhancement in signal-to-noise ratio⁹⁴. It is able to achieve this as the total internal reflection at the parabolic surface

collimates the emission into a unidirectional output mode, resulting in improved wave guiding of the NV emission. All tips are implanted with ^{15}N at an energy of 12 keV, leading to a nominal depth of (17 ± 6) nm. The nominal depth is calculated using the SRIM software package, and represents a lower bound value. The tips are manufactured by Qnami AG, and are mounted onto a custom tip holder (see § 3.2.2) immediately after being removed from their storage container. The tip holder is then transferred into the UHV stage for measurement.

6.3 Vacuum induced NV^- to NV^0 transition

After the tip is transferred into the UHV stage, it is driven into the focal point of the objective lens. To simplify the approach process, we make use of the camera setup (described in § 3.5), to perform a rough optical alignment of the tip. A fine approach is then performed with the confocal microscope, where the position of the tip is adjusted along 5 axes (x, y, z, θ, ϕ), until the count rate is maximized. After this, the collection optics are aligned to maximize confocal contrast. In all cases, the NV is excited off-resonantly with a 515 nm laser. The laser power during all measurements, unless otherwise specified, is held near saturation i. e. $\approx 80 \mu\text{W}$.

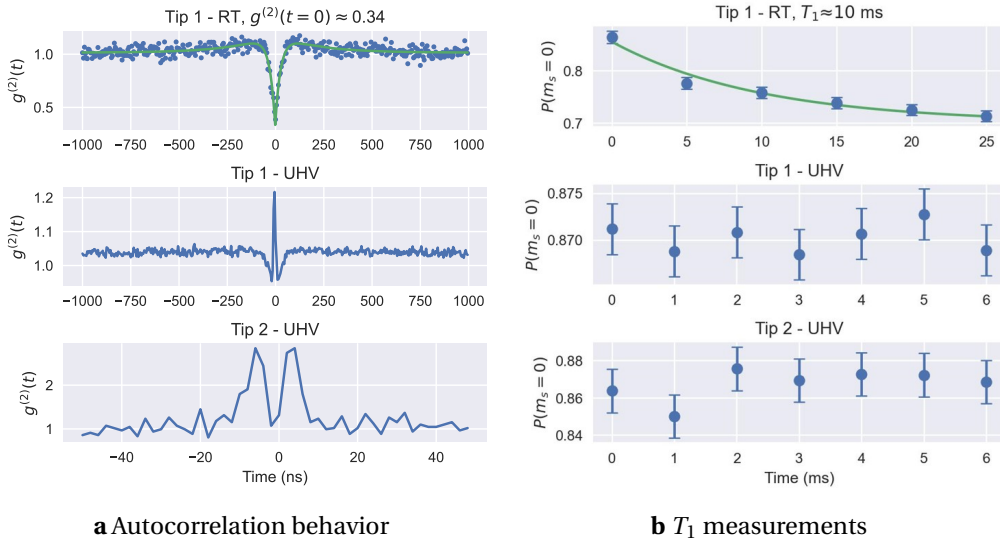


Fig. 6.3: Measurements comparing behavior of single NV centers at ambient and ultra-high vacuum ($\approx 10^{-8}$ mbar) conditions. **a** Ambient autocorrelation shows a sharp NV^- anti-bunching dip to $g^{(2)}(0) = 0.34$. At UHV the strong $g^{(2)}(0)$ dip disappears, indicating strong instability of the NV^- center. **b** Ambient T_1 measurement shows an exponential decay with a T_1 time of ≈ 10 ms. At UHV all spin coherence disappears. Photon shot noise is at least two orders of magnitude lower than measured counts.

Fig. 6.3a shows autocorrelation measurements performed across two conventional diamond tips between ambient and UHV conditions ($\approx 10^{-8}$ mbar). At ambient conditions, a clear signature of NV^- – an anti-bunching dip to $g^{(2)}(0) = 0.34$ with ≈ 400 ns sidebands is observed. At UHV, this signature disappears entirely, replaced by a very weak anti-bunching dip occurring at significantly smaller timescales (Note the x-axis timescale in the images).

Fig. 6.3b shows a T_1 measurement performed across two conventional diamond tips between ambient and UHV conditions. At ambient conditions, a clear exponential decay is observed, with a T_1 time of ≈ 10 ms. At UHV, the exponential decay disappears entirely, replaced by a flat line, indicating that the NV center has lost all spin coherence.

Both of these measurements likely indicate a transition from NV^- to NV^0 induced by vacuum conditions. However, the T_1 measurements are indirect, and only represent two discrete measurement points. They tell us nothing about the dynamics of the transition, and how it varies with vacuum pressure. To further understand this, we need to perform direct measurements across a range of pressures. As we have seen from Fig. 6.1a, the spectroscopic signature of NV^0 is clearly distinct from NV^- . We can therefore use fluorescence spectroscopy to study the charge state dynamics of the NV center as a function of pressure.

6.4 Spectroscopic variation with pressure

Spectroscopic measurements are performed by adding a 50:50 beam splitter into the collection path. The beam splitter is added after the lens-pinhole-lens combination (see Fig. 3.9a for optical schematic). On one path, a plano-convex lens focuses the light onto a $100\ \mu\text{m}$ fiber coupled to an OceanInsight QE Pro spectrometer. The spectrometer has an optical resolution of $6.87\ \text{nm}$ and wavelength range from $200\ \text{nm}$ to $1100\ \text{nm}$. On the other path, we have our standard dual-APD setup for performing confocal and second-order correlation measurements. All spectroscopic measurements were performed on a single NV center in a parabolic diamond tip. The wavelength range selected by our low and high pass filters was $550\ \text{nm}$ to $800\ \text{nm}$. Note that all pressure variation measurements were performed by starting the system from ambient conditions, and slowly progressing to lower pressure. Measurements were taken at points where the pressure could be maintained at a steady value using our multi-stage pumping system.

Fig. 6.4a shows the results of the spectroscopic measurements with varying pressure. At ambient conditions, we see a strong NV^- signature for a diamond tip, with the spectral “weight” located in the NV^- phonon sideband region in the $650\ \text{nm}$ to $750\ \text{nm}$ range. As the pressure is reduced, the spectral weight shifts to the NV^0 phonon sideband region in the $600\ \text{nm}$ to $650\ \text{nm}$ range, and the NV^- signature weakens. Note that all spectra are normalized to the total photon counts observed in the $550\ \text{nm}$ to $800\ \text{nm}$ measurement range. We can clearly see the change in spectral weight in Fig. 6.4c, where the individual spectra $I(P_i)$ at pressure P_i are subtracted from the ambient spectrum $I(P_0)$. Until $\approx 10^{-3}$ mbar no change in behavior is observed, but below this pressure the NV^- sidebands at $\geq 650\ \text{nm}$ start getting suppressed, with the NV^0 phonon sideband at $\geq 600\ \text{nm}$ becoming increasingly more dominant from 10^{-4} mbar to 10^{-5} mbar, beyond which it appears to saturate.

We can use the data in Fig. 6.4a to calculate a probability metric of observing NV^0 and NV^- . Defining the probability of observing NV^0 as P_{NV^0} , and the probability of observing NV^- as P_{NV^-} , we can calculate:

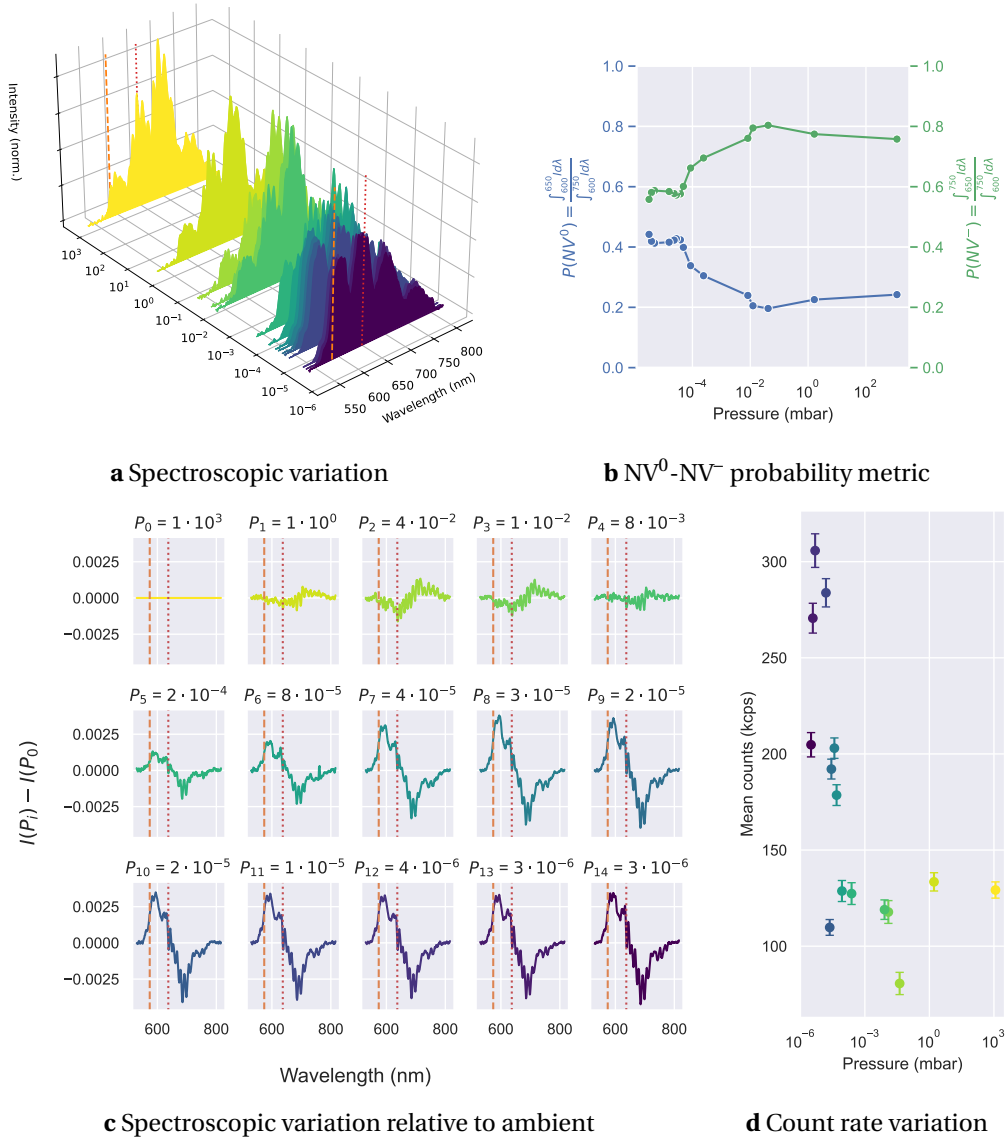


Fig. 6.4: **a** Spectroscopic measurements on a single NV center in a parabolic tip from 550 nm to 800 nm. Pressure is represented in mbar on the y-axis (out of page). NV⁰ and NV⁻ ZPL is shown at 575 nm (dashed orange line) and 637 nm (dotted red line) respectively. Ambient spectrum is measured at $P_0 = 1180$ mbar. **b** Variation of the NV⁰-NV⁻ probability metric with pressure. The probability for NV⁰ (in blue) is defined as the normalized number of photons from 600 nm to 650 nm, and the probability for NV⁻ (in green) is defines as the normalized number of photons from 650 nm to 750 nm. **c** Delta variation in the spectra relative to ambient conditions i. e. $I(P_i) - I(P_0)$, where the pressure of the i^{th} spectra is shown above the plot. In both plots the spectra are normalized to the total number of photons in the measurement window. **d** A strong overall increase in count rates from 550 nm to 800 nm is observed with decreasing pressure.

$$P_{NV^0} = \frac{I_{NV^0}}{I_{NV^0} + I_{NV^-}} \quad \text{and} \quad P_{NV^-} = \frac{I_{NV^-}}{I_{NV^0} + I_{NV^-}} \quad (6.3)$$

where,

$$I_{NV^0} = \int_{600\text{nm}}^{650\text{nm}} I(\lambda) d\lambda \quad \text{and} \quad I_{NV^-} = \int_{650\text{nm}}^{750\text{nm}} I(\lambda) d\lambda \quad (6.4)$$

The choice of 650 nm as the cut-off(on) wavelength, was based on the zero crossing of the delta spectrum in Fig. 6.4c. The probability metric curves are shown in Fig. 6.4b. We see that until 10^{-2} mbar, the probability of finding mostly NV^- state remain roughly constant, after which it drops off until 10^{-5} mbar, beyond which it saturates. Note that this metric, while useful, will be offset by the Raman lines overlapping with the NV^0 sidebands. This offset is manifested by the NV^- probability being only $\approx 80\%$ at ambient conditions (we would expect this to be near 100 %). The Raman lines should not show any pressure variation, and thus the probabilities will *qualitatively* be correct. A potential way to correct for this is to assume no NV^0 contribution at ambient conditions i. e. the data from 600 nm to 650 nm purely corresponds to Raman lines at ambient conditions and offset the $I(P_i)$ data accordingly.

In addition to the shift in spectral weight from the NV^- sidebands to the NV^0 sidebands, we observe that the number of photons in the measurement window also increases. This is clearly seen in Fig. 6.4d where the overall count rate increases from 140 kcps at ambient to a maximum of 310 kcps at $\approx 10^{-6}$ mbar. Note that in all cases the counts were measured over a 30 s period with each data point integrated for 100 ms, and the error bars represent the standard deviation in the count rate over this measurement window.

6.5 Autocorrelation variation with pressure

We now turn our attention to autocorrelation measurements. Fig. 6.5a shows the variation of autocorrelation with pressure measured on a single NV^- center in a parabolic tip. As with the spectrometry data, we see a clear NV^- autocorrelation behavior until 10^{-2} mbar. The sidebands, caused by the shelving of the NV^- electron after undergoing an ISC is clearly visible up to ≈ 400 ns. However, as we lower the pressure further, both the anti-bunching dip and the sidebands are suppressed. After 4.9×10^{-5} mbar they disappear entirely.

The theory of the three level structure of the NV^- center and its relation to the second order correlation function is described well in Berthel et al. [104]. To summarize, the excitation rate k_{12} , the spontaneous emission k_{21} , and the two parameters k_{23} and k_{31} of the additional decay path involving the shelving states. The relation between the transition rates and the second order correlation is given in Eq. 6.5:

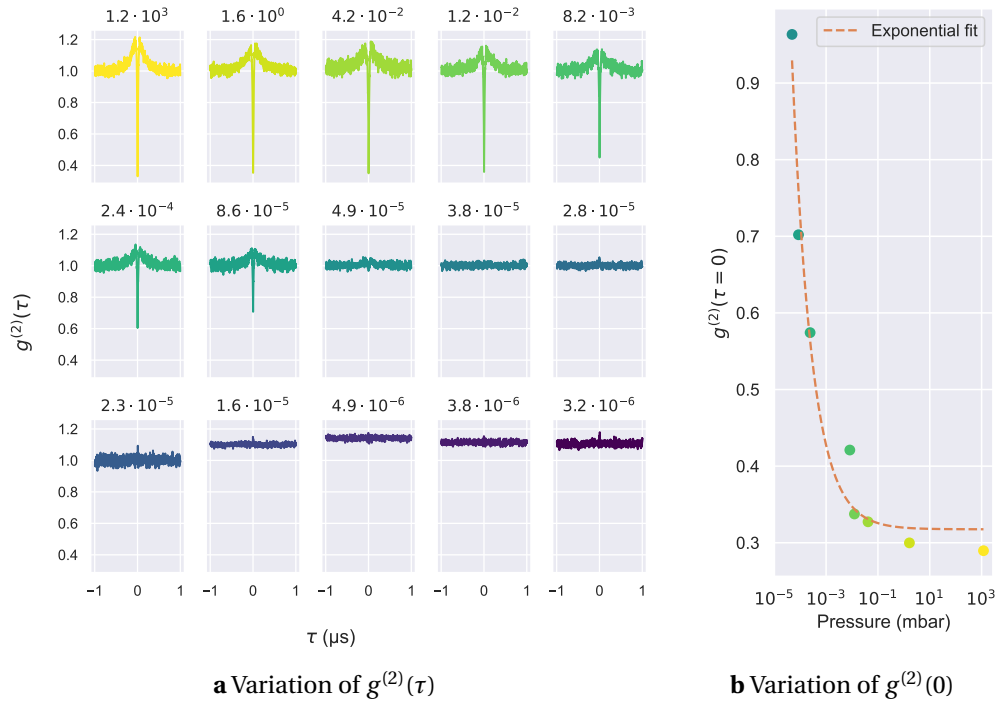


Fig. 6.5: **a** Autocorrelation measurements on a single NV center in a parabolic tip. Pressure is shown above the corresponding plot in mbar units. **b** The autocorrelation data is fit to a second-order correlation function, and $g^{(2)}(\tau = 0)$ is extracted from the fits. Note that below 4.9×10^{-5} mbar the autocorrelation data is not well fit by the second order correlation function and is therefore not shown.

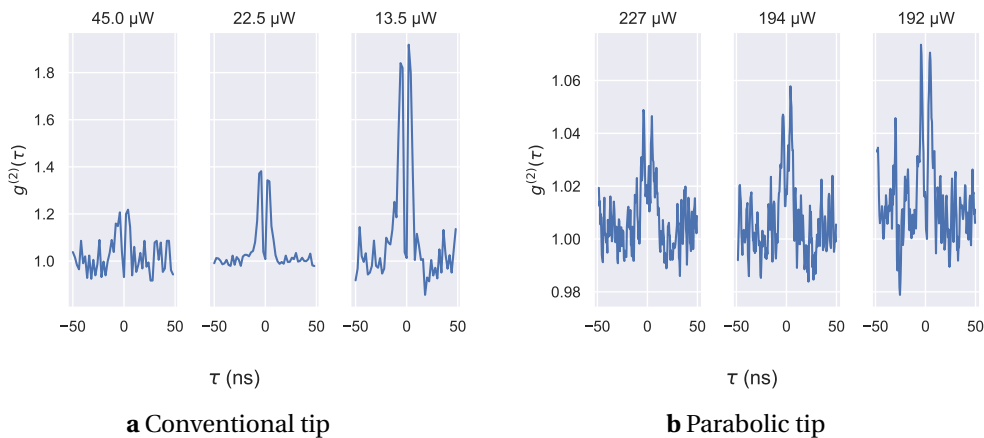


Fig. 6.6: Variation of a sharp $g^{(2)}(\tau)$ feature with narrow sidebands at vacuum ($\approx 10^{-6}$ mbar) with laser power on, **a** conventional tip and, **b** parabolic tip. The laser power is shown above the corresponding plot.

$$g^{(2)}(\tau) = 1 - \beta e^{-\gamma_1 \tau} + (\beta - 1) e^{-\gamma_2 \tau} \quad (6.5)$$

where,

$$\gamma_1 \approx k_{12} + k_{21} \quad \text{and} \quad \gamma_2 \approx k_{31} + \frac{k_{12}k_{23}}{k_{12} + k_{21}} \quad \text{and} \quad \beta \approx 1 + \frac{k_{12}k_{23}}{k_{31}(k_{12} + k_{21})} \quad (6.6)$$

The data in Fig. 6.5a data was fit to the second-order correlation function, and $g^{(2)}(\tau = 0)$ is extracted from the fit. The variation of $g^{(2)}(\tau = 0)$ with pressure is shown in Fig. 6.5b. Interestingly, the data appears to show an exponential increase in $g^{(2)}(0)$ with decreasing pressureⁱ. Note that points below 4.9×10^{-5} mbar are not well fit by the second-order correlation function and are therefore not shown.

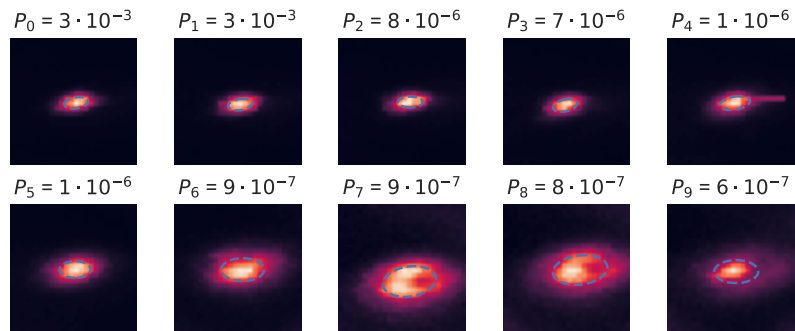
However, both NV^- and NV^0 are known to show photon anti-bunching behavior related to their three-level structure¹⁰¹. At sufficient vacuum, i. e. below 10^{-6} mbar, we observe a sharp $g^{(2)}(\tau)$ feature with narrow sidebands (Fig. 6.6). The feature is consistent across both conventional and parabolic tip geometry (Fig. 6.6a and Fig. 6.6b respectively), with the caveat that the feature is significantly weaker in the parabolic tip, and required $\approx 5x$ the laser power to resolve. Given that this feature only appears after a saturation in spectral behavior is observed, it is likely to be related to the NV^0 charge state. However, the second-order correlation sidebands observed here (≈ 15 ns) are shorter than previous observations (≈ 50 ns) for the NV^0 charge state¹⁰⁴, and the feature does not demonstrate a clear anti-bunching dip.

6.6 Confocal variation with pressure

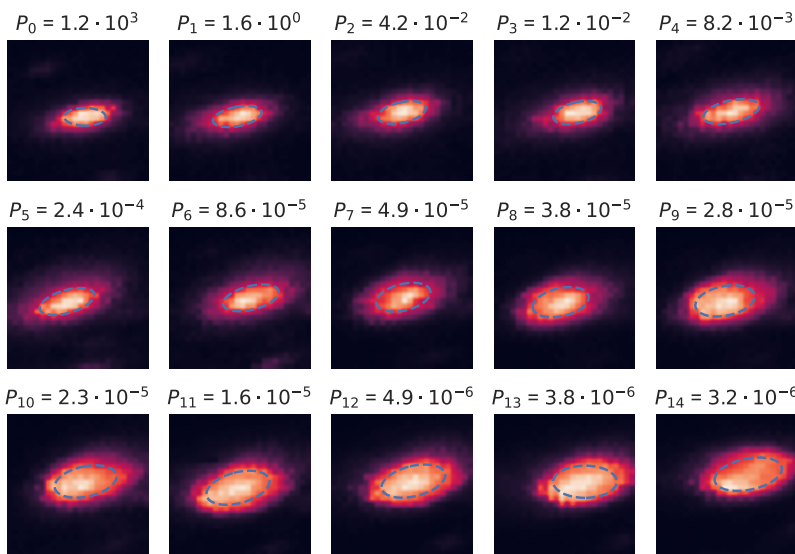
An interesting feature we observed over the course of the pressure variation measurements was the variation of the confocal images. We observe the confocal spot of the NV center increase in size with decreasing pressure. We were skeptical of this result initially, and assumed that it was an artifact of the objective lens induced by pressure, or even an artifact caused by the particular tip. However, we observe the same result across multiple tips (both parabolic and conventional geometry), and across two different objectives (both standard and vacuum compatible). This size variation is shown for a conventional tip in Fig. 6.7a and for a parabolic tip in Fig. 6.7b. Importantly, we note that the rest of the confocal scan i. e. the diamond plate did not show any size variation with pressure.

The confocal spots in Fig. 6.7a and Fig. 6.7b are fit with a 2-D Gaussian function, shown on the figure as dotted blue ellipses. From this we can extract a size metric using the ellipse perimeter. The variation of this perimeter is shown in Fig. 6.7c. Across all tips and objectives, we see a clear increase in the confocal size with decreasing pressure. The pressure at which the size

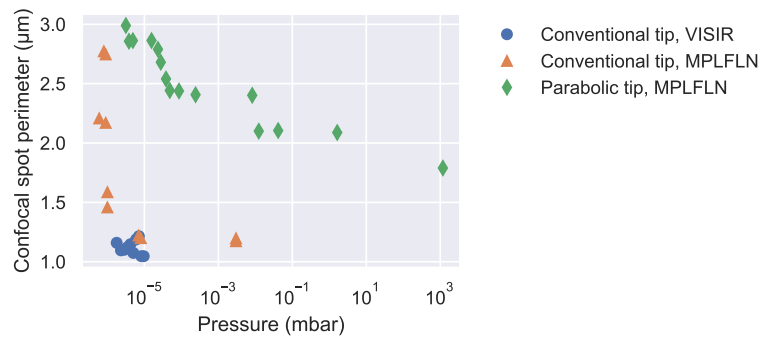
ⁱWe would stress that there is no obvious reason for exponential behavior, other than that it appears to model the observed data quite well.



a Conventional tip



b Parabolic tip



c Variation of NV confocal spot perimeter

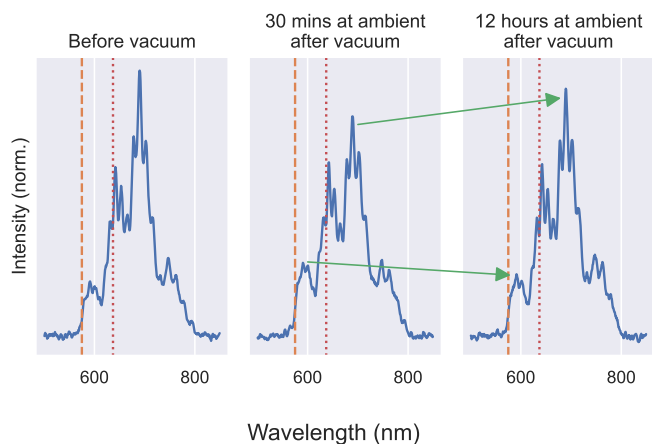
Fig. 6.7: Variation of NV confocal with pressure on, **a** conventional tip and, **b** parabolic tip. Pressure is shown above the corresponding plot in units mbar. Dashed blue line indicates a 2-D Gaussian fit to the data. **c** Variation of NV confocal perimeter with pressure. Data measured on conventional tips (both VISIR and MPLFLN objectives) and parabolic tips (MPLFLN objective).

changes rapidly is also consistent with the complete loss of the NV^- anti-bunching dip and enhancement of the NV^0 spectral signature.

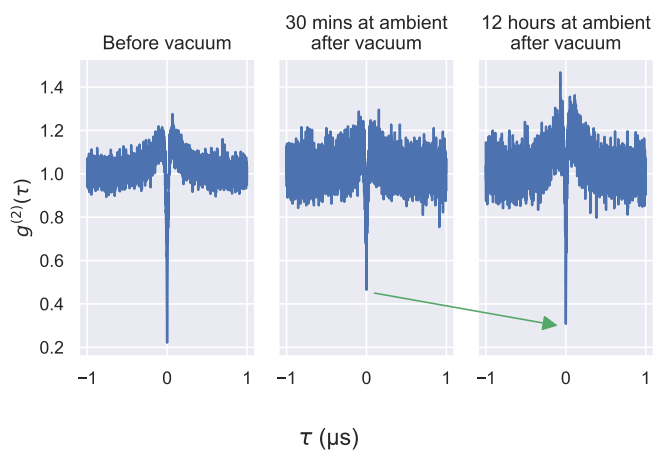
We do not, of course, believe that the size of the NV defect itself is changing as a function of pressure. However, since we are working with diamond nanopillars, it is conceivable that a modification in the way the NV emits photons between the NV^- and NV^0 charge states could couple differently to the waveguide modes of the nanopillar, which could potentially result in the observed size variation. To the extent of our knowledge, this has not been reported in literature prior to this work, and future theoretical simulations into this could help shed some light on the mechanism.

6.7 Recovery of NV^- post vacuum exposure

In all measured cases, the process of NV^- to NV^0 charge state conversion was reversible. To reverse the process, the system was brought back to ambient conditions and held there for several hours. We would like to stress that *no* recovery was observed by simply raising the pressure in the vacuum chamber. We only started to observe a recovery after bringing the chamber back to ambient conditions. The recovery process was gradual, and took approximately ≈ 12 h to complete. The recovery of the NV^- spectral signature is shown in Fig. 6.8a, and the recovery of the NV^- anti-bunching dip is shown in Fig. 6.8b. From the spectra, we can clearly see that over the course of the recovery, the NV^0 sidebands between 600 nm to 650 nm are being suppressed while the NV^- sidebands between 650 nm to 750 nm are being enhanced.



a NV⁻ spectral recovery



b NV⁻ autocorrelation recovery

Fig. 6.8: Measurements before the system was exposed to vacuum ($\approx 10^{-6}$ mbar), and recovery of NV⁻ at ambient conditions 30 min and 12 h post vacuum exposure. **a** Spectroscopic measurements, NV⁰ and NV⁻ ZPL is shown at 575 nm (dashed orange line) and 637 nm (dotted red line) respectively. Spectra are normalized to the total number of photons in the measurement window. **b** Autocorrelation measurements, showing $g^{(2)}(0) = 0.3$ post recovery.

7 Conclusion & Outlook

Over course of this thesis, we were able to achieve the main goals that we laid out at the beginning of the project. We motivated the use of the nitrogen vacancy center as an ideal single qubit magnetometer, and then used a single NV center to demonstrate electron paramagnetic resonance on an encapsulated nitrogen spin ($N@C_{60}$) using a single near-surface NV center in diamond at 4.7 K. Exploiting the strong magnetic dipolar interaction between the NV and endofullerene electronic spins, we demonstrated RF pulse controlled Rabi oscillations and measured spin-echos on the encapsulated spin.

The limitations of this “fixed” NV approach led us to design and construct an entirely new NV-SPM capable of operating from ambient pressure to ultra-high vacuum (10^{-9} mbar), from room temperature to cryogenic temperatures (4.7 K), and from zero-field to high vector magnetic field (1 T). In addition, the system is capable of generating nanosecond pulsed RF excitation up to 20 GHz, can perform confocal imaging and second-order photon correlation, can record real-time optical spectra, and features both active and passive damping to minimize vibrations. The system functionality is tied together with a custom built software package, which allows for advanced levels of measurement sequencing, control and analysis.

Using this NV-SPM, we performed nanoscale, all-optical relaxometry measurements on synthetic antiferromagnetic thin films at ambient conditions, and observe clear domain wall structures in good agreement with our magnetic force microscopy measurements on the same sample.

We then performed the first measurements examining the charge state behavior of the NV center in diamond tips as a function of vacuum. Using spectroscopic and second-order correlation measurements, we report a clear vacuum induced charge state transition from NV^- to NV^0 . We also observe anomalous effects related to the confocal “size” of the NV center when it undergoes this transition. Finally, we demonstrate that the vacuum induced transition to NV^0 is completely reversible in nature.

This work demonstrates the capabilities of our NV-SPM. It also details the challenges associated with constructing such a system. As is always the case in physics, the experimental

system is never truly complete, and there are many avenues for future work. We briefly discuss some of these avenues in the next section.

Future work

Setup upgrades

Cold tip/sample preparation The current tip/sample transfer arm operates at room temperature. This significantly limits the extent to which evaporated materials can be deposited on the tip/sample surface. This can be improved by replacing it with a liquid Helium cooled transfer arm. This will also permit an *in-situ* control of the diamond surface, which may prove critical to stabilizing the NV^- charge state under vacuum conditions.

Improved piezoelectric positioning The range of the piezoelectric stages in the system is highly limited and can be non-linear at certain points. This is likely due to a combination of loosening of the piezoelectric elements due to vibrations, and unbalanced strain applied on the piezoelectric stack over the normal course of operation. This can be improved by re-mounting, or even entirely replacing the piezoelectric elements after disassembling the measurement head.

Improved MW alignment and reduced piezoelectric strain Currently, we use a custom designed and home-built stage and holder. This shows excellent MW transmission, but adds additional strain on the piezoelectric stack (see the previous point) and is challenging to reproducibly align. A switch to a commercial stage and holder such as those manufactured by Ferrovac AG (RECOMCREC13 stage & SHOMECEC13 holder respectively), could significantly improve these aspects of the system performance.

Improved cryogen hold time The current hold time of the system could prove to be restrictive for longer measurement schemes. This can be improved by adding additional thermalization stages to the MW cabling along the cryostat. In addition, we observe that the tip/sample stages are a few Kelvin warmer than the cryostat baseplate. This can be significantly improved by connecting thick and flexible Copper braids between the stages and the cryostat baseplate.

Sensor and material platform improvements

Alternate defect centers in diamond The Silicon vacancy (SiV) center in diamond^{105,106} is a promising defect center in diamond for quantum sensing. It features a stronger zero-phonon line (ZPL) and a narrow spectral line width as compared to the NV center. Alternatively, both the Sulphur vacancy (SV) center in diamond^{107,108} and the Germanium vacancy (GeV) center in diamond^{109,110}, are promising defect centers due to their long spin coherence times and high magnetic field sensitivity. We do recognize, however, that only NV centers in diamond have currently been fabricated into scanning probe microscope tips.

Doped diamond tips NV^- charge state stabilization could also be performed by doping the diamond with electron donors, such as Phosphorous. Experimental evidence measured at ambient conditions on diamond membranes suggests that a significant improvement in NV phase coherence T_2 can be achieved using this method^{58,111}.

Alternate solid-state material platforms Silicon carbide (SiC) has been attracting attention in recent years as a material platform for quantum sensing due to its ability to host a variety of defect centers with useful quantum sensing properties¹¹²⁻¹¹⁴.

Interesting magnetic systems

Exotic magnetic structures Merons are the topological equivalent of half-skyrmions. Unlike AF skyrmions, merons do not exhibit deflected motion and have better size scaling properties¹¹⁵⁻¹¹⁷. In addition, they can be magnetically erased and regenerated by temperature cycling. Both these properties make them ideal candidates for use in spintronic devices. Currently merons in $\alpha - Fe_2O_3$ have been observed using X-ray Photoemission electron microscopy (PEEM)¹¹⁵. The NV center would be an ideal high-resolution, non-invasive sensor for studying the internal structure of merons.

EF-Tu proteins in bacterial cells The EF-Tu protein delivers tRNA to the ribosome¹¹⁸. The current understanding is that the protein is homogeneously distributed in the cell. However, EF-Tu has been observed to form self-organized filaments in vitro^{119,120}. This leaves several open questions – Is EF-Tu part of the bacterial cytoskeleton, and what is its impact on translation i.e. mRNA to protein conversion? The NV center at low-temperature would be an ideal non-invasive sensor to observe the distribution and structure of spin-labelled EF-Tu proteins in bacterial cells.

A Data Processing with Qudi-Hira-Analysis

The data was analyzed in Python 3.10 using the Qudi-Hira-Analysis package developed by the author over the course of the thesis. The analysis code is published in

D. Pinto, *Dineshpinto/qudi-hira-analysis: v1.0.0*, version v1.0.0, Zenodo, Feb. 4, 2023

Qudi-Hira-Analysis offers an abstracted high level interface, and provides a set of functions to automate data import, handling and analysis. It also aims to improve transparency and reproducibility in experimental data analysis. In an ideal scenario, two lines of code are sufficient to recreate all output data. It is also cross platform, and can be used on Windows, Linux and MacOS.

Python offers some very handy features like dataclasses, which are heavily used by this toolkit. Dataclasses offer a full OOP (object-oriented programming) experience while analyzing complex data sets. They provide a solid and transparent structure to the data to reduce errors arising from data fragmentation. This generally comes at a large performance cost, but this is (largely) sidestepped by lazy loading data and storing metadata instead wherever possible.

Qudi-Hira-Analysis can be installed from the Python Package Index, using the following command:

```
pip install qudi-hira-analysis
```

To use Qudi-Hira-Analysis, we first need to set up the `DataHandler` object (henceforth referred to as `dh`). The code for this is given in [Fig. A.1](#). We initialize it with:

- `data_folder` is the main folder where all the data is stored, it can be the direct path to the data, or composed of several sub-folders, each containing the data for a specific measurement
- `figure_folder` the path to the folder where the figures will be saved
- `measurement_folder` is the specific sub-folder in `data_folder` where the data for a specific measurement is stored. This argument is optional, and can be left out if the data is stored in the `data_folder` directly.

Appendix A. Data Processing with Qudi-Hira-Analysis

```
# Import libraries to handle filepaths and plotting
from pathlib import Path
import matplotlib.pyplot as plt
import seaborn as sns

from qudi_hira_analysis import DataHandler

dh = DataHandler(
    data_folder=Path("C:\\", "Data"),
    figure_folder=Path("C:\\", "QudiHiraAnalysis"),
    measurement_folder=Path("20230101_NV1")
)
```

Fig. A.1: Setting up the DataHandler object.

To load a specific set of measurements from the data folder, we use the `load_measurements()` method. The code for this is given in [Fig. A.2](#). The method takes the following required arguments:

- `measurement_str` is the string that is used to identify the measurement. It is used to filter the data files in the `data_folder` and `measurement_folder` (if specified)

Optional arguments are:

- `qudi` is a boolean. If `True`, the data is assumed to be in the format used by Qudi (default: `True`)
- `pulsed` is a boolean. If `True`, the data is assumed to be in the format used by Qudi for pulsed measurements (default: `False`)
- `extension` is the extension of the data files (default: `".dat"`)

The `load_measurements()` method returns a dictionary containing the measurement data filtered by `measurement_str`.

The dictionary keys are measurement timestamps in “(year)(month)(day)-(hour)(minute)-(second)” format. The dictionary values are `MeasurementDataclass` objects whose schema is shown visually in [Fig. A.3a](#).

The visual structure of the toolkit is shown in [Fig. A.3b](#). It largely consists of three portions:

- `IOHandler` handles all IO operations i. e. reading specific measurement data files and saving figures
- `DataLoader` maps IO functions in `IOHandler` to measurement data types
- `AnalysisLogic` contains automated fitting routines supporting all common fitting functions using in NV magnetometry

```

corrs = dh.load_measurements("autocorrelation")

fig, ax = plt.subplots()

for autocorr in corrs.values():
    # Get laser power by parsing filename
    laser_pow = autocorr.get_param_from_filename(unit="uW")

    # Use ns instead of ps
    autocorr.data["Time (ns)"] = autocorr.data["Time (ps)"] / 1e3

    # Plot the data
    sns.lineplot(
        data=autocorr.data,
        x="Time (ns)",
        y="g2norm (t)",
        label=f"{laser_pow:.2f} uW",
        ax=ax
    )

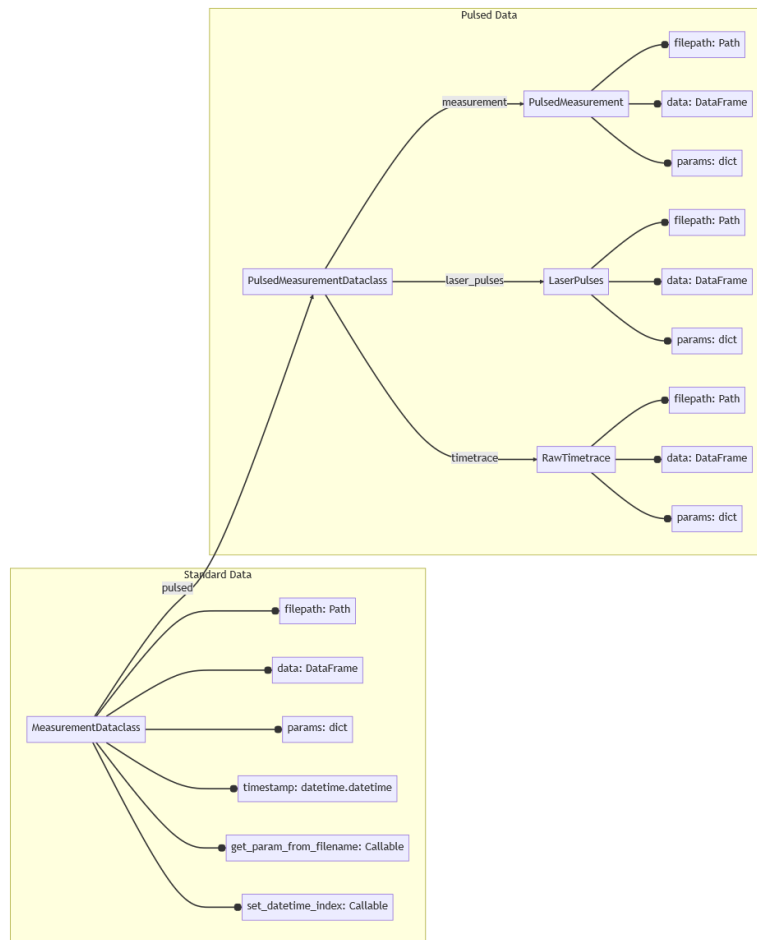
    # Fit the data using the antibunching function
    fit_x, fit_y, result = dh.fit(
        x="Time (ns)",
        y="g2norm (t)",
        data=autocorr.data,
        fit_function=dh.fit_function.antibunching
    )

    # Plot the fit
    sns.lineplot(x=fit_x, y=fit_y, ax=ax)

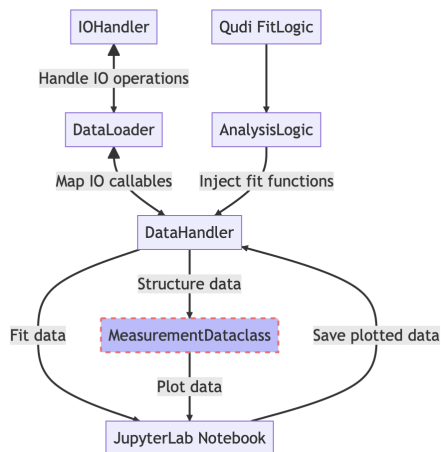
# Save the figure to the figure folder specified earlier
# By default, saves data in .png, .jpg, .pdf and .svg formats
dh.save_figures("autocorrelation", fig=fig)

```

Fig. A.2: Example usage importing all autocorrelation data in a measurement set, labeling the data with the laser power, fitting it to the $g^{(2)}$ -correlation function described in [Appendix A.5](#), and saving the resulting plot.



a MeasurementDataclass schematic



b Qudi-Hira-Analysis schematic

Fig. A.3: Schematic diagrams of the **a** MeasurementDataclass and **b** Qudi-Hira-Analysis toolkit.

A.1 Spin state computation

```
# Use T1 measurements as an example, any pulsed measurement will work
t1s = dh.load_measurement("t1", pulsed=True)

for t1 in t1s.values():
    raw_signal_data = t1.pulsed.laser_pulses.data
    # Extract spin state from raw data
    signal_data, error_data = dh.analyse_mean_norm(
        raw_signal_data,
        signal_start=100e-9,
        signal_end=400e-9,
        norm_start=2e-6,
        norm_end=3e-6
    )
```

The position of the laser pulse is determined from the profile of the time-tagged counts. A choice of time step dt , integration window width T , and the shifts of the 1st and 2nd integration windows relative to laser pulse t_1 and t_2 . The spin state s for n photons is calculated using Eq. A.1.

$$n_{\text{state}} = \sum_{t=t_1}^{t_1+T} n_t; \quad n_{\text{ref}} = \sum_{t=t_2}^{t_2+T} n_t; \quad s = \frac{n_{\text{state}}}{n_{\text{ref}}} \bar{n}_{\text{ref}} \quad (\text{A.1})$$

A.2 Spectroscopy analysis

```
odmrs = dh.load_measurement("odmr", pulsed=True)

for odmr in odmrs.values():
    # Fit the data to a double Lorentzian
    fit_x, fit_y, result = dh.fit(
        x="Controlled variable (Hz)",
        y="Signal",
        data=odmr.data,
        fit_function=dh.fit_function.lorentziandouble,
    )
    sns.lineplot(x=fit_x, y=fit_y, label=odmr.filename)
    # Generate a report of the fit (optimal parameters, errors, etc.)
    print(result.fit_report())
```

The spin-state computation result is baseline corrected using asymmetric least squares smoothing with an asymmetry (weighting of positive residuals) of 0.9 and a smoothness (2nd derivative constraint) of 10^6 . Spectroscopic peaks positions are determined by iterative runs of the `peakutils` `peakfinder`. Each peak is given its own Lorentzian model using `lmfit`. A constant model is assumed to correct for any offset. The fitting for N Lorentzians (Eq. A.2) is performed using the Powell minimizer. Standard deviation of the background is calculated at points having a vanishing spline 2nd derivative. signal-to-noise ratio (SNR) ratio is calculated from the peak height and the noise background.

$$f(x; c, A_i, \mu_i, \sigma_i) = c + \sum_{i=1}^N \left[\frac{A_i}{\pi} \frac{\sigma_i}{(x - \mu_i)^2 + \sigma_i^2} \right] \quad (\text{A.2})$$

A.3 Oscillation analysis

```
rabis = dh.load_measurement("rabi", pulsed=True)

for rabi in rabis.values():
    # Fit the data to an exponentially decaying sinusoid
    fit_x, fit_y, result = dh.fit(
        x="Controlled variable (s)",
        y="Signal",
        data=rabi.data,
        fit_function=dh.fit_function.sineexponentialdecay,
    )
    sns.lineplot(x=fit_x, y=fit_y, label=rabi.filename)
```

The parameters of the fit are estimated – amplitude is guessed from standard deviation ($\sqrt{2}\sigma$), frequency from real fast-fourier transform of the signal and decay from the change in standard deviation. These parameters are then optimized by the scipy curve fitting routine to an exponentially decaying sinusoid (Eq. A.3).

$$f(x; c, A, d, \omega, \phi) = c + A \exp\left(-\frac{x}{d}\right) \sin(\omega x + \phi) \quad (\text{A.3})$$

A.4 Hahn-Echo analysis

```
echos = dh.load_measurement("hahn", pulsed=True)

for echo in echos.values():
    # Fit the data to a stretched exponentially decaying sinusoid
    fit_x, fit_y, result = dh.fit(
        x="Controlled variable (s)",
        y="Signal",
        data=echo.data,
        fit_function=dh.fit_function.sinestretchedexponentialdecay,
    )
    sns.lineplot(x=fit_x, y=fit_y, label=echo.filename)
```

The Hahn-Echo decay and revivals are given by Eq. A.4.

$$f(x; c, A, T_2, \alpha, \omega, \phi) = c + A \exp\left[-\left(\frac{x}{T_2}\right)^\alpha\right] \langle \cos^2(\omega x + \phi) \rangle \quad (\text{A.4})$$

A.5 Second order correlation analysis

Example code for the analysis of the second order correlation function is given in Fig. A.2. The theory of the three level structure of the NV center and its relation to the second order correlation function is described in Berthel et al. [104]. The excitation rate k_{12} , the spontaneous emission k_{21} , and the two parameters k_{23} and k_{31} of the additional decay path involving shelving. The relation between the transition rates and the second order correlation is given in Eq. A.5:

$$g^{(2)}(\tau) = 1 - \beta e^{-\gamma_1 \tau} + (\beta - 1) e^{-\gamma_2 \tau} \quad (\text{A.5})$$

where,

$$\gamma_1 \approx k_{12} + k_{21} \quad (\text{A.6})$$

$$\gamma_2 \approx k_{31} + \frac{k_{12} k_{23}}{k_{12} + k_{21}} \quad (\text{A.7})$$

$$\beta \approx 1 + \frac{k_{12} k_{23}}{k_{31} (k_{12} + k_{21})} \quad (\text{A.8})$$

The measured $g^{(2)}(\tau)$ data is fit to Eq. A.5 yielding $\beta, \gamma_1, \gamma_2$. The k_{ij} coefficients can be extracted using,

$$k_{21} = \gamma_1 - k_{12} \quad (\text{A.9})$$

$$k_{31} = \frac{\gamma_2}{\beta} \quad (\text{A.10})$$

$$k_{23} = \frac{\gamma_1 \gamma_2 (\beta - 1)}{\beta k_{12}} \quad (\text{A.11})$$

Under the assumption of a constant k_{21} , its value can be extracted by extrapolating a linear fit between excitation power P_{exc} and γ_1 at $P_{exc} = 0$ i. e. $\gamma_1(P_{exc} = 0) = k_{21}$. Previous works result in $k_{21} \approx 21.7$ ns for the NV⁻ charge state^{122,123}.

A.6 Error estimation

The largest contributor to the experimental noise is from photon shot noise. Photon shot noise is a spatially and temporally random phenomenon described by Bose-Einstein statistics. Given N photons, Eq. A.12 is a general form of photonic shot noise, in the limit where the photon energy is much smaller than thermal energy $h\nu \ll k_B T$ it can be approximated to Eq. A.13.

Appendix A. Data Processing with Qudi-Hira-Analysis

$$\sigma_p(N) = N \left(\frac{\beta}{\beta - 1} \right); \quad \beta = \exp \left(\frac{h\nu}{k_B T} \right) \quad (\text{A.12})$$

$$\sigma_p(N) \approx \sqrt{N} \quad (\text{A.13})$$

This error is then propagated using standard error propagation techniques. Taking the photon counts from [Eq. A.1](#) and using $\delta n = \sqrt{n}$ we get [Eq. A.14](#).

$$\frac{\delta s}{s} = \sqrt{\left(\frac{\delta n_{\text{state}}}{n_{\text{state}}} \right)^2 + \left(\frac{\delta n_{\text{ref}}}{n_{\text{ref}}} \right)^2} = \sqrt{\frac{1}{n_{\text{state}}} + \frac{1}{n_{\text{ref}}}} \quad (\text{A.14})$$

$$\delta s = \left(\frac{n_{\text{state}}}{n_{\text{ref}}} \bar{n}_{\text{ref}} \right) \sqrt{\frac{1}{n_{\text{state}}} + \frac{1}{n_{\text{ref}}}} \quad (\text{A.15})$$

B Perturbation theory & coupling strength

When considering the above stated Hamiltonian one would expect a splitting of the N@C₆₀ single molecule spectral lines with a total distance of $2a$ between the center of the $M_I = -1$ and the $M_I = +1$ peaks. This can be seen utilizing a second order perturbation approach.

electron spin: $S = 3/2$

nuclear spin: $I = 1$

external magnetic field: $\hat{B} = \begin{pmatrix} B_x \\ B_y \\ B_z \end{pmatrix} = \begin{pmatrix} 0 \text{ mT} \\ 0 \text{ mT} \\ 9.697 \text{ mT} \end{pmatrix}$

$$\begin{aligned} \frac{\mathcal{H}}{h} &= \frac{\mathcal{H}_{EZ}}{h} + \frac{\mathcal{H}_{ZF}}{h} + \frac{\mathcal{H}_{HF}}{h} \\ &= \frac{\mu_B}{h} \hat{B}^T \hat{g} \hat{S} + \hat{S}^T \hat{D} \hat{S} + \hat{S}^T \hat{A} \hat{I} \\ &= \frac{g\mu_B}{h} (B_x \hat{S}_x + B_y \hat{S}_y + B_z \hat{S}_z) + \frac{D}{3} (2\hat{S}_z^2 - \hat{S}_y^2 - \hat{S}_x^2) + a(\hat{S}_x \hat{I}_x + \hat{S}_y \hat{I}_y + \hat{S}_z \hat{I}_z) \end{aligned}$$

We assume that the Electron-Zeeman interaction \mathcal{H}_{EZ} represents the unperturbed system's Hamiltonian H_0 whereas Hyperfine \mathcal{H}_{HF} and Zero-Field \mathcal{H}_{ZF} interactions are considered to be the perturbation \mathcal{H}_1 .

$$\mathcal{H} = \mathcal{H}_0 + v_1 = \mathcal{H}_{EZ} + (\mathcal{H}_{HF} + \mathcal{H}_{ZF})$$

The line broadening is Fourier limited by the experimental pulse width of 100 ns, giving a line broadening of $1/(\pi \times 100\text{ns}) \approx 3.3\text{MHz}$ ¹²⁴. This is slightly smaller than what we see in the experiment ($\approx 4\text{MHz}$), indicating that the weak interaction of the spin-bath with the endofullerene is moderately lowering its T_2^* (leading to an additional Gaussian broadening $\propto 1/T_2^*$ ^{125,126}).

B.1 Dependence on zero-field axis

In an ensemble, all axial orientations of the molecule average out. This does not happen at the single spin level. Therefore one might consider an angular dependence when computing the zero-field splitting terms for the single molecule. The angle ϕ between the magnetic field and the orientation of the molecular frame is introduced. The zero-field splitting tensor in the molecular frame is given by,

$$\hat{D}_{mol} = \begin{pmatrix} -\frac{1}{3}D & 0 & 0 \\ 0 & -\frac{1}{3}D & 0 \\ 0 & 0 & \frac{2}{3}D \end{pmatrix}$$

This now has to be rotated into the lab-frame with a z -aligned magnetic field. For this a rotation around the y -axis over the angle ϕ given by $\hat{R}_y(\phi) \hat{D}_{mol} \hat{R}_y^T(\phi)$ yields the splitting tensor in the lab-frame,

$$\hat{D}_{lab} = \begin{pmatrix} D(\cos^2(\phi) - \frac{1}{3}) & 0 & \frac{1}{2}D \sin(2\phi) \\ 0 & -\frac{1}{3}D & 0 \\ \frac{1}{2}D \sin(2\phi) & 0 & D(\sin^2(\phi) - \frac{1}{3}) \end{pmatrix}$$

leading to a zero-field splitting Hamiltonian of the form,

$$\frac{\mathcal{H}_{ZF}}{h} = \frac{1}{6} D (\hat{S}_x^2 + \hat{S}_z^2 - 2\hat{S}_y^2) + \frac{1}{2} D (\hat{S}_z \hat{S}_x + \hat{S}_x \hat{S}_z) \sin(2\phi) + \frac{1}{2} D (\hat{S}_z^2 - \hat{S}_x^2) \cos(2\phi)$$

This, as well as an EasySpin simulation for different angles shows that for all angles ϕ the zero-field splitting leads to an almost symmetrical distance between the central transition-peaks (solid lines) for each nuclear quantum number M_I . Hence, angular dependencies in the zero-field splitting terms do not lead to an effective shift of the peak-positions measurable at a considerable line-width. The total distance between the $M_I = -1$ and the $M_I = +1$ central peaks remains $2a$, which can also be seen from the calculated energy corrections.

B.2 Dependence on anisotropic hyperfine interaction

Up to this point the total width of the spectrum is given by $2a$. Ensemble EPR measures $2a = 32$ MHz for N@C₆₀. However, our single spin EPR results measure $2a = 38$ MHz. Admitting the possibility of a strong deformation of the C₆₀ cage we can consider an anisotropic hyperfine interaction. The anisotropy parameter Δ is introduced so that the interaction tensor \hat{A} becomes,

$$\hat{A} = \begin{pmatrix} A_x & 0 & 0 \\ 0 & A_y & 0 \\ 0 & 0 & A_z \end{pmatrix} = \begin{pmatrix} a - \frac{\Delta}{2} & 0 & 0 \\ 0 & a - \frac{\Delta}{2} & 0 \\ 0 & 0 & a + \Delta \end{pmatrix}$$

The hyperfine interaction Hamiltonian thus reads

$$\begin{aligned} \frac{\mathcal{H}_{\text{HF}}}{h} &= \hat{S}^T \hat{A} \hat{I} = A_x \hat{S}_x \hat{I}_x + A_y \hat{S}_y \hat{I}_y + A_z \hat{S}_z \hat{I}_z \\ &= \left(a - \frac{\Delta}{2} \right) (\hat{S}_x \hat{I}_x + \hat{S}_y \hat{I}_y) + (a + \Delta) \hat{S}_z \hat{I}_z \end{aligned}$$

Due to this anisotropy the total distance between the $M_I = -1$ and the $M_I = +1$ central peaks now becomes $2a + 2\Delta$. This result can also be obtained from the second order perturbation calculation when using the above stated hyperfine Hamiltonian. When also including an angular dependence in the hyperfine interaction (which should be the same one as for the zero field interaction) the total splitting distance can be found to be $2a + \frac{1}{2}\Delta + \frac{3}{2}\Delta \cos(2\phi)$.

B.3 Enhanced hyperfine & zero-field interactions

Simulating a single N@C₆₀ molecule with a g-factor of $g_1 = 2.00204$ and a additional spin-1/2 bath with a g-factor of $g_2 = 2.03$, which may originate from drop coating the N@C₆₀ solution. The g-factor of this second spin species, however, strongly differs from the previously considered C₆₀ radical. The blue line shows the combined spectrum. Considering a hyperfine constant of $A = 19$ MHz for the spin-3/2 species instead of the usual 15.85 MHz for N@C₆₀, the combined spectrum fits the measured data quite nicely even without an anisotropic hyperfine interaction ($\Delta A = 0$) or including an additional angular dependence in the zero-field splitting interaction ($\phi = 0$).

The strong deviation of the N@C₆₀ hyperfine parameter could result from the hyperfine constant, possibly being quite different when the molecule is located on the diamond surface as compared to its typical values inside the bulk. This change would imply a decrease of the fullerene cage cavity. Considering all the information gathered from these experiments it however remains unclear how this specific decrease is caused, and requires follow up experiments to better understand the chemical effects of the diamond surface.

B.4 Non-thermal spin distributions

The splitting of hyperfine components in a typical ensemble X-band EPR experiment (9 - 10 GHz) is typically symmetric and can hence only explain the increase of the total spectrum width, not the asymmetry. In the low-field situation here (≈ 260 MHz), the spectrum may become slightly asymmetric due to a combination of the zfi and second-order hfi terms. The maximum expected downshift would however amount to $A^2/2g\mu_B B_z \approx 0.5$ MHz under

the present experimental conditions. The downshift of the lowest-energy transition can be rationalized by considering a possible non-thermal population that favors the minimal angular momentum state of N@C₆₀, i.e. $|m_S, m_I\rangle = |-3/2, -1\rangle$. This would favor the $m_S = -3/2$ to $m_S = -1/2$ transition for $m_I = -1$ and hence explain the downshift. A possible driving mechanism could be the frequent inter-system-crossing events of the NV center itself, which happen in the laser polarization intervals whenever the (electronically excited) NV $| -1 \rangle$ state crosses over to the singlet manifold. This acts as a “drain” for angular momentum in the environment. A detailed picture of the exact sequence of intermediate steps leading to a polarization of the N@C₆₀ molecule and related quantitative analysis is beyond the scope of this work. We note that the population redistribution may occur on a long time scale since the spin relaxation times of endofullerenes at 4.7 K are on the order of seconds (T_{1e}) and even hours (T_{1n})³⁴. Each iteration of the measurement sequence is on the order of 5 μ s, over time there may well be a detectable accumulation of tiny imbalances of the coupling to the environment.

B.5 Coupling strength & distance

Our measurement scheme for the NV-bath spin coupling strength is similar to the more generalized spin-echo double resonance (SEDOR) proposed in de Lange et al. [127]. Their scheme probes the NV dephasing induced by a group of bath spins, which refocusing all the remaining groups of spin baths. This measurement sequence has been used to quantify the contribution from the nuclear and electron (P1 centers) spin-baths to the total dephasing of the NV spin^{127,128} and the external spins⁴⁷. In the employed DEER pulse-sequence we refocus only the electron spins, which could include both the known spins from the N@C₆₀ and any unknown electron spin-bath. Thus, the π -pulse on the electronic spin-bath also refocuses the static noise experienced by these external spins caused by their local environments, thereby having a two-fold effect on NV spin decoherence. The NV spin-echo signal displays a Gaussian envelope decay with a decoherence time of $T_2 \simeq 4.3\mu$ s when all the decoherence channels are refocused. On the other hand, when some of the dephasing channels are refocused, we find the decay is well-fitted for Eq. B.1.

$$P \approx \exp\left(\frac{-t}{\tau}\right) \cos\left(\frac{gt}{2}\right) \quad (\text{B.1})$$

where $\tau = 3.17\mu$ s is the coherence decay of the NV-spin determined by the magnetic environment that is not refocused due to the π -pulse performed at the frequency $\omega = 272$ MHz. Further, this decay is modulated by the dominant coherent coupling of the external spin at the coupling rate g . A simple and well used model to explain such a behavior is determined by the Hamiltonian evolution and the decoherence of the NV spin. For the Hamiltonian we consider the dominant contribution of the dipolar interaction along the field direction (z), given by,

$$\mathcal{H} = S^z \left(\frac{g}{2} \sigma_L^z + \sum_k \frac{F_k}{2} \sigma_k^z \right) \quad (\text{B.2})$$

where σ are Pauli matrices. Here g is coupling to the target electron spin of the spin-label, and F_k are the couplings to the an unknown electron spin-bath. Further, we switch on a Markovian decoherence channel for the NV spin due to its magnetic environment, characterized by the decay constant $1/\tau$. In the case when $F_k = 0$, solving the rate equation with the characteristic decay and coherent coupling to a single electron spin with coupling g , we arrive at the same fit formula obtained above.

The best fit for the data indicates that there is a slight discrepancy between the decay constants obtained with and without the π -pulse i.e., $\tau \neq T_2$. Using $\tau = T_2$ immediately yields a high coupling value for $g \simeq 0.4$ MHz instead of $g \simeq 0.28$ MHz. This could immediately hint towards the presence of additional electron spin-bath (third group), and whose effect was not refocused during the DEER pulse sequence. Including these additional electron spins and re-deriving the relation for the DEER signal⁴⁹ we obtain Eq. B.3.

$$P = \exp\left(\frac{-t}{\tau}\right) \cos\left(\frac{gt}{2}\right) \Pi_k \cos\left(\frac{F_k}{2}\right) \quad (\text{B.3})$$

where F_k are the coupling of the NV to additional electron spins. In including these third group of electron spins with couplings F_k to explain this discrepancy, we find ambiguities as a large number of possible combinations of the values of F_k could find a better fit for the decay of DEER signal. Thus, estimating the unknown number in the additional electronic spin-bath and their coupling distributions is beyond the scope of the current work. We instead give here a qualitative error in estimating the coupling strength from the simple fit-formula, given above which is for example including upto four additional spins would increase our uncertainty in the predicting the coupling as $0.22 \text{ MHz} < g < 0.40 \text{ MHz}$. As the fitted coupling values to these additional spins are in the same order one could assume the presence of an unknown electronic spin-bath close to the surface that also accounts for the observed asymmetry in the DEER spectrum. As the statistical probability of more than one N@C₆₀ spin within the sensing volume is extremely low ($\approx 0.2\%$), we find that including a single or a few electron spins do not contradict our distance measurements obtained in the ideal case. We also note that any direct dipolar coupling between the N@C₆₀ electron spin and electron spin-bath was neglected. Including them would lead an enhancement in the $T_{1\rho}$ of the spins, i.e., an additional equilibration channel for the target spin. As all of them are default in a fully-mixed state, and the Hamiltonian dynamics does not lead to any polarization, these dissipative channels are less effective.

C Setup Components

C.1 Nano-positioning stage

Component	Manufacturer	Part number
(x, y) positioner (x2)	Attocube	ANPx101/RES/LT/UHV
z positioner (x2)	Attocube	ANPz101/RES/LT/UHV
θ_x positioner	Attocube	ANGt101/RES/LT/UHV
θ_y positioner	Attocube	ANGp101/RES/LT/UHV
(x, y, z) scanner	Attocube	ANS100xyzstd/LT/UHV
Controller 1a (x, y, z)	Attocube	ANC 350
Controller 1b (θ_x, θ_y)	Attocube	ANC 300
Controller 2 ($x, y, z, \theta_x, \theta_y$)	Nanonis	HVS4 + PMD4
Controller 2b (x, y, z)	Nanonis	HVS4 + HVA4 + SC4

C.2 Tip/sample stage

Component	Manufacturer	Part number
MW socket (x2)	SV Microwave	SF1132-6067
MW plug (x2)	SV Microwave	1132-4005
Crimp socket (x4)	Allectra	Allectra 212-PINF-25-S
Solder plugs (x6)	Fischer Elektronik	PK 1 G
PCB MW connector (x2)	Rosenberger	18S101-40ML5
SMP-M to SMA cable (x2)	Teledyne	Stormflex 047
SMP-M cable (x2)	Amphenol RF	095-725-111-030
Wobble-stick 1	VAb	MDWS-ZO 350
Wobble-stick 2	VAb	STWS 150
Transfer arm	VAb	MDS 40-400

C.3 Atomic force microscope

Component	Manufacturer	Part number
Preamplifier IC	Analog Devices	AD8512
Compensation IC	Analog Devices	AD633AR
Secondary amplifier (opt.)	Femto	DLPVA-100-BLN-S
Low-pass electrical filter	Thorlabs	EF-124
High-pass electrical filter (opt.)	Thorlabs	EF-123
PLL controller	Nanonis	OC4

C.4 Ultra high vacuum

Component	Manufacturer	Part number
Diaphragm pump	Pfeiffer Vacuum	MVP 070-3
Backing turbopump	Pfeiffer Vacuum	HiPace 80 (+ TC 110, DCU 110)
Pirani gauge	Pfeiffer Vacuum	TPR 280
Main turbopumps (2x)	Pfeiffer Vacuum	HiPace 300 H (+ TC 400, DCU 310)
Ion-getter pump	NEXTorr	D300-5 (+ NIOPS-03)
Cold cathode gauge (2x)	Pfeiffer Vacuum	IKR 270
Gauge monitor	Pfeiffer Vacuum	TPG 366
Bayerd-Alpert gauge	Arun Microelectronics	AIG17G (+ NGC2)
Pneumatic gate valve (2x)	VAT	Series 10.8 DN63-200
Manual gate valve	VAT	Series 10.8 DN63-200

C.5 Low temperature

Component	Manufacturer	Part number
Helium depth indicator	Twickenham	HDI
Negative T-coefficient sensor	Lakeshore Cryotronics	CX-1070-SD
Silicon diode sensor	Lakeshore Cryotronics	DT-470-SD
Sensor monitor	Lakeshore Cryotronics	Model 218

C.6 Vector magnet

Component	Manufacturer	Part number
Magnet controller (x3)	Lakeshore	Model 625
Positive T-coefficient sensor (x3)	Lakeshore Cryotronics	PT-102
Negative T-coefficient sensor	Lakeshore Cryotronics	CX-1070-SD

C.7 Confocal microscope

Index	Component	Manufacturer	Part number
1	Diode laser	Toptica	iBEAM-SMART-515-S
2	Fiber collimator	Thorlabs	F110APC-532
3	Laser line filter	Thorlabs	FL514.4-10
4	Continuously variable ND filter	Thorlabs	NDC-50C-2M-A
5	Linear polarizer	Thorlabs	LPVISA050-MP2
6	Beamsplitter cube (10:90)	Thorlabs	BS025
7	Photodiode power sensor + console	Thorlabs	S130C + PM100D
8	Dichroic laser beam combiner	Newport	DCM13
9	Dielectric mirror	Newport	10Q20BB.1
10	Beamsplitter cube (50:50)	Thorlabs	BS013
11	Tip/Tilt piezo platform	PI	S-330.8SH
12	Tip/Tilt controller	PI	E-727
13	Semi-Apochromat objective	Olympus	MPLFLN100x
14	CMOS sensor	Thorlabs	CS165CU
15	Plano-convex lens	Newport	KPX076AR.14
16	Pinhole	Thorlabs	P75D
17	Plano-convex lens	Newport	KPX082AR.14
18	Longpass filter 1	Thorlabs	FELH0550
	Longpass filter 2	Thorlabs	FELH0650
	Shortpass filter	Thorlabs	FESH0800
19	Beamsplitter cube (50:50)	Thorlabs	BS013
20	Photon counting module (2x)	Excelitas	SPCM-AQRH-WX
21	Time-to-digital converter	Swabian	Timetagger 20
		Instruments	
22	Dielectric mirror	Newport	10Q20BB.1
23	Dielectric mirror	Thorlabs	BB1-E02
24	Piezo nanopositioner	PI	P-733.3CD XYZ
25	Piezo controller	PI	E-725
26	Semi-Apochromat objective	Attocube	LT-APO/VISIR/0.82
27	Dielectric mirror	Thorlabs	BB1-E02
28	Spectrometer	OceanInsight	QE Pro

C.8 Pulsed microwave

Component	Manufacturer	Part number
Arbitrary waveform generator	Spectrum	DN2.663-04
Microwave signal generator	Rohde & Schwarz	SMF100A (+ B122, B32, K3)
Microwave power amplifier	Spanawave	GT-1000B
Cryogenic cables	Teledyne	StormFlex 047
Solid state switch	American Microwave	SW-2184-1
Bias tee	Mini-Circuits	ZFBT-6GW+
High-pass filter	Mini-Circuits	SHP-1000+
SMA Bias Tee	Pulsar	BT-29-400S
Pulse amplifier	Mini Circuits	ZPUL-30P+
Vector network analyzer	Rohde & Schwarz	ZVL6

C.9 Communication protocols

Component	Manufacturer	Communication Protocol
Arbitrary waveform generator	Spectrum	Ethernet
Microwave signal generator	Rohde & Schwarz	Ethernet
Pressure gauge monitor	Pfeiffer Vacuum	RS232 (virtual)
Sensor monitor	Lakeshore	Ethernet
Piezo controller	PI	Ethernet
Tip/Tilt controller	PI	Ethernet
Magnet controller (x3)	Lakeshore	RS232
Diode laser	Toptica	RS232
Helium depth indicator	Twickenham	RS232
Time-to-digital converter	Swabian Instruments	USB3.0
LWD camera	Dino-Lite	USB3.0
Lightfield camera	Dino-Lite	USB2.0
Controller 1	Attocube	USB3.0
Controller 2	Nanonis	Ethernet

Bibliography

- ¹F. Jelezko and J. Wrachtrup, “Single defect centres in diamond: A review”, *physica status solidi (a)* **203**, 3207–3225 (2006).
- ²a. systems AG, *Session 1: Magnetic Imaging Conference*, attocube systems AG, <https://app.livestorm.co/p/ed6e7298-9c9f-4344-a861-936952cf3958>.
- ³M. V. G. Dutt et al., “Quantum Register Based on Individual Electronic and Nuclear Spin Qubits in Diamond”, *Science* **316**, 1312–1316 (2007).
- ⁴N. Zhao et al., “Sensing single remote nuclear spins”, *Nature Nanotechnology* **7**, 657–662 (2012).
- ⁵T. Wolf et al., “Subpicotesla Diamond Magnetometry”, *Physical Review X* **5**, 041001 (2015).
- ⁶B. Grotz et al., “Sensing external spins with nitrogen-vacancy diamond”, *New Journal of Physics* **13**, 055004 (2011).
- ⁷C. L. Degen, F. Reinhard, and P. Cappellaro, “Quantum sensing”, *Reviews of Modern Physics* **89**, 035002 (2017).
- ⁸G. Balasubramanian et al., “Nanoscale imaging magnetometry with diamond spins under ambient conditions”, *Nature* **455**, 648–651 (2008).
- ⁹S. A. Momenzadeh et al., “Nanoengineered Diamond Waveguide as a Robust Bright Platform for Nanomagnetometry Using Shallow Nitrogen Vacancy Centers”, *Nano Letters* **15**, 165–169 (2015).
- ¹⁰L. Garbini, *New Nature Communications paper on nanoscale magnetic features in van der Waals magnets using Qnami QuantileverMX probes*, Qnami, (Apr. 21, 2021) <https://qnami.ch/new-nature-communications-paper-on-nanoscale-magnetic-features-in-van-der-waals-magnets-using-qnami-quantilevermx-probes/>.
- ¹¹D. P. DiVincenzo, “The Physical Implementation of Quantum Computation”, *Fortschritte der Physik* **48**, 771–783 (2000).
- ¹²J. H. N. Loubser, W. P. van Ryneveld, and L. du Preez, “Exchange interaction effects in the E.S.R. spectrum of substitutional nitrogen in diamond”, *Solid State Communications* **3**, 307–309 (1965).
- ¹³A. Lenef and S. C. Rand, “Electronic structure of the N-V center in diamond: Theory”, *Physical Review B* **53**, 13441–13455 (1996).
- ¹⁴J. Maze et al., “Properties of nitrogen-vacancy centers in diamond: group theoretic approach”, *New Journal of Physics* **13**, 025025 (2011).

Bibliography

- ¹⁵N. B. Manson, X.-F. He, and P. T. H. Fisk, “Raman heterodyne detected electron-nuclear-double-resonance measurements of the nitrogen-vacancy center in diamond”, *Optics Letters* **15**, 1094–1096 (1990).
- ¹⁶X.-F. He, N. B. Manson, and P. T. H. Fisk, “Paramagnetic resonance of photoexcited N-V defects in diamond. II. Hyperfine interaction with the ^{14}N nucleus”, *Physical Review B* **47**, 8816–8822 (1993).
- ¹⁷B. Smeltzer, J. McIntyre, and L. Childress, “Robust control of individual nuclear spins in diamond”, *Physical Review A* **80**, 050302 (2009).
- ¹⁸S. Felton et al., “Hyperfine interaction in the ground state of the negatively charged nitrogen vacancy center in diamond”, *Physical Review B* **79**, 075203 (2009).
- ¹⁹M. Steiner et al., “Universal enhancement of the optical readout fidelity of single electron spins at nitrogen-vacancy centers in diamond”, *Physical Review B* **81**, 035205 (2010).
- ²⁰C. S. Shin et al., “Optically detected nuclear quadrupolar interaction of ^{14}N in nitrogen-vacancy centers in diamond”, *Physical Review B* **89**, 205202 (2014).
- ²¹G. Balasubramanian et al., “Ultralong spin coherence time in isotopically engineered diamond”, *Nature Materials* **8**, 383–387 (2009).
- ²²L. Hanlon et al., *Enhancement of spin-to-charge conversion of diamond NV centers at ambient conditions using surface electrodes*, (Sept. 28, 2022) <http://arxiv.org/abs/2209.14012>, preprint.
- ²³E. Bauch et al., “Ultralong Dephasing Times in Solid-State Spin Ensembles via Quantum Control”, *Physical Review X* **8**, 031025 (2018).
- ²⁴H. Clevenson et al., “Broadband magnetometry and temperature sensing with a light-trapping diamond waveguide”, *Nature Physics* **11**, 393–397 (2015).
- ²⁵J. M. Taylor et al., “High-sensitivity diamond magnetometer with nanoscale resolution”, *Nature Physics* **4**, 810–816 (2008).
- ²⁶F. Reinhard, *Nanoscale Sensing and Quantum Coherence*, (June 11, 2019) <http://arxiv.org/abs/1906.04637>, preprint.
- ²⁷G. Binnig, C. F. Quate, and Ch. Gerber, “Atomic Force Microscope”, *Physical Review Letters* **56**, 930–933 (1986).
- ²⁸F. J. Giessibl, “Advances in atomic force microscopy”, *Reviews of Modern Physics* **75**, 949–983 (2003).
- ²⁹L. Gross, “Recent advances in submolecular resolution with scanning probe microscopy”, *Nature Chemistry* **3**, 273–278 (2011).
- ³⁰R. Reifengerger, *Fundamentals of Atomic Force Microscopy: Part I: Foundations* (WORLD SCIENTIFIC, Nov. 2015).
- ³¹D. Pinto et al., “Readout and control of an endofullerene electronic spin”, *Nature Communications* **11**, 6405 (2020).
- ³²H. Mauser et al., “Stabilization of Atomic Nitrogen Inside C60”, *Angewandte Chemie International Edition in English* **36**, 2835–2838 (1997).
- ³³J. C. Greer, “The atomic nature of endohedrally encapsulated nitrogen N@C60 studied by density functional and Hartree-Fock methods”, *Chemical Physics Letters* **326**, 567–572 (2000).

- ³⁴W. Harneit, “Spin Quantum Computing with Endohedral Fullerenes”, in *Endohedral Fullerenes: Electron Transfer and Spin*, edited by A. A. Popov, Nanostructure Science and Technology (Springer International Publishing, Cham, 2017), pp. 297–324.
- ³⁵W. Harneit, “Fullerene-based electron-spin quantum computer”, *Physical Review A* **65**, 032322 (2002).
- ³⁶C. Meyer et al., “Experimental Steps Towards the Realisation of a Fullerene Quantum Computer”, *physica status solidi (b)* **233**, 462–466 (2002).
- ³⁷K. Huebener et al., “ODMR of NV centers in nano-diamonds covered with N@C60”, *physica status solidi (b)* **245**, 2013–2017 (2008).
- ³⁸R. S. Schonfeld, “Optical readout of single spins for quantum computing and magnetic sensing”,
- ³⁹S. Zhou and K. Porfyraakis, “Preparation and Chemistry of N@C60”, in *Endohedral Fullerenes: Electron Transfer and Spin*, edited by A. A. Popov, Nanostructure Science and Technology (Springer International Publishing, Cham, 2017), pp. 265–295.
- ⁴⁰J. Twamley, “Quantum-cellular-automata quantum computing with endohedral fullerenes”, *Physical Review A* **67**, 052318 (2003).
- ⁴¹K. -. Dinse et al., “EPR investigation of atoms in chemical traps”, *Carbon, Fullerenes '99* **38**, 1635–1640 (2000).
- ⁴²B. Goedde et al., “‘Nitrogen doped’ C60 dimers (N@C60–C60)”, *Chemical Physics Letters* **334**, 12–17 (2001).
- ⁴³S. R. Plant et al., “A two-step approach to the synthesis of N@C60 fullerene dimers for molecular qubits”, *Chemical Science* **4**, 2971–2975 (2013).
- ⁴⁴A. J. Häußler et al., “Optical depth localization of nitrogen-vacancy centers in diamond with nanometer accuracy”, *Optics Express* **22**, 29986–29995 (2014).
- ⁴⁵E. Schaefer-Nolte et al., “A diamond-based scanning probe spin sensor operating at low temperature in ultra-high vacuum”, *Review of Scientific Instruments* **85**, 013701 (2014).
- ⁴⁶J. J. L. Morton et al., “Electron spin relaxation of N@C60 in CS₂”, *The Journal of Chemical Physics* **124**, 014508 (2006).
- ⁴⁷F. Shi et al., “Single-protein spin resonance spectroscopy under ambient conditions”, *Science* **347**, 1135–1138 (2015).
- ⁴⁸H. J. Mamin et al., “Multipulse Double-Quantum Magnetometry with Near-Surface Nitrogen-Vacancy Centers”, *Physical Review Letters* **113**, 10 . 1103 / PhysRevLett . 113 . 030803 (2014).
- ⁴⁹L. Schlipf et al., “A molecular quantum spin network controlled by a single qubit”, *Science Advances* **3**, e1701116 (2017).
- ⁵⁰M. Scheloske et al., “Synthesis and Functionalization of Fullerenes Encapsulating Atomic Phosphorus”, *Israel Journal of Chemistry* **46**, 407–412 (2006).
- ⁵¹L. Franco et al., “Synthesis and magnetic properties of N@C60 derivatives”, *Chemical Physics Letters* **422**, 100–105 (2006).
- ⁵²E. Dietel et al., “Atomic Nitrogen Encapsulated in Fullerenes: Effects of Cage Variations”, *Journal of the American Chemical Society* **121**, 2432–2437 (1999).

Bibliography

- ⁵³B. Naydenov, “Encapsulation of Endohedral Fullerenes for Quantum Computing”, <http://dx.doi.org/10.17169/refubium-16421> (2006).
- ⁵⁴B. K. Ofori-Okai et al., “Spin properties of very shallow nitrogen vacancy defects in diamond”, *Physical Review B* **86**, 081406 (2012).
- ⁵⁵T. Roskopf et al., “Investigation of Surface Magnetic Noise by Shallow Spins in Diamond”, *Physical Review Letters* **112**, 147602 (2014).
- ⁵⁶M. Waiblinger et al., “Corrected Article: Thermal stability of the endohedral fullerenes N @ C 60 , N @ C 70 , and P @ C 60 [Phys. Rev. B **63** , 045421 (2001)]”, *Physical Review B* **64**, 10.1103/PhysRevB.64.159901 (2001).
- ⁵⁷M. Eckardt, R. Wiczorek, and W. Harneit, “Stability of C60 and N@C60 under thermal and optical exposure”, *Carbon* **95**, 601–607 (2015).
- ⁵⁸E. D. Herbschleb et al., “Ultra-long coherence times amongst room-temperature solid-state spins”, *Nature Communications* **10**, 3766 (2019).
- ⁵⁹M. Ozmaian et al., “Diffusion and self-assembly of C60 molecules on monolayer graphyne sheets”, *Scientific Reports* **6**, 10.1038/srep21910 (2016).
- ⁶⁰P. C. Maurer et al., “Room-Temperature Quantum Bit Memory Exceeding One Second”, *Science* **336**, 1283–1286 (2012).
- ⁶¹J. J. L. Morton et al., “Solid-state quantum memory using the 31P nuclear spin”, *Nature* **455**, 1085–1088 (2008).
- ⁶²D. D. Awschalom et al., “Quantum Spintronics: Engineering and Manipulating Atom-Like Spins in Semiconductors”, *Science* **339**, 1174–1179 (2013).
- ⁶³B. Keimer and J. E. Moore, “The physics of quantum materials”, *Nature Physics* **13**, 1045–1055 (2017).
- ⁶⁴N. Hedrich et al., “Nanoscale mechanics of antiferromagnetic domain walls”, *Nature Physics* **17**, 574–577 (2021).
- ⁶⁵A. K. Nayak et al., “Magnetic antiskyrmions above room temperature in tetragonal Heusler materials”, *Nature* **548**, 561–566 (2017).
- ⁶⁶F. P. Chmiel et al., “Observation of magnetic vortex pairs at room temperature in a planar α -Fe2O3/Co heterostructure”, *Nature Materials* **17**, 581–585 (2018).
- ⁶⁷I. Gross et al., “Real-space imaging of non-collinear antiferromagnetic order with a single-spin magnetometer”, *Nature* **549**, 252–256 (2017).
- ⁶⁸*SHOM Flag style sample plate*, <https://www.ferrovac.com/?tool=ProductDescription&product=SHOM>.
- ⁶⁹J. W. Ekin, “6 Properties of Solids at Low Temperatures”, in *Experimental Techniques for Low-Temperature Measurements: Cryostat Design, Material Properties and Superconductor Critical-Current Testing*, edited by J. Ekin (Oxford University Press, Oct. 12, 2006), pp. 226–270.
- ⁷⁰M. L. Williams, “CRC Handbook of Chemistry and Physics, 76th edition”, *Occupational and Environmental Medicine* **53**, 504 (1996).
- ⁷¹*Supplier Data - Polyetheretherketone (PEEK) (Goodfellow)*, AZoM.com, (Mar. 5, 2003) <https://www.azom.com/article.aspx?ArticleID=1882>.

- ⁷²J. M. Binder et al., “Qudi: A modular python suite for experiment control and data processing”, *SoftwareX* **6**, 85–90 (2017).
- ⁷³J. M. Perkel, “Programming: Pick up Python”, *Nature* **518**, 125–126 (2015).
- ⁷⁴*The top programming languages*, The State of the Octoverse, <https://octoverse.github.io/com/2022/top-programming-languages>.
- ⁷⁵*Qcodes_contrib_drivers/pyspcm.py at main · QCoDeS/Qcodes_contrib_drivers*, GitHub, https://github.com/QCoDeS/Qcodes_contrib_drivers.
- ⁷⁶D. Paone et al., “All-optical and microwave-free detection of Meissner screening using nitrogen-vacancy centers in diamond”, *Journal of Applied Physics* **129**, 024306 (2021).
- ⁷⁷J. Kools, “Exchange-biased spin-valves for magnetic storage”, *IEEE Transactions on Magnetics* **32**, 3165–3184 (1996).
- ⁷⁸A. Scholl et al., “Observation of Antiferromagnetic Domains in Epitaxial Thin Films”, *Science* **287**, 1014–1016 (2000).
- ⁷⁹M. J. Grzybowski et al., “Imaging Current-Induced Switching of Antiferromagnetic Domains in CuMnAs”, *Physical Review Letters* **118**, 057701 (2017).
- ⁸⁰S. Heinze et al., “Real-Space Imaging of Two-Dimensional Antiferromagnetism on the Atomic Scale”, *Science* **288**, 1805–1808 (2000).
- ⁸¹A. Krönlein et al., “Magnetic Ground State Stabilized by Three-Site Interactions: Fe/Rh(111)”, *Physical Review Letters* **120**, 207202 (2018).
- ⁸²M. Kleiber et al., “Topology-Induced Spin Frustrations at the Cr(001) Surface Studied by Spin-Polarized Scanning Tunneling Spectroscopy”, *Physical Review Letters* **85**, 4606–4609 (2000).
- ⁸³W. Legrand et al., “Room-temperature stabilization of antiferromagnetic skyrmions in synthetic antiferromagnets”, *Nature Materials* **19**, 34–42 (2020).
- ⁸⁴P. M. Sass et al., “Magnetic Imaging of Domain Walls in the Antiferromagnetic Topological Insulator MnBi₂Te₄”, *Nano Letters* **20**, 2609–2614 (2020).
- ⁸⁵P. Appel et al., “Nanomagnetism of Magnetoelectric Granular Thin-Film Antiferromagnets”, *Nano Letters* **19**, 1682–1687 (2019).
- ⁸⁶A. Haykal et al., “Antiferromagnetic textures in BiFeO₃ controlled by strain and electric field”, *Nature Communications* **11**, 1704 (2020).
- ⁸⁷Q.-C. Sun et al., “Magnetic domains and domain wall pinning in atomically thin CrBr₃ revealed by nanoscale imaging”, *Nature Communications* **12**, 1989 (2021).
- ⁸⁸A. Finco et al., “Imaging non-collinear antiferromagnetic textures via single spin relaxometry”, *Nature Communications* **12**, 767 (2021).
- ⁸⁹O. Hellwig, A. Berger, and E. E. Fullerton, “Domain Walls in Antiferromagnetically Coupled Multilayer Films”, *Physical Review Letters* **91**, 197203 (2003).
- ⁹⁰O. Hellwig et al., “A new phase diagram for layered antiferromagnetic films”, *Nature Materials* **2**, 112–116 (2003).
- ⁹¹P. F. Carcia, A. D. Meinhaldt, and A. Suna, “Perpendicular magnetic anisotropy in Pd/Co thin film layered structures”, *Applied Physics Letters* **47**, 178–180 (1985).
- ⁹²M. T. Johnson et al., “Magnetic anisotropy in metallic multilayers”, *Reports on Progress in Physics* **59**, 1409 (1996).

Bibliography

- ⁹³C. Kittel, “Theory of the Structure of Ferromagnetic Domains in Films and Small Particles”, *Physical Review* **70**, 965–971 (1946).
- ⁹⁴N. Hedrich et al., “Parabolic Diamond Scanning Probes for Single-Spin Magnetic Field Imaging”, *Physical Review Applied* **14**, 064007 (2020).
- ⁹⁵J.-P. Tetienne et al., “Magnetic-field-dependent photodynamics of single NV defects in diamond: an application to qualitative all-optical magnetic imaging”, *New Journal of Physics* **14**, 103033 (2012).
- ⁹⁶I. Gross et al., “Skyrmion morphology in ultrathin magnetic films”, *Physical Review Materials* **2**, 024406 (2018).
- ⁹⁷W. Akhtar et al., “Current-Induced Nucleation and Dynamics of Skyrmions in a Co-based Heusler Alloy”, *Physical Review Applied* **11**, 034066 (2019).
- ⁹⁸J. N. Neethirajan et al., “Controlled Surface Modification to Revive Shallow NV– Centers”, *Nano Letters*, [10.1021/acs.nanolett.2c04733](https://doi.org/10.1021/acs.nanolett.2c04733) (2023).
- ⁹⁹F. Brandenburg et al., “Improving the electron spin properties of nitrogen-vacancy centres in nanodiamonds by near-field etching”, *Scientific Reports* **8**, 15847 (2018).
- ¹⁰⁰C. Schreyvogel et al., “Active and fast charge-state switching of single NV centres in diamond by in-plane Al-Schottky junctions”, *Beilstein Journal of Nanotechnology* **7**, 1727–1735 (2016).
- ¹⁰¹N. Aslam et al., “Photo-induced ionization dynamics of the nitrogen vacancy defect in diamond investigated by single-shot charge state detection”, *New Journal of Physics* **15**, 013064 (2013).
- ¹⁰²Z. Yuan et al., “Charge state dynamics and optically detected electron spin resonance contrast of shallow nitrogen-vacancy centers in diamond”, *Physical Review Research* **2**, 033263 (2020).
- ¹⁰³D. Bluvstein, Z. Zhang, and A. C. B. Jayich, “Identifying and Mitigating Charge Instabilities in Shallow Diamond Nitrogen-Vacancy Centers”, *Physical Review Letters* **122**, 076101 (2019).
- ¹⁰⁴M. Berthel et al., “Photophysics of single nitrogen-vacancy centers in diamond nanocrystals”, *Physical Review B* **91**, 035308 (2015).
- ¹⁰⁵L. J. Rogers et al., “Electronic structure of the negatively charged silicon-vacancy center in diamond”, *Physical Review B* **89**, 235101 (2014).
- ¹⁰⁶C. Hepp et al., “Electronic Structure of the Silicon Vacancy Color Center in Diamond”, *Physical Review Letters* **112**, 036405 (2014).
- ¹⁰⁷G. D. Cheng et al., “Theory of sulfur-vacancy defect in diamond: a comparable NV-1 iso-electronic center”, *Optik* **136**, 151–156 (2017).
- ¹⁰⁸T. Lühmann et al., “Coulomb-driven single defect engineering for scalable qubits and spin sensors in diamond”, *Nature Communications* **10**, 4956 (2019).
- ¹⁰⁹T. Iwasaki et al., “Germanium-Vacancy Single Color Centers in Diamond”, *Scientific Reports* **5**, 12882 (2015).
- ¹¹⁰Y. N. Palyanov et al., “Germanium: a new catalyst for diamond synthesis and a new optically active impurity in diamond”, *Scientific Reports* **5**, 14789 (2015).
- ¹¹¹A. Watanabe et al., “Shallow NV centers augmented by exploiting n-type diamond”, *Carbon* **178**, 294–300 (2021).

- ¹¹²V. Dyakonov et al., “Atomic-Scale Defects in Silicon Carbide for Quantum Sensing Applications”, *Materials Science Forum* **821–823**, 355–358 (2015).
- ¹¹³F. J. Heremans, C. Yale, and D. Awschalom, “Control of Spin Defects in Wide-Bandgap Semiconductors for Quantum Technologies”, *Proceedings of the IEEE* **104**, 1–15 (2016).
- ¹¹⁴S. Castelletto and A. Boretti, “Silicon carbide color centers for quantum applications”, *Journal of Physics: Photonics* **2**, 022001 (2020).
- ¹¹⁵H. Jani et al., “Antiferromagnetic half-skyrmions and bimerons at room temperature”, *Nature* **590**, 74–79 (2021).
- ¹¹⁶S. Woo et al., “Observation of room-temperature magnetic skyrmions and their current-driven dynamics in ultrathin metallic ferromagnets”, *Nature Materials* **15**, 501–506 (2016).
- ¹¹⁷A. Soumyanarayanan et al., “Tunable room-temperature magnetic skyrmions in Ir/Fe/Co/Pt multilayers”, *Nature Materials* **16**, 898–904 (2017).
- ¹¹⁸M. V. Rodnina, “Translation in Prokaryotes”, *Cold Spring Harbor Perspectives in Biology* **10**, a032664 (2018).
- ¹¹⁹B. D. Beck, “Polymerization of the bacterial elongation factor for protein synthesis, EF-Tu”, *European Journal of Biochemistry* **97**, 495–502 (1979).
- ¹²⁰H. J. Defeu Soufo et al., “Bacterial translation elongation factor EF-Tu interacts and colocalizes with actin-like MreB protein”, *Proceedings of the National Academy of Sciences of the United States of America* **107**, 3163–3168 (2010).
- ¹²¹D. Pinto, *Dineshpinto/qudi-hira-analysis: v1.0.0*, version v1.0.0, Zenodo, Feb. 4, 2023.
- ¹²²Y. Sonnefraud et al., “Diamond nanocrystals hosting single nitrogen-vacancy color centers sorted by photon-correlation near-field microscopy”, *Optics Letters* **33**, 611–613 (2008).
- ¹²³A. Beveratos et al., “Bunching and Antibunching from Single NV Color Centers in Diamond”, in *Quantum Communication, Computing, and Measurement 3*, edited by P. Tombesi and O. Hirota (Springer US, Boston, MA, 2002), pp. 261–267.
- ¹²⁴N. V. Vitanov et al., “Power broadening revisited: theory and experiment”, *Optics Communications* **199**, 117–126 (2001).
- ¹²⁵A. Dréau et al., “Avoiding power broadening in optically detected magnetic resonance of single NV defects for enhanced dc magnetic field sensitivity”, *Physical Review B* **84**, 195204 (2011).
- ¹²⁶F. Kong et al., “Kilohertz electron paramagnetic resonance spectroscopy of single nitrogen centers at zero magnetic field”, *Science Advances* **6**, eaaz8244 (2020).
- ¹²⁷G. de Lange et al., “Controlling the quantum dynamics of a mesoscopic spin bath in diamond”, *Scientific Reports* **2**, 382 (2012).
- ¹²⁸J. Xing et al., “Electron Spin Decoherence of Nitrogen-Vacancy Center Coupled to Multiple Spin Baths*”, *Chinese Physics Letters* **33**, 107601 (2016).

Short Curriculum Vitæ

Dinesh Pinto

annual.fallout_0z@icloud.com

Education

EPFL, Lausanne, Switzerland
2019 – 2023 *Doctor of Philosophy – PhD, Physics*

University of Stuttgart, Stuttgart, Germany
2016 – 2018 *Master of Science – MSc, Physics*

St. Stephen's College, University of Delhi, India
2013 – 2016 *Bachelor of Science – BSc (Honors), Physics*

Research Experience

3. Physikalisches Institut, University of Stuttgart
2017 – 2018 *Research Assistant*

St. Stephen's Center for Theoretical Physics, University of Delhi
2014 – 2016 *Research Assistant*

Publications & Peer review

D. Pinto, R. Román, A. Singha, J. Wrachtrup and K. Kern. A nitrogen vacancy scanning probe microscope at ultra-high vacuum and high magnetic fields. (In preparation)

J. Neethirajan, T. Hache, D. Paone, D. Pinto, A. Denisenko, R. Stöhr, P. Udvarhelyi, A. Pershin, A. Gali, J. Wrachtrup, K. Kern, and A. Singha. Controlled surface-modification to revive shallow NV⁻ centers. *Nano Letters* 2023, 23, 7, 2563-2569 (2023)

D. Pinto. [dineshpinto/qudi-hira-analysis: v1.0.0. Zenodo 7604670](https://zenodo.org/record/7604670) (2023).

D. Paone, D. Pinto, G. Kim, L. Feng, M.J. Kim, R. Stöhr, A. Singha, S. Kaiser, G. Logvenov, B. Keimer, J. Wrachtrup, and K. Kern. All-optical and microwave-free detection of Meissner screening using nitrogen-vacancy centers in diamond. *Journal of Applied Physics* 129, 024306 (2021)

D. Pinto, D. Paone, B. Kern, T. Dierker, R. Wieczorek, A. Singha, D. Dasari, A. Finkler, W. Harneit, J. Wrachtrup and K. Kern. Readout and control of an endofullerene electronic spin. *Nature Communications* 11, 6405 (2020)

Reviewed publications in *APL Materials* (1), *Applied Physics Letters* (4), *Journal of Applied Physics* (2) and *Review of Scientific Instruments* (1)